11-7-2022

Exploring the Biomedical Applications of Polyurethane-based Foams, Films, and Hydrogels

Anand Utpal Vakil
Syracuse University

Recommended Citation

Abstract

Shape memory polymers (SMPs) are a class of smart materials that can be temporarily stored in a deformed shape and can actively recover their original shape upon exposure to an external stimulus, such as heat, magnetic field, moisture, pH, light, or electric field. The ability of SMPs to change shape when required can be used for a wide range of applications, especially in the case of minimally invasive biomedical applications. In this work, polyurethane-based SMPs were explored for their use in tissue engineering, drug delivery, and wound healing applications.

In the second chapter, low density porous foams with tunable degradability were developed for their use in tissue engineering applications. *In vitro* degradation profiles were compared to *in vivo* degradation profiles to establish a correlation between the two. This work is useful to accurately develop an understanding of the degradability of materials before testing them on animals. It is vital to match the biomaterial's degradation rate to the regeneration rate of surrounding tissues and thereby avoid any hindrance caused by the biomaterials to new tissue growth.

The third chapter explores the use of magnetically activated SMP films to achieve on-demand drug delivery. The films developed here can be remotely triggered to undergo a shape change by exposure to an alternating magnetic field and thereby provide drug release as required. The ability to control the rate of shape change based on the polymer chemistry and the magnetic particle content enables tunability of drug release rate. These materials can either be used to release a single drug at varying time points or simultaneously administer two drugs at different release rates.

In the fourth chapter, antimicrobial poly(ethylene glycol)-based polyurethane hydrogels were developed. Readily available plant-based phenolic acids were physically incorporated into the hydrogels to impart the antimicrobial properties. When applied to a topical wound site, these hydrogels could easily recover their original shape, seal the wound, and release the phenolic acids. These materials proved to inhibit bacterial growth for 20 days, which could be used to prevent an acute wound from developing into a chronic wound.

Overall, this work demonstrates the ability to alter SMP scaffold properties as required to develop a range of biomaterials for varied healing applications.

Exploring the Biomedical Applications of Polyurethane-based

Foams, Films, and Hydrogels

by

Anand Utpal Vakil

B.Tech., Manipal Institute of Technology, 2016

M.S., Syracuse University, 2018

Dissertation

Submitted in partial fulfillment of the requirements for the degree of

Doctor of Philosophy in Chemical Engineering

Syracuse University

December 2022

To my parents, and my brother ….

Declaration

I hereby declare that this dissertation's contents are original and have not been submitted in whole or in part for consideration for any other degree or qualification in this, or any other academic institution. This dissertation is my work, except where specific reference is made to the work of others.

<div align="right">

Anand Utpal Vakil

December 2022

</div>

Acknowledgments

I would first like to thank my guide and mentor Dr. Mary Beth Browning Monroe, who has been an amazing advisor. Your willingness to give me the freedom to pursue the projects that I wanted and your ability to guide me and keep me moving in the right direction whenever I pondered a problem for too long has made this journey enjoyable. Your guidance has shaped my thought process and enabled me to become a better researcher.

Next, I would like to thank my fantastic lab mates. Especially Natalie Petryk who I did mentor for a couple of years and ended up being a great support to my research. With her amazing grasping ability, Natalie made my duty as a mentor, much easier than it was supposed to be. I would also like to thank my other lab mates - Henry Beaman, Maryam Ramezani, and Changling Du, who have helped me through multiple of my projects. The other mentees that have helped me through my projects are Nakira Christmas, Ellen Shepherd, Darnelle Stintfort, and Bryanna Howes. Overall, the great lab mates made the lab a fun place to work over the years.

I would also like to acknowledge my committee members Dr. Pranav Soman, Dr. Ivan Gitsov Ivanov, Dr. Ian Hosein, Dr. Julie Hasenwinkel, Dr. Era Jain, and Dr. Rachel Steinhardt. Their feedback during my initial candidacy exam did give some concrete feedback that helped shape my dissertation.

My friends – Raj De, Deepjyoti Singh, Sarthak Gupta and Sumon Sahu have been amazing support systems. I could honestly rely on them to destress.

Lastly, I would like to thank my family members – my parents and my brother. I could not have

completed this journey without the strong foundation that you have provided me with.

TABLE OF CONTENTS

LIST OF FIGURES

LIST OF TABLES

Chapter I

Introduction

1. Biomaterials

Any material that is designed to interact with biological systems (tissues and/or biological fluids) and replace a part or a function of the body in a safe, reliable, and physiological manner can be termed a biomaterial[1]. Polymer blends and nanocomposites have been widely explored for various biomedical applications, such as biodegradable scaffolds for wound healing and tissue engineering, biosensors, and implants for controlled drug release. These biomaterials consist of natural, synthetic, and semi-synthetic polymers or their blends. Each of these individual groups of materials has its specific advantages and disadvantages, and the properties of biomaterials largely depend on the material used for their preparation.[2], [3] An overview of some of the biomaterials used in wound healing and tissue engineering applications is provided in the following sections.

1.1 Natural Biomaterials

There are abundant options of natural polymers derived from plants and animals. Cellulose, derived from the plant cell wall, has been converted into fibers and is widely used for various biomedical applications due to its high crystallinity and strength[4]. Similarly, chitosan, obtained from shells of crustaceans has been used for multiple applications due to its degradability (hydrolysis via lysozyme)[5], biocompatibility, antimicrobial activity, cell attachment, and hemostatic properties[6]. Other examples of naturally occurring polymers that are used for biomedical applications include alginate, carrageenan, pectin, collagen, and gelatin.

1.2 Semi-synthetic biomaterials

Semi-synthetic polymers may be termed as materials from a natural source that have undergone chemical modification to combine the benefits of natural and synthetic components. One such example of semi-synthetic polymers include a combination of polyethylene oxide and silicon-

substituted hydroxyapatite for hard tissue engineering applications such as orthopedic and spine surgery[7]. Semi-synthetic polymers offer added capabilities to tune physicomechanical properties by altering the monomer units, molecular weight, and branching. This process enables an ability to combine the benefits of natural and synthetic polymers. However, the extent to which these mechanical properties can be tuned is limited by the molecular structure of natural polymers. Additionally, natural polymers obtained from animal sources could potentially induce allergic or immunologic reactions when applied to the human body[8]. For example, crustacean-based chitosan has been successfully used as a biomaterial, and allergic reactions can be prevented with well purified chitin-derived products; however, improper purification can make chitosan unusable for patients that suffer from shellfish allergies[9]. Chitosan also has limited solubility in water unless it has an acidic pH, and its insolubility in organic solvents limits modifications and crosslinking that can be performed. In another example, studies on injectable collagen-based devices[10]–[12] produced by pepsin extraction from calf skin for soft tissue augmentation[13], [14] have consistently shown incidence of preexisting hypersensitivity to bovine collagen (i.e., allergies) in 2- 4% of patients. An additional 1% of subjects develop postoperative bovine allergies, which limits bovine collagen clinical use[10]–[12].

1.3 Synthetic biomaterials

Synthetic polymers offer a wide range of tunability. They are used for soft tissue repair and regenerative medicine due to their ability to closely mimic biological tissues and their relatively low cost compared to biomaterials obtained from natural sources. The thermo-mechanical properties, biocompatibility, degradability, and wound healing capabilities of synthetic biomaterials can be tuned to a great extent by altering the monomers, additives, and processing

3

conditions. Both degradable and non-degradable synthetic biomaterials have been used for regenerative medicine applications.

1.3.1 Non-degradable or biostable synthetic biomaterials.

Biostable biopolymers are used to replace tissues that are damaged to an extent that they are incapable of normal function. Some examples of biostable polymers include :

- **Polymethyl methacrylate (PMMA).** PMMA has a relatively high coefficient of thermal expansion (193.6×10^{-6} °C^{-1}) [15], high compressive strength (between 85 and 110 MPa), and excellent optical properties, which enable its use in applications such as hard contact lenses[16] and bone cement[17].

- **Poly(ethylene terephthalate) (PET).** The high glass transition temperature (70°C), yield strength (40 MPa), and biocompatibility of PET, along with its impermeability to most gases and liquids,[18] enable its use to repair large blood vessels and other soft tissues isurgeries such as axillofemoral bypass[19], rhinoplasty[20], and ligament reconstruction[21].

- **Silicones.** Overall, silicones have an extremely low surface tension that enables them to repel water easily. The ability to tune the material properties based on altering side chains and extent of crosslinking, along with being non-degradable and nontoxic enables silicones to be used for a wide number of applications that include intraocular lenses, bandages, scar treatment sheets, and breast implants [22].

1.3.2 Degradable synthetic and semisynthetic biomaterials.

4

Biodegradability is a major criteria for successful tissue regeneration [23]. Biomaterial scaffolds provide a suitable environment for the cells to grow by enabling the exchange of required nutrients, oxygen, metabolic products, and suitable growth factors to enhance cell growth and differentiation. Ideally, these scaffolds degrade away during healing to leave only healthy tissue behind and no remains of the synthetic material. Synthetic polymers are degraded via chain scission that can occur via hydrolytic or oxidative degradation. Semi-synthetic biopolymers can degrade via enzymatic degradation as well. Hydrolytic degradation typically occurs via chain scission of ester linkages by water molecules [24]. Oxidative degradation often occurs via tertiary amine and ether breakage by reactive oxygen species released by macrophages [25]. Enzymatic degradation occurs via the breakage of a glycosidic linkage or a peptide bond through enzyme-catalyzed hydrolysis known as enzymolysis or enzymatic hydrolysis [26]. Some examples of biodegradable biomaterials include:

- **Poly(lactic) acid (PLA).** A high elastic modulus (~3 GPa) and high tensile strength (~50-70 MPa) along with slow degradability (~2 years) make PLA suitable for use in anchoring bone implants [27], [28].

- **Poly(glycolic) acid (PGA).** A faster hydrolytic degradation rate (~10 weeks) [29] compared to PLA along with higher tensile modulus (~7 GPa) and high crystallinity (~55%) [30] makes PGA suitable for use as degradable sutures.

- **Polycaprolactone (PCL).** Due to its semi-crystalline nature, PCL has a relatively low degradability rate (2 to 4 years) in aqueous environments depending on its molecular weight [31]. PCL can be easily copolymerized with other polymers, such as polyethylene oxide, to develop polymeric blends with both hydrophobic and hydrophilic microdomains [32].

5

2. Polyurethanes

Another class of biomaterials that is one of the most versatile families of polymers is polyurethanes [33]–[36]. These are synthesized by a step-growth or condensation reaction between isocyanates and hydroxyls along with supplementary chemicals and catalysts. Polyurethanes were developed by Bayer in 1937 [37] and today these materials are widely used in the biomedical industry. In 2019 global polyurethane production was estimated to be 25 million metric tons, accounting for 6% of all polymers produced that year, and is expected to reach 29.2 million metric tons by 2029 [38].

Step growth and polycondensation reactions usually result in condensation byproducts such as water or CO_2, however, there are no byproducts produced during the formation of urethane linkages between isocyanates and hydroxyls. Linear segmented thermoplastic networks can be obtained by reacting diisocyanates and diols. Highly crosslinked thermoset networks can be obtained by reaction between diisocyanates and polyols containing more than two functional groups, such as triols or tetraols.

To form a stable polyurethane network, it is vital to balance the total electrophile equivalents provided by isocyanates with an equal or slightly higher number of nucleophile equivalents provided by hydroxyls, carboxylic acids, or amines (reactions 1 through 6) to avoid isocyanate side reactions (reactions 7 and 8) that could occur as shown in **Figure 1** [39], [40]. At temperatures below 60°C, allophanate (reaction 3) and biuret (reaction 7) formation are very slow, and can thus be avoided by ensuring that net hydroxyls are lower than the total isocyanates [41]. The products formed via side reactions can interfere with the required urethane formation and potentially lead to altered thermomechanical properties. Excess nucleophilic equivalents can be washed away during a cleaning procedure to obtain a pure product.
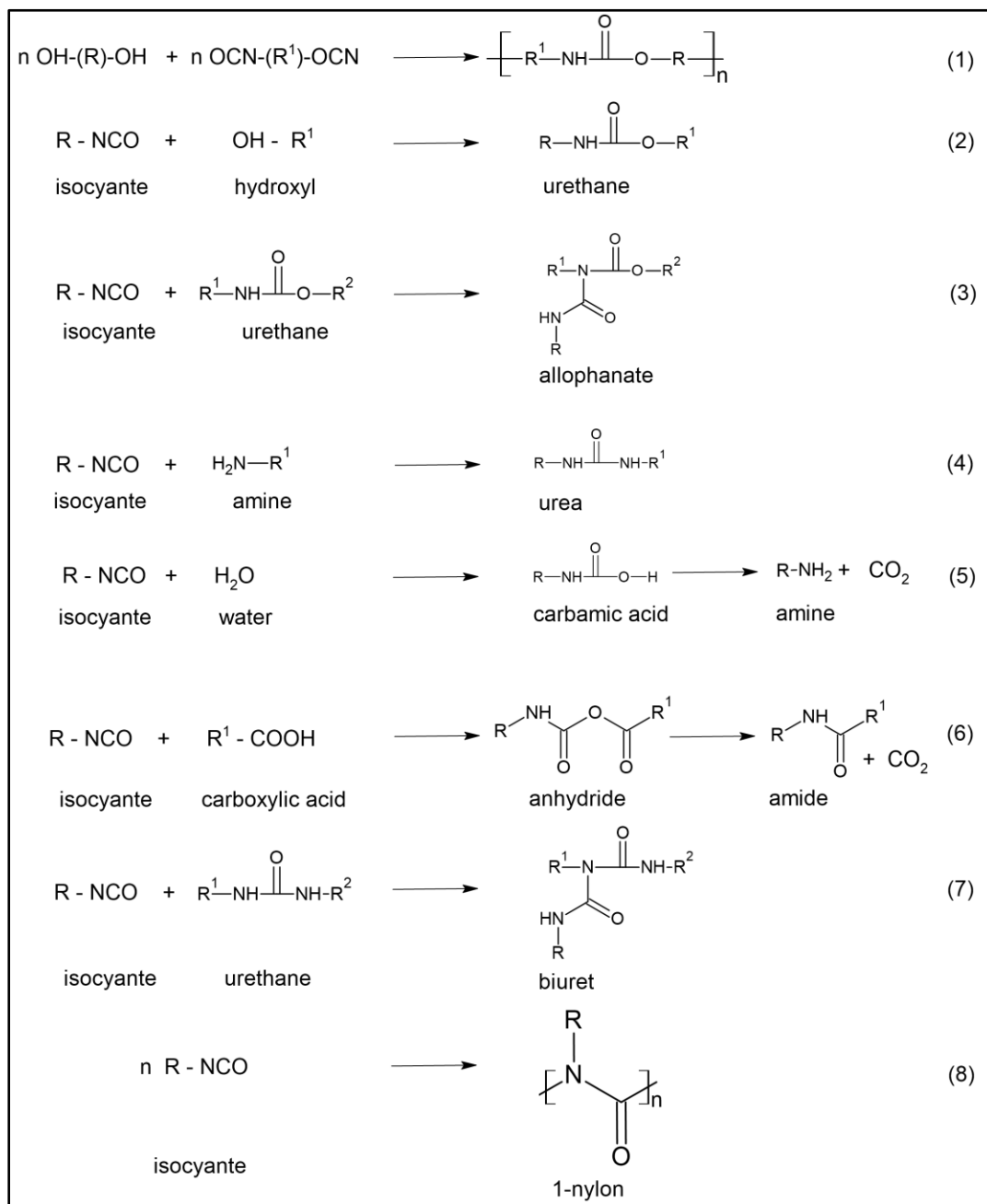
Figure 1.1 Basic reactions during urethane synthesis[42].

Final applications of polyurethanes can be employed in the form of foams, hydrogels, and/or films.

2.1 Polyurethane Foams

7

Commerical polyurethane foams are used in several applications that include home insulation, bedding, furniture, automotive interiors, carpet underlying, and packaging [43]. Foams can either be flexible or rigid depending on the application. Flexible slabstock foams are the most common polyurethane product in the commercial industry. Flexible foams amount to 50% of global polyurethane production [44].

2.2 Foaming process

Polyurethane foams are synthesized via a two-part process. The first part involves the formation of an isocyanate pre-mix. Here all the required isocyanates are allowed to react with a portion of the total required hydroxyls. The mixture is thoroughly mixed and allowed to react at a predetermined temperature for a predetermined time. During this step, a fraction of the isocyanates is allowed to react with hydroxyls to form an isocyanate-terminated pre-polymer with a slightly increased viscosity. This step is carried out entirely in a controlled dry environment to avoid the reaction between isocyanates and atmospheric moisture. Once the pre-polymer reaches a required viscosity, surfactants are added to this mixture. During the second step, a hydroxyl mixture is prepared that contains the balance of hydroxyls along with the required amount of catalyst and blowing agents (e.g., water), which are then mixed with the pre-polymer to form a stable foam. The reaction between water and isocyanates results in the formation of urea and CO_2 that evaporates and is released as a byproduct; this initiates the blowing process. Thus water is considered a chemical blowing agent during the formation of polyurethane foams.

During the synthesis of flexible polyurethane foams, it is vital to balance the rate of gelling and foaming reactions. These rates are dependent on the amount and type of additives added during the foaming process. If gelling (reaction 2, catalyzed by tertiary amine-based catalysts) occurs faster than blowing (reaction 6, catalyzed by tin-based catalysts), the polymer would cure quickly

and will not be able to rise to provide the required blowing effect. If the blowing occurs faster than gelling, the resultant foam would rise rapidly and then collapse due to inadequate curing.

The novel physical properties of hyperbranched polyurethane macromolecules render them ideal candidates for use as shape memory materials. Flexible shape memory polymer foams are used for biomedical applications due to their tunable mechanical and thermal properties, biocompatibility, shape filling capabilities, and tuneable degradability [45]–[47].

3 Shape memory polymers

Shape memory polymers are a group of 'smart' materials that provide an avenue to solve scientific challenges through their ability to undergo geometric transformations upon exposure to an external stimulus such as temperature, light, moisture, pH, enzyme, magnetic field, or electrical impulse [48]–[54]. These 'smart' materials are initially fabricated in a primary shape that can be deformed into a temporary secondary shape using an appropriate stimulus, known as programming. The primary shape can be regained back upon application of a second external stimulus, known as recovery, as shown in **Figure 2**. The stimulus used may or may not be the same during the programming and recovery stages. For example, thermally-induced shape memory polymers can be temporarily deformed into a secondary shape using heat as an external stimulus, but can regain their original shape via indirect actuation using magnetic field, [55] infrared light [56], or electrical current [57] as a stimulus during the recovery stage.
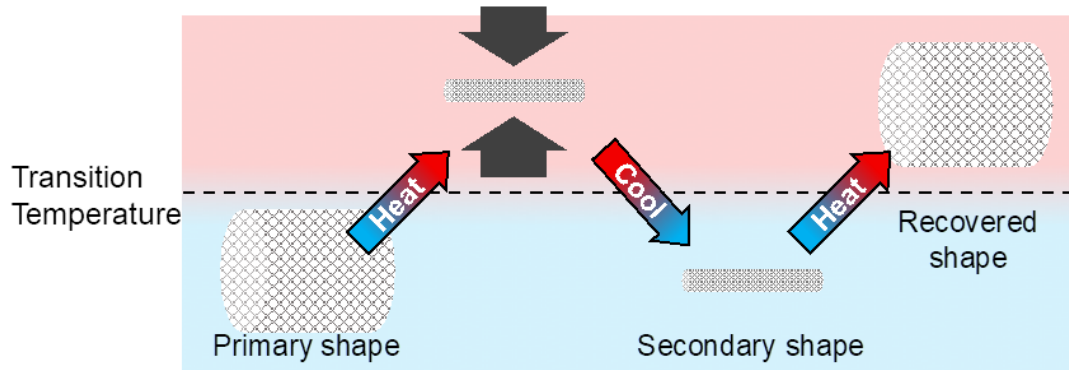
Figure 1.2 Schematic representation of shape memory behavior.

The shape memory effect of a polymer can be initiated by utilizing two major components, net points and switching segments. The permanent shape of a shape memory polymer is determined by the net points of the polymer network. Net points are chain segments that can either be chemical crosslinks, such as covalent bonds, or physical intermolecular interactions, such as hydrogen bonds. Amorphous thermoset networks utilize hydrogen bonds present between crosslinks as switching segments, which break and re-form during shape fixing and shape recovery. These materials transition from a glassy to rubbery phase upon heating above their glass transition temperature (T_g). The hydrogen bonds between chains break above the T_g, either enabling deformation into a tempory shape that is stabilized upon cooling or triggering shape recovery from the temporary to permanent shape [58], [59]. Semi-crystalline polymers contain long-chain flexible macromers that undergo transition based on T_g and serve as soft segments. Strongly hydrogen-bonded chemical crosslinks formed by chain extenders, serve as rigid crystalline hard segments that have a T_g and/or melting temperature well above that of the soft segments [60].

Shape memory polyurethane foams have abundant biomedical uses, especially for wound healing and tissue engineering applications. The key requirements for effective wound healing involve (a) maintaining a moist wound while absorbing exudate, (b) pain reduction, (c) low adherence to the

underlying wound, (d) potential for active intervention in the wound healing process, and (e) maintaining a sterile environment and easy removal from wounds without causing further trauma[61]. These properties are achievable through foams as well as another class of materials - hydrogels.

4. Hydrogels

Hydrogels are defined as three-dimensional crosslinked polymer networks that can absorb large amounts of water and swell up to 10-1000 times their original weight[62] and can thereby maintain a high moisture level of the wound bed. Hydrogels are often made up of water-soluble monomers, yet the highly crosslinked networks prevent dissolution in water. Hydrogels are formed by chemical reactions between monomers or by interactions such as hydrogen bonds or Van der Waals interactions [22]. Hydrogels may be porous or non-porous depending on their applications. If hydrogel networks are formed by molecular entanglements or are held together by secondary forces, such as ionic, hydrogen bonding, or hydrophobic forces, that play a major role in forming the network, they may be considered reversible or physical gels [63]. When covalent bonds are formed by crosslinking the monomers in a dry state or a solution, they may be termed permanent or chemical gels [64].

Due to their extensive water retention capacity and ability to mimic native tissue, hydrogels were initially synthesized commercially for their use in the human body. Hydrogels with superior stability in the swollen state are used to develop contact lenses that require high solid content. Applications that require superior swelling capacity, such as diapers, utilize low-solid content hydrogels. Crosslinkers and monomers used to synthesize the hydrogel networks influence the solid/liquid content of polymer networks, which can be determined during or post-synthesis [65]. Hydrogels can either be natural, semi-synthetic, or synthetic.

11

4.1 Natural hydrogels.

Natural hydrogels are primarily derived from two major sources – polysaccharides and polypeptides. Cellulose is a common polysaccharide that is used to synthesize hydrogels. Cellulose requires additional crosslinking to synthesize a hydrogel network, unlike other water-soluble polysaccharides [66]. Gelatin is a common source of polypeptides. Gelatin is obtained by partial hydrolysis of collagen that is extracted from the skin, bones, and connective tissues of animals and is easily available, degradable, and biocompatible [67].

4.2 Semisynthetic or hybrid hydrogels.

Modifying natural sources of polysaccharides and polypeptides with synthetic monomers enables utilization of the benefits of the high functionality of natural hydrogels along with tunable mechanical properties obtained from synthetic hydrogels. For example, a combination of gelatin and poly(ethylene glycol) (PEG) has been utilized to generate a semi-synthetic nerve scaffold that enables control over the degradation rate, protein composition, and structural features of the polymer matrix to develop a precise platform for the regeneration of peripheral nerves [68].

4.2 Synthetic hydrogels

Synthetic hydrogels are obtained from multiple source, such as N-isopropyl acrylamide (NIPAAm) [69], poly(propylene glycol) PPG, PEG [70], and poly(vinyl alcohol) (PVA) [71]. Due to their easily tunable properties, including porosity, swelling, stability, biocompatibility, biodegradability, and mechanical strength, along with their ability to provide a cell-friendly environment that provides similarity to the extracellular matrix, synthetic hydrogels have abundant use in wound healing applications. Moreover, synthetic hydrogels offer additional advantages over natural hydrogels such as easy shape control, low production cost, and stable mechanical

12

properties. These properties allow the synthesis of stable formulations. Combining the properties of synthetic hydrogels along with polyurethane chemistry allows the formation of stable PEG-based polyurethane hydrogel foams that can be used for dermal wound healing applications.

5. Polyurethane Biomaterials

Polyurethanes have the versatility to be synthesized via an underlying reaction between isocyanates and hydroxyls that can be obtained from a large variety of monomers. This enables the formation of different materials such as foams, films, and hydrogels by tuning the synthesis processes as discussed. The advantage of abundant tunability of polyurethanes is utilized to synthesize easy-to-manufacture scaffolds and biomaterials for tissue engineering, wound healing, and drug delivery applications that are discussed in detail in the subsequent chapters.

6. Scope of this Dissertation

The aim of this work is to explore the potential biomedical applications of Polyurethane-based functional polymers. This dissertation will focus on design rationale, formulation, processing, and application focused characterization of these novel biomaterials as mentioned.

Chapter II includes the evaluation of gas-blown polyurethane foams used for tissue engineering. Here, degradability of shape memory foams has been analyzed. A comparison has been shown between the degradation rates *in vitro* and *in vivo*. This study points out the challenges involved with developing *in vitro* degradation profiles of materials and suggests a change in characterization techniques to better predict *in vivo* degradation profiles of samples.

Chapter III introduces a proof of concept to achieve magnetically actuated on-demand drug delivery. Here, the use of a polyurethane polymer composite is demonstrated that is not dependent on the type of drug used. The formulation developed here can be used to simultaneously administer

two different drugs using a single implant. It can also be used to administer the same drug at different release rates.

Chapter IV involves the use of peg-based polyurethane hydrogels to mitigate bacterial infection. This chapter demonstrates post fabrication modifications that can be performed on hydrogels to impart antimicrobial properties. Hydrogels used here, demonstrated antimicrobial efficacy for a period of 20 days. The use of easily available plant-derived phenolic acids is utilized here to mitigate antibiotic overuse.

References

[1]   J. Park and R. S. Lakes, *Biomaterials: an introduction*, Third. Springer Science & Business Media, 2007.

[2]   F. J. O'Brien, "Biomaterials and scaffolds for tissue engineering," *Mater. Today*, vol. 14, no. 3, pp. 88–95, Mar. 2011.

[3]   M. J. Los, A. Hudecki, and E. Wiechec, *Stem Cells and Biomaterials for Regenerative Medicine*. Elsevier, 2019.

[4]   R. J. Hickey and A. E. Pelling, "Cellulose biomaterials for tissue engineering," *Front. Bioeng. Biotechnol.*, vol. 7, no. MAR, p. 45, 2019.

[5]   M. R. J. SALTON, "Cell Wall of Micrococcus Lysodeikticus as the Substrate of Lysozyme," *Nature*, vol. 170, no. 4331, pp. 746–747, Nov. 1952.

[6]   A.-H. Stricker-Krongrad *et al.*, "Efficacy of Chitosan-Based Dressing for Control of Bleeding in Excisional Wounds," *Eplasty*, vol. 18, p. e14, 2018.

[7]   N. Berri, J. Fares, and Y. Fares, "Polyethylene Oxide and Silicon-Substituted Hydroxyapatite Composite: A Biomaterial for Hard Tissue Engineering in Orthopedic and Spine Surgery," *Adv. Biomed. Res.*, vol. 7, no. 1, p. 117, 2018.

[8]   A. K. Lynn, I. V. Yannas, and W. Bonfield, "Antigenicity and immunogenicity of collagen," *J. Biomed. Mater. Res.*, vol. 71B, no. 2, pp. 343–354, Nov. 2004.

[9]   O. T. Burton and P. Zaccone, "The potential role of chitin in allergic reactions," *Trends Immunol.*, vol. 28, no. 10, pp. 419–422, Oct. 2007.

[10]   L. Cooperman and D. Michaeli, "The immunogenicity of injectable collagen. I. A 1-year

prospective study," *J. Am. Acad. Dermatol.*, vol. 10, no. 4, pp. 638–646, 1984.

[11] L. Cooperman and D. Michaeli, "The immunogenicity of injectable collagen. II. A

retrospective review of seventy-two tested and treated patients," *J. Am. Acad. Dermatol.*,

vol. 10, no. 4, pp. 647–651, 1984.

[12] G. Charriere, M. Bejot, L. Schnitzler, G. Ville, and D. J. Hartmann, "Reactions to a bovine

collagen implant. Clinical and immunologic study in 705 patients," *J. Am. Acad.

Dermatol.*, vol. 21, no. 6, pp. 1203–1208, 1989.

[13] G. Lemperle, N. Hazan-Gaúthier, and M. Lemperle, "PMMA microspheres (Artecoll) for

skin and soft-tissue augmentation. Part II: Clinical investigations," *Plast. Reconstr. Surg.*,

vol. 96, no. 3, pp. 627–634, 1995.

[14] L. MILLIKAN and THE MULTICENTER STUDY GROUP, "Long-term safety and

efficacy with Fibrel in the treatment of cutaneous scars--results of a multicenter study.

Multicenter study group," *J. Dermatol. Surg. Oncol.*, vol. 15, no. 8, pp. 837–842, 1989.

[15] J. Wang, M. K. Lee, S. M. Park, S. Hong, and N. Kim, "A study on the mechanical

properties and deformation behavior of injection molded PMMA-TSP laminated

composite," *Korea Aust. Rheol. J.*, vol. 24, no. 1, pp. 23–33, Mar. 2012.

[16] A. W. Lloyd, R. G. A. Faragher, and S. P. Denyer, "Ocular biomaterials and implants,"

Biomaterials, vol. 22, pp. 769–785, 2001.

[17] M. J. Provenzano, K. P. J. Murphy, and L. H. R. Iii, "Bone Cements: Review of Their

Physiochemical and Biochemical Properties in Percutaneous Vertebroplasty."

[18] A. Aref-Azar, F. Biddlestone, J. N. Hay, and R. N. Haward, "The effect of physical ageing

on the properties of poly(ethylene terephthalate)," *Polymer (Guildf).*, vol. 24, no. 10, pp. 1245–1251, Oct. 1983.

[19]   J. B. Towne *et al.*, "Axillofemoral bypass with externally supported, knitted Dacron grafts: a follow-up through twelve years," *J. Vasc. Surg.*, vol. 17, no. 1, pp. 107–115, Jan. 1993.

[20]   N. Fanous, M. Samaha, and A. Yoskovitch, "Dacron implants in rhinoplasty: a review of 136 cases of tip and dorsum implants," *Arch. Facial Plast. Surg.*, vol. 4, no. 3, pp. 149–156, 2002.

[21]   G. R. Barrett, L. L. Line, W. R. Shelton, J. O. Manning, and R. Phelps, "The Dacron ligament prosthesis in anterior cruciate ligament reconstruction. A four-year review," *Am. J. Sports Med.*, vol. 21, no. 3, pp. 367–373, 1993.

[22]   J. E. Ratner, B. D., Hoffman, A. S., Schoen, F. J., & Lemons, *Biomaterials Science: An Introduction to Materials in Medicine*, 2nd ed. Academic Press, 2004.

[23]   H. Zhang, L. Zhou, and W. Zhang, "Control of Scaffold Degradation in Tissue Engineering: A Review," *Tissue Eng. Part B Rev.*, vol. 20, no. 5, pp. 492–502, Oct. 2014.

[24]   L. N. Woodard and M. A. Grunlan, "Hydrolytic Degradation and Erosion of Polyester Biomaterials," *ACS Macro Lett.*, vol. 7, no. 8, pp. 976–982, Aug. 2018.

[25]   J. R. Martin *et al.*, "A porous tissue engineering scaffold selectively degraded by cell-generated reactive oxygen species," *Biomaterials*, vol. 35, no. 12, pp. 3766–3776, 2014.

[26]   R. Maeda, M. Matsumoto, and K. Kondo, "Enzymatic hydrolysis reaction of water-soluble chitin derivatives with egg white lysozyme," *J. Ferment. Bioeng.*, vol. 84, no. 5,

pp. 478–479, 1997.

[27]   J. C. Middleton and A. J. Tipton, "Synthetic biodegradable polymers as orthopedic devices," *Biomaterials*, vol. 21, no. 23, pp. 2335–2346, Dec. 2000.

[28]   A. Södergård and M. Stolt, "Properties of lactic acid based polymers and their correlation with composition," *Prog. Polym. Sci.*, vol. 27, no. 6, pp. 1123–1163, Jul. 2002.

[29]   O. Bostman, "Osteolytic changes accompanying degradation of absorbable fracture fixation implants," *J. Bone Joint Surg. Br.*, vol. 73-B, no. 4, pp. 679–682, Jul. 1991.

[30]   S. W. Shalaby, *Biomedical polymers : designed-to-degrade systems*. Hanser Publishers, 1994.

[31]   M. A. Woodruff and D. W. Hutmacher, "The return of a forgotten polymer— Polycaprolactone in the 21st century," *Prog. Polym. Sci.*, vol. 35, no. 10, pp. 1217–1256, Oct. 2010.

[32]   S. M. Li, X. H. Chen, R. A. Gross, and S. P. Mccarthy, "Hydrolytic degradation of PCL/PEO copolymers in alkaline media," *J. Mater. Sci. Mater. Med. 2000 114*, vol. 11, no. 4, pp. 227–233, 2000.

[33]   P. Vermette, H. J. Griesser, G. Laroche, and R. Guidoin, *Biomedical Applications of Polyurethanes*. 2001.

[34]   N. M. K. Lamba, K. A. Woodhouse, and S. L. Cooper, *Polyurethanes in biomedical applications*. CRC Press, 1998.

[35]   J. W. Boretos and W. S. Pierce, "Segmented polyurethane: A polyether polymer. An initial evalution for biomedical applications," *J. Biomed. Mater. Res.*, vol. 2, no. 1, pp.

121–130, Mar. 1968.

[36]   J. M. Anderson *et al.*, "Recent Advances in Biomedical Polyurethane Biostability and Biodegradation," 1998.

[37]   H. A. Bayer, O., Siefken, W., Rinke, H., Orthner, L., & Schild, "Process for the Production of Polyurethanes and Polyureas [Verfahren zur Herstellung von Polyurethanen bzw. Polyharnstoffen]," DE728981C, 1937.

[38]   "Polyurethane global market volume 2029 | Statista." [Online]. Available: https://www.statista.com/statistics/720341/global-polyurethane-market-size-forecast/. [Accessed: 05-Jul-2022].

[39]   L. I. Cavaco and J. A. Melo, "Polyurethane : properties, structure and applications."

[40]   E. Delebecq, J.-P. Pascault, B. Boutevin, and F. Ganachaud, "On the Versatility of Urethane/Urea Bonds: Reversibility, Blocked Isocyanate, and Non-isocyanate Polyurethane," *Chem. Rev.*, vol. 113, no. 1, pp. 80–118, 2012.

[41]   M. Špírková and K. Dušek, "Extent of side reactions and gelation of polyether polyurethanes," *Polym. Bull.*, vol. 22, no. 2, pp. 191–198, Aug. 1989.

[42]   "Isocyanate Reactions." [Online]. Available: https://polymerdatabase.com/polymer chemistry/Urethanes.html. [Accessed: 12-Sep-2022].

[43]   Chris Defonseka, *Practical Guide to Flexible Polyurethane Foams*. Shrewsbury: Smithers Rapra Technology Limited, 2013.

[44]   M. Szycher, "Structure–Property Relations in Polyurethanes," in *Szycher's Handbook of Polyurethanes, Second Edition*, CRC Press, 2012, pp. 37–86.

[45]   M. Cabanlit *et al.*, "Polyurethane Shape-Memory Polymers Demonstrate Functional

Biocompatibility In Vitro," *Macromol. Biosci.*, vol. 7, no. 1, pp. 48–55, Jan. 2007.

[46]   P. Singhal, W. Small, E. Cosgriff-Hernandez, D. J. Maitland, and T. S. Wilson, "Low

density biodegradable shape memory polyurethane foams for embolic biomedical

applications," *Acta Biomater.*, vol. 10, no. 1, pp. 67–76, Jan. 2014.

[47]   M. B. B. Monroe, A. D. Easley, K. Grant, G. K. Fletcher, C. Boyer, and D. J. Maitland,

"Multifunctional shape memory polymer foams with bio-inspired antimicrobials,"

ChemPhysChem, vol. 19, no. 16, pp. 1999–2008, Aug. 2018.

[48]   Y. S. Joo, J. R. Cha, and M. S. Gong, "Biodegradable shape-memory polymers using

polycaprolactone and isosorbide based polyurethane blends," *Mater. Sci. Eng. C*, vol. 91,

no. July 2017, pp. 426–435, 2018.

[49]   A. Lendlein, H. Jiang, O. Jünger, and R. Langer, "Light-induced shape-memory

polymers," *Nature*, vol. 434, no. 7035, pp. 879–882, 2005.

[50]   W. M. Huang, B. Yang, Y. Zhao, and Z. Ding, "Thermo-moisture responsive

polyurethane shape-memory polymer and composites: A review," *J. Mater. Chem.*, vol.

20, no. 17, pp. 3367–3381, 2010.

[51]   Q. V. Nguyen, M. S. Lee, J. S. Lym, Y. Il Kim, H. J. Jae, and D. S. Lee, "pH-Sensitive

sulfamethazine-based hydrogels as potential embolic agents for transcatheter vascular

embolization," *J. Mater. Chem. B*, vol. 4, no. 40, pp. 6524–6533, Oct. 2016.

[52]   S. L. Buffington, J. E. Paul, M. M. Ali, M. M. Macios, P. T. Mather, and J. H. Henderson,

"Enzymatically triggered shape memory polymers," *Acta Biomater.*, vol. 84, pp. 88–97,

Jan. 2019.

[53] Q. Ze *et al.*, "Magnetic Shape Memory Polymers with Integrated Multifunctional Shape Manipulation," *Adv. Mater.*, vol. 32, no. 4, p. 1906657, Jan. 2020.

[54] G. J. M. Antony, S. T. Aruna, C. S. Jarali, and S. Raja, "Electrical and thermal stimuli responsive thermoplastic shape memory polymer composites containing rGO, Fe3O4 and rGO–Fe3O4 fillers," *Polym. Bull.*, vol. 78, no. 11, pp. 6267–6289, 2021.

[55] R. Mohr, K. Kratz, T. Weigel, M. Lucka-Gabor, M. Moneke, and A. Lendlein, "Initiation of shape-memory effect by inductive heating of magnetic nanoparticles in thermoplastic polymers," *Proc. Natl. Acad. Sci.*, vol. 103, no. 10, pp. 3540–3545, Mar. 2006.

[56] D. J. Maitland, M. F. Metzger, D. Schumann, A. Lee, and T. S. Wilson, "Photothermal properties of shape memory polymer micro-actuators for treating stroke," *Lasers Surg. Med.*, vol. 30, no. 1, pp. 1–11, Jan. 2002.

[57] J. W. Cho, J. W. Kim, Y. C. Jung, and N. S. Goo, "Electroactive shape-memory polyurethane composites incorporating carbon nanotubes," *Macromolecular Rapid Communications*, vol. 26, no. 5. pp. 412–416, 2005.

[58] M. Behl and A. Lendlein, "Actively moving polymers," *Soft Matter*, vol. 3, no. 1, pp. 58–67, 2007.

[59] A. Lendlein, M. Behl, B. Hiebl, and C. Wischke, "Shape-memory polymers as a technology platform for biomedical applications," *Expert Rev. Med. Devices*, vol. 7, no. 3, pp. 357–379, 2010.

[60] I. Yilgör, E. Yilgör, and G. L. Wilkes, "Critical parameters in designing segmented

polyurethanes and their effect on morphology and properties," *Polymer (Guildf).*, vol. 58, pp. A1–A36, 2015.

[61]   J. Koehler, F. P. Brandl, and A. M. Goepferich, "Hydrogel wound dressings for bioactive treatment of acute and chronic wounds," *Eur. Polym. J.*, vol. 100, pp. 1–11, Mar. 2018.

[62]   E. M. Ahmed, "Hydrogel: Preparation, characterization, and applications: A review," *J. Adv. Res.*, vol. 6, no. 2, pp. 105–121, Mar. 2015.

[63]   E. Lih, J. S. Lee, K. M. Park, and K. D. Park, "Rapidly curable chitosan-PEG hydrogels as tissue adhesives for hemostasis and wound healing," *Acta Biomater.*, vol. 8, no. 9, pp. 3261–3269, 2012.

[64]   Q. Chai, Y. Jiao, and X. Yu, "Hydrogels for biomedical applications: Their characteristics and the mechanisms behind them," *Gels*, vol. 3, no. 1, 2017.

[65]   H. Omidian and K. Park, "Introduction to Hydrogels," in *Biomedical Applications of Hydrogels Handbook*, New York, NY: Springer New York, 2010, pp. 1–16.

[66]   Y. Cheng, X. Luo, G. F. Payne, and G. W. Rubloff, "Biofabrication: programmable assembly of polysaccharide hydrogels in microfluidics as biocompatible scaffolds," *J. Mater. Chem.*, vol. 22, no. 16, p. 7659, 2012.

[67]   B. Balakrishnan, M. Mohanty, P. R. Umashankar, and A. Jayakrishnan, "Evaluation of an in situ forming hydrogel wound dressing based on oxidized alginate and gelatin," *Biomaterials*, vol. 26, no. 32, pp. 6335–6342, Nov. 2005.

[68]   Y. Berkovitch and D. Seliktar, "Semi-synthetic hydrogel composition and stiffness regulate neuronal morphogenesis," *Int. J. Pharm.*, vol. 523, no. 2, pp. 545–555, May

2017.

[69] N. Milašinović, M. Kalagasidis Krušić, Z. Knežević-Jugović, and J. Filipović, "Hydrogels of N-isopropylacrylamide copolymers with controlled release of a model protein," *Int. J. Pharm.*, vol. 383, no. 1–2, pp. 53–61, Jan. 2010.

[70] H. Madry *et al.*, "Thermosensitive Hydrogel Based on PEO–PPO–PEO Poloxamers for a Controlled In Situ Release of Recombinant Adeno-Associated Viral Vectors for Effective Gene Therapy of Cartilage Defects," *Advanced Materials*, vol. 32, no. 2. 2020.

[71] D. Zhang *et al.*, "Carboxyl-modified poly(vinyl alcohol)-crosslinked chitosan hydrogel films for potential wound dressing," *Carbohydr. Polym.*, vol. 125, pp. 189–199, Jul. 2015.

Chapter II

In Vitro and *In Vivo* Degradation Correlations for

Polyurethane Foams with Tunable Degradation Rates

2.1 Introduction

The use of degradable biomaterials for tissue regeneration applications has been widely reported in the literature[1]–[7]. The key capabilities of a degradable scaffold that enable use for tissue regeneration include the ability for cells surrounding the implant site to attach, proliferate, and generate new tissue as the scaffold degrades away. This approach would potentially eliminate the complications associated with scaffold removal after healing. Matching scaffold degradation rate to the tissue regeneration rate is crucial for effective regenerative medicine methods. Scaffold degradation that is too slow relative to tissue regeneration can hinder growth of new blood vessels and tissues, while degradation that is too rapid could case scaffold failure before adequate tissue scaffolding is in place. Other requirements involve matching the mechanical properties of the implant to that of the surrounding tissue, tuning the geometry and porosity of the scaffold to aid implantation and subsequent cell migration into the scaffold, and achieving satisfactory cell-material interactions.

Both synthetic and natural polymers have been explored for use as degradable tissue scaffolds. Some examples of highly tunable, hydrolytically degradable synthetic polyesters include poly-lactic acid (PLLA)[8], polyglycolic acid (PLGA)[9], and poly-dl-lactic-co-glycolic acid (PLGA)[10] due to their high tunability. Additionally, enzymatically degradable synthetic copolymers of α–hydroxy acids and α-amino acids, known as polydepsipeptides[11] are a valuable addition to the existing list of synthetic biodegradable polymers with even greater control over degradability[12] compared to traditional polyesters. Natural polymers, such as collagen[13], proteoglycans[14], alginate-based substrates, hyaluronic acid derivatives[15], and chitosan[15], have been used for tissue engineering applications as well due to their biocompatibility, enzymatically-responsive degradation mechanisms, and/or cell-binding sites.

The diffusion of nutrients and oxygen into tissue scaffolds can be improved by incorporating interconnected pores, especially in the absence of vasculature during the initial stages of wound healing[16], [17]. Furthermore, pore structure can be used as a tool to tune degradation kinetics. Thus, tunable pore structures are important for regenerative medicine scaffolds. Furthermore, the ability to safely implant scaffolds at the wound site is crucial and can be difficult in irregularly shaped defects. Effective implantation can be achieved with shape memory polymers (SMPs). By utilizing the shape memory effect, a porous scaffold can be initially deformed and stored in a low-profile shape that is easy to implant. Upon implantation, scaffold shape change could be triggered by heating to body temperature and exposure to water to enable recovery to the original shape and filling of the wound space. This feature would enable successful scaffold implantation in irregularly shaped wounds, particularly in cases where wound entries are narrower on the outside and wider on the inside, such as in gunshot wounds[18]. Beyond regenerative medicine, degradable SMPs can be used for multiple other applications, such as embolic devices for vascular lesions aneurysms[19][20], hemorrhage control in traumatic wounds[21], and filling up bone defects[22].

One system that meets all these criteria is highly crosslinked thermoset polyurethane SMP foams. These low-density SMP foams have a high volume recovery ratios and tunable volume recovery rates, and their shape change can be triggered by multiple stimuli[23]. Additionally, the low cost and ease of manufacturing, exceptional chemical and physical tunability, and high biocompatibility make polyurethane SMPs an attractive option for various biomedical applications[24], [25]. Several previous approaches have been explored to obtain porous, biodegradable shape memory polyurethanes with this system. The degradation mechanism of these polyurethane SMPs was initially demonstrated by Weems et al. Tertiary amines in the polyol

monomers are susceptible to oxidative degradation, and foam degradation rate depends on the material hydrophobicity[26]. The materials are exceptionally resistant to hydrolytic degradation, even under accelerated conditions.

Several others have tried to further control polyurethane SMP foam degradability. For example, hydrolytically-degradable ester linkages were incorporated into SMP foams using poly(ε-caprolactone) (PCL). While hydrolytic degradation could be tuned with PCL, the overall degradation rate was slow, even in an accelerated hydrolytic degradation medium (0.1M NaOH), and the foams had a low glass transition temperature (T_g, <25°C) that limits their practical use in terms of storing materials in their secondary shapes at room temperature[27]. A faster degradation rate was achieved by Weems et al., wherein succinic acid-based esters were incorporated into SMP foams. In this system, 80% mass loss occurred in a 2% H_2O_2 media over 80 days[28]. However, this relatively hydrophobic SMP required heating to 50°C to achieve complete volume expansion, thus requiring the use of an external heating mechanism to actuate these SMPs post-implantation. Other work by Jang, et al. employed ester-containing monomers to improve thermal and shape memory properties, but this system also degraded slowly[29]. In our recent work, we incorporated esters formed by the reaction between nitrilotriacetic acid (NTA) and diethylene glycol (DEG) to increase the degradation rate while maintaining thermal and shape memory properties. In this system, complete *in vitro* oxidative degradation in 3% H_2O_2 occurred within 30 days[30].

There have also been efforts to slow the degradation rate and obtain biostable SMP foams by replacing tertiary amine-containing polyols with glycerol, isocyanurate, and hexanetriol[31]–[33]. In our recent work, we increased the biostability of porous SMP foams by incorporating diethylene glycol (DEG) and triethylene glycol (TEG). This approach slowed the degradation rate to provide materials with 20% mass remaining after 102 days in 3% H_2O_2[34]. Slowly degrading

27

SMP foams could be valuable for long-term implants and/or for applications in which the material is removed and no degradation is desired prior to explantation.

Multiple animal models have demonstrated the healing capabilities of these SMP foams. A porcine model was used by Rodriguez et al. to evaluate SMP foams for the treatment of intracranial aneurysms[35]. After 90 days of implantation, almost complete penetration of collagen through the foam volume, lack of inflammation, and a thick fibrous cap across the aneurysm neck were observed, demonstrating SMP foam biocompatibility. A SMP foam-coated metal coil was used by Horn et al. to treat a sidewall aneurysm in a porcine model. Approximately 89-93% reduction in the cross-sectional aneurysm area was observed over 180 days after SMP foam treatment, indicating long-term healing capabilities[36]. Weems et al. later continued this research by cleaning the explanted material from aneurysms and qualitatively characterized their degradation using spectroscopy. It was concluded that the *in vivo* mass loss profile was much slower than that obtained *in vitro* using a 3% H_2O_2 solution, which is generally considered to be 'real-time' oxidative degradation media[37][26]. Degradation of SMP foams via multinucleated giant cells with subsequent fibrin deposition was characterized via histological assessment by Jessen et al. using a porcine vascular occlusion model to demonstrate the healing capability of SMP foams[38]. In this model, a steady slow degradation rate of ~3% mass loss/30 days was estimated using cross-sectional area measurements of foam histology images.

Multiple approaches have been used to synthesize SMP foams with desirable physical and shape memory properties and tunable degradation rates. However, there has been inconsistency in *in vitro* characterization in terms of degradation media selection (e.g., H_2O_2 concentration), and focused *in vivo* characterization of SMP foam degradation is limited. It is vital to develop a reliable method for obtaining *in vivo* degradation profiles of SMP foams while confirming their safety.

This method must also be useful for comparing degradation profiles of selected formulations with data that is provided in the literature to rationally select materials with desired degradation outcomes.

In this study, porous SMP foams with previously established tunable *in vitro* degradation rates were utilized, and their *in vivo* degradation profiles were studied using a subcutaneous rat model. This common animal model is often used to evaluate biomaterial scaffold degradation, cellularization, inflammation, and angiogenesis over time, providing a clear point of comparison with previously characterized degradable biomaterials[39]–[44]. Material degradation was carried out over 12 weeks to regularly assess mass loss, scaffold surface chemistry, pore architecture, and histopathological evaluation of cellular infiltration and inflammation. Since previous work has shown that *in vitro* methods fail to accurately predict *in vivo* degradation profiles, samples were subjected to *in vitro* degradation in varying concentration of H_2O_2 (1, 2, and 3%) to identify the medium that most closely predicted *in vivo* degradation profiles[26], [45]. To further complement histological assessment, *in vitro* cytotoxicity analysis of fully degraded samples was performed to assess the material safety using a protocol established by Herting et al.[46] These studies provide fundamental information on correlating *in vivo* and *in vitro* degradation profiles, thereby expanding the characterization of a valuable biomaterial system. This information could be further used to improve the rational *in vitro* characterization of other degradable biomaterials prior to their use in animals.

2.2 Materials and Methods

2.2.1 Materials

Nitrilotriacetic acid (NTA), diethylene glycol (DEG), 1-(3-dimethyl aminopropyl)-3-ethyl carbodiimide HCl (EDC), 4-(dimethylamino) pyridine (DMAP, $\geq$ 99%), N, N, N', N'-tetrakis-2-hydroxypropyl ethylenediamine (HPED), triethanol amine (TEA), hexamethylene diisocyanate (HDI), chloroform, ethanol, acetone, isopropyl alcohol, Triton X-100, phosphate-buffered saline (PBS), and trypsin were purchased and used as received from Fisher Scientific (Waltham, MA, USA). Collagenase (clostridium histolyticum) and pancreatin (porcine pancreas) were purchased from Sigma Aldrich and used as received. Surfactant EPH-190 and catalysts T-131 and BL-22 were used as received from Evonik (Essen, Germany).

2.2.2 SMP fabrication and characterization
2.2.2.1 Ester-containing monomer synthesis

The ester-containing monomer, NTA-DEG, was synthesized as previously described.[30] Briefly, NTA was initially dissolved in chloroform (50 wt%) and activated with 0.1 mol. eq. of DMAP. The combination was allowed to mix for 30 minutes in a round bottom flask at room temperature until all components were completely dissolved. DEG was added dropwise to the flask while maintaining an NTA: DEG ratio of 1:3. Then, EDC was added to the reaction components while maintaining an NTA: EDC ratio of 1:3 to catalyze the reaction between NTA and DEG. The reaction was allowed to proceed at 40°C for 24 hours. Small aliquots were taken on an hourly basis to track rection completion via attenuated total reflectance-Fourier transform infrared spectroscopy (ATR-FTIR, Nicolet, Fisher Scientific, Waltham, MA, USA). Reaction completion was concluded at the appearance of the C=O ester peak at ~1741 cm^{-1}. After completion, excess solvent was evaporated using rotary evaporation and the product was dried overnight under -30 inHg vacuum at 40°C. 1H Nuclear magnetic resonance spectroscopy (NMR, Avance III HD 400 MHz, Bruker)

was performed on the product by dissolving 0.6 mg of product in 1 ml of deuterated chloroform (CDCl$_3$) at 298 K using the TMS/solvent signal as an initial reference. NTA-DEG: ^{1}H NMR (CDCl$_3$; ppm): 3.64 (t,-CH$_2$CH$_2$OCO-), 3.64 (t,-CH$_2$OH), 3.72(s,-CH$_2$N-), 3.78(t,-CH$_2$CH$_2$OH), 4.25(s, - CH$_2$OCO-). NMR confirmed 85-88% functionalization of NTA carboxylic acids with DEG. A schematic of the reaction is shown in **Figure 2.1**.
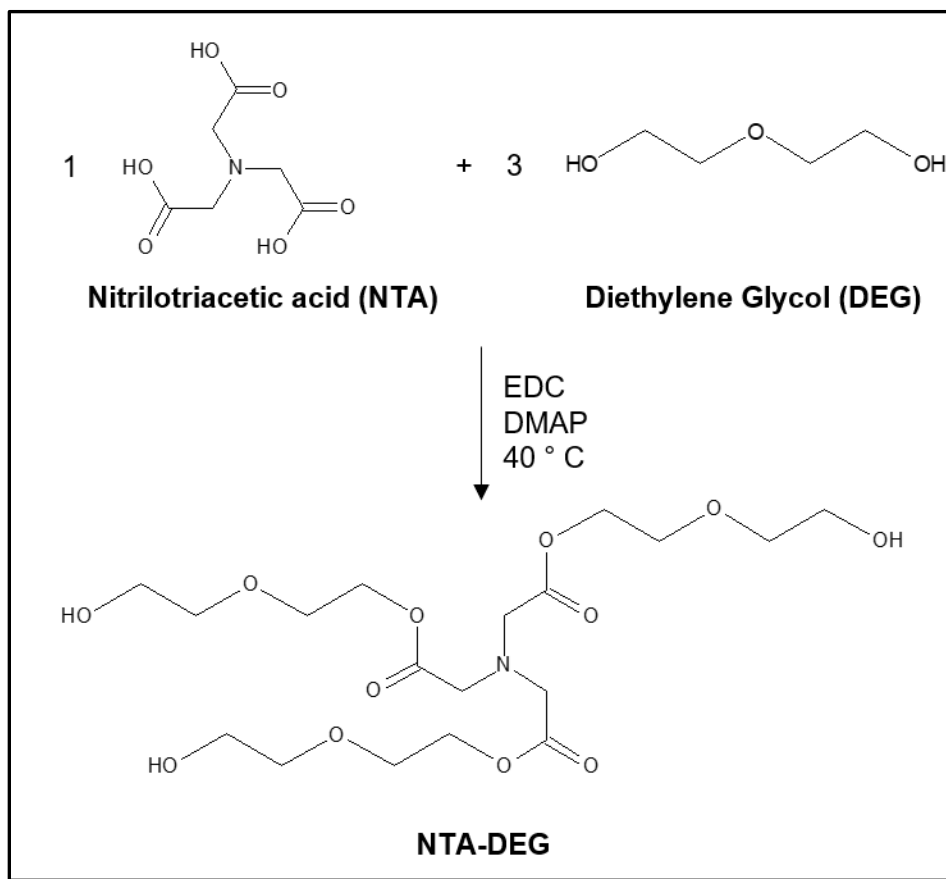
Figure 2.1 Synthesis of ester-containing monomer, nitrilotriacetic acid (NTA)-diethylene glycol (DEG)

2.2.2.2 Foam synthesis

Foams were prepared in a two-part process as previously described.[30], [47]. In the first part, all the required isocyanate equivalents provided by HDI were mixed with 35% of the required

hydroxyl equivalents (NTA-DEG, DEG, HPED, and/or TEA) under an inert dry atmosphere (relative humidity < 200 ppm) in a glovebox (Labconco, Kansas City, MO, USA). This mixture (premix) was allowed to cure in an oven at 50°C for 48 hours. Once the curing was complete, the required amount of surfactant was added to the premix and mixed at 3500 rpm using a speed mixer (Flacktek, Landrum, SC, USA) for 30 seconds before cooling down to room temperature. The second component (hydroxyl (OH) mix) was prepared parallelly. This OH mix consisted of all the balance hydroxyls (HPED, NTA-DEG, water, and/or TEA) along with the gelling (T-131) and blowing (BL-22) catalysts. The OH mix components were mixed in a speed mixer at 3500 rpm for 30 seconds and added to the premix container. Both components were then mixed at 1800 rpm for 5 seconds and poured into a 1-liter container to allow for the foaming process to occur in an oven at 50°C for 10 minutes. The foams quickly rose within 1 to 2 minutes. The prepared foam was kept in a fume hood overnight to ensure complete reaction and release of CO_2 (formed from the reaction between isocyanates and water). Then, foams were removed, cleaned, and dried for further characterization. A schematic representing the formation of foams is shown below in **Figure 2.2**, and **Table 1** contains details on the component content of synthesized foams. All samples were initially cleaned via a total of 4 washes that included 2 washes using deionized water and 2 washes using 70% ethanol, alternatively for 15 minutes each.

Table 2.1 Synthesized foam compositions.

Sample ID	HDI (wt%)	HPED (wt%)	TEA (wt%)	DEG (wt%)	NTA-DEG (wt%)	EPH 190 (wt%)	T-131 (wt%)	BL-22 (wt%)	Water (wt%)
Control	54.03	27.61	8.05	-	-	6.44	0.46	1.01	2.37
30% DEG	53.16	27.15	-	8.69	-	6.19	0.60	1.18	2.91
30% NTA-DEG	43.10	24.40	-	-	21.71	6.17	1.10	1.23	2.29

The surface chemistry of synthesized samples was analyzed using ATR-FTIR at 4 cm^{-1} resolution. Surface chemistry characterization was performed on samples throughout the *in vitro* and *in vivo* degradation processes as well. The characteristic peaks identified to confirm successful synthesis and monitor degradation include carbonyl of urethane at ~1680 cm^{-1}, carbonyl of ester at ~1730 cm^{-1}, ether at ~1090 cm^{-1}, and tertiary amines at ~1050 cm^{-1}.
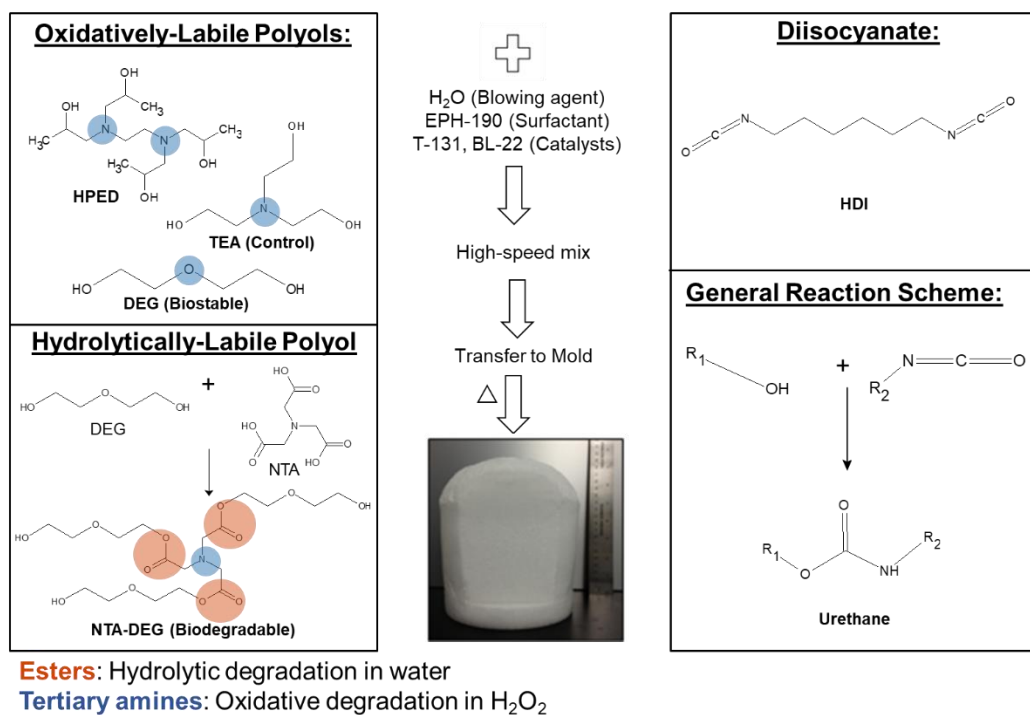
Figure 2.2. Overview of foam synthesis.

2.2.2.3 Pore size analysis

Thin slices (1 cm width, 1 cm length, and 0.5 cm height) were cut from the washed foams along the longitudinal and horizontal axes to analyze the pore structure and size parallel and perpendicular to the foam rise direction. The slices were sputter coated (Desk V Sputter coater, Denton Vacuum, Moorestown, NJ, USA) with a layer of gold for 45 seconds under a vacuum of 50 to 100 mTorr to obtain a gold layer with 10 Å thickness. Sputter-coated samples were mounted

onto a holder, and pore morphology was analyzed using scanning electron microscopy (SEM, JSM 5600, JEOL, Peabody, MA, USA) at 35X magnification and an accelerating voltage of 10kV under a high vacuum to maintain a common scale and contrast level. Pore size was quantified as the largest diameter of all visible pores in an image using ImageJ.

2.2.2.4 Density and Surface Area

Foam density (n=3) was measured by cutting samples into small cubes with each side measuring ~1 cm and weighing them. The length of each face of the sample was measured using calipers and volume was recorded as (length x width x height). Sample weight was divided by the volume to determine the average density of foams. Samples were cut from different sections of foam to ensure that uniform low-density foams were synthesized.

Surface area of samples were calculated using a previously determined correlation between specific surface area and pore size of polyurethane foams, **Equation 2.1**[26]. Slope (20.91944 ± 0.312) and intercept (-11.34565 ± 0.406) were previously obtained by plotting specific surface area (mm^2/mm^3) against known pore size (mm) for each pore. Then, average surface area of samples was calculated using density and specific surface area based on **Equation 2.2**.

$$Specific\ Surface\ Area\ \left(\frac{mm^2}{mm^3}\right) = (Pore\ size\ (mm) * slope) + intercept\ \ldots\ldots\ \textbf{Equation 2.1}$$

$$Surface\ Area\ \left(\frac{cm^2}{g}\right) = \frac{Specific\ Surface\ Area\ \left(\frac{mm^2}{mm^3}\right)}{Densisity\ \left(\frac{g}{cm3}\right)} * 10\left(\frac{mm}{cm}\right)\ \ldots\ldots\ \ \textbf{Equation 2.2}$$

2.2.2.5 Hydrophilicity

Thin slices of nonporous films (5 mm width, 6 cm length, and 1.5 cm height) were prepared from the same compositions listed in **Table 2.1**, without the addition of surfactant or water

(blowing agent) and used to measure hydrophilicity. The contact angle was measured using a goniometer (Model 500, Ramé-hart Co, Succasunna, NJ). Water droplets (2 ml, n=6) were dropped onto each film, and images were captured at a 0.01-second interval using a high-speed camera (SuperSpeed U4 series). Samples were raised to touch the droplet to eliminate droplet spreading due to gravitational impact. Images were analyzed using DROPImage software to determine the contact angle between the water droplet and the film being tested. An average of 100 measurements were used for each droplet to determine the contact angle.

2.2.2.6 Thermal and Mechanical Analysis

Samples (n=3) were cut into thin slices (5 to 10 mg), placed in a platinum pan, and heated from 0 to 600°C at a rate of 10°C/min to measure the temperature at which 0.5% of the mass was lost to thermal degradation using Q500 Thermogravimetric Analyzer (TA Instruments, New Castle, DE, USA). This temperature (Control – 142 °C, 30% DEG – 131 °C, 30% NTA-DEG – 141 °C) was noted as the upper limit to which the samples could be safely heated without undergoing any thermal degradation for future analysis.

To measure glass transition temperature (T_g), samples (n=3) were cut into thin slices (3 to 5 mg) and loaded into t-zero aluminum pans with lids (DSC 84009, DSC consumables, TA instruments, New Castle, DE, USA). The samples were placed onto DSC Q200 (TA Instruments, New Castle, DE, USA), equilibrated at -40 °C, held isothermally for 2 minutes, heated to 120°C at a rate of 10°C/min, held isothermally for 2 minutes, cooled to -40°C at a rate of 10°C/min, held isothermally for 2 minutes, and heated back to 120°C at a rate of 10°C/min. The half-height transition temperature of the endothermic shift during the second heating cycle was recorded as dry T_g.

To measure the wet T_g, samples (n=3, 3 to 5mg) were placed in water at 50°C for 12 minutes to allow for plasticization and then loaded in t-zero aluminum pans with hermetic lids. Samples were equilibrated at -60°C, held isothermally for 2 minutes, heated to 100°C at 10°C/min, and held isothermally for 2 minutes. Wet T_g was recorded as the half-height transition temperature during the endothermic shift in the single heating cycle.

Samples (n=5) were cut into dog bones (ASTM D638 scaled down by a factor of 4) with a gauge length of 6.25 mm and width of 1.5 mm. The thickness of each sample was measured before testing to measure the cross-sectional area under consideration. Samples were subjected to a tensile force using a tensile tester (Test Resources, Shakopee, MN, USA) via a 24 N load cell. The tensile force was applied at a rate of 2 mm/min until failure, and the resulting stress/strain curve was used to measure elastic modulus, ultimate tensile strength, and elongation at break. To test samples in wet conditions, they were cut according to the same ASTM standards mentioned above, placed in a vial containing deionized water at 50°C for 1 hour, patted dry, and clamped to the tensile tester for analysis.

2.2.2.7 Shape Memory Behavior

Shape memory behavior was measured by allowing the samples to recover their volume in a water bath at 37°C. Samples (n=3) were cleaned and dried before use. Each sample was cut into a cylindrical geometry (diameter = 8 mm, length = 1 cm) and nitinol wire (diameter = 330 µm) was threaded through the foam longitudinally to hold it in place. Samples were heated to 70°C for 10 minutes (i.e., above their T_g), crimped using a radial crimper (Blockwise Engineering, Tempe, AZ, USA) into a smaller deformed geometry, and cooled in the crimper for 15 minutes at room temperature. This process allowed for programming (i.e., fixing) the temporary shape. The crimped volume was measured using calipers to determine the amount of crimping attained.

36

Samples were then placed in an airtight container for 24 hours and the crimped volume was measured once again to determine shape fixity according to **Equation 2.3**. After 24 hours, samples were placed in a water bath at 37°C for 10 minutes, and images were captured at a 5-second interval to record the volume change. ImageJ was used to measure the volume of the sample at each time point (t). Sample volume recovery was measured according to **Equation 2.4**.

$$Shape\ Fixity\ (\%) = 1 - \frac{Crimped\ volume_{24\ hr} - Crimped\ volume_{0\ hr}}{Crimped\ volume_{0\ hr}} * 100\% \ \ldots\ldots \ \text{Equation 2.3}$$

$$Volume\ Recovery\ (\%) = \frac{Sample\ volume\ (t)}{Expanded\ volume} * 100\ \% \ldots\ldots\ldots\ldots\ldots\ldots\ldots\ldots\ldots\ldots\ldots \ \text{Equation 2.4}$$

2.2.3 Cytocompatibility

2.2.3.1 Indirect Cytocompatibility

Before testing samples (n=3) were cut into small cubes (each side measuring ~1 cm) and cleaned as described in Section 2.2.2. Samples were then soaked in PBS overnight to ensure complete removal of ethanol and placed on Transwell® inserts in pre-seeded 24-well plates containing NIH mouse fibroblast 3T3 cells (10,000 cells per well between passage #4 and 6) that had been cultured for 24 hours in Dulbecco's Modified Eagle Medium (DMEM) supplemented with 10% fetal bovine serum (FBS) and 1% penicillin-streptomycin (PS) at 37°C. This study, based on ISO-10993-5 standards, indirectly measures potential effects of foam leachable in the media on cell viability and is useful for biomaterials that do not have specific attachment sites for cells[47]. Cell morphology was assessed using a Zeiss Axiovert inverted microscope to confirm even cell distribution before proceeding. Wells that contained empty inserts over cells were used as positive cytocompatible controls. Negative cytotoxic controls included wells seeded with cells

that had 0.5% H_2O_2 added to cause cell death. Cell viability was quantified using a Resazurin assay at 3, 24, and 72 hours. Transwell inserts and samples were removed from the wells, and media was replaced with Resazurin cell viability stain for 2 hours at 37°C before measuring fluorescence at 570 nm using a microplate reader (FLx900, Bio-Teck Instruments Inc). Cell viability was measured according to **Equation 2.5**:

$$\text{Cell Viability (\%)} = \frac{Abs_{570}(\text{x})}{Abs_{570}(Control)} \times 100\% \quad \ldots\ldots\ldots\ldots\ldots\ldots \quad \text{Equation 2.5}$$

where x is the selected treatment group, and the cytocompatible empty insert control was used as a standard with 100% viability.

2.2.3.2 Foam degradation byproduct cytocompatibility

To test degradation byproduct cytocompatibility, cleaned foams (not implanted in rats) were allowed to undergo complete degradation under accelerated conditions in 30% H_2O_2 at 70°C as previously described by Herting et al[46]. A line was marked in each vial to maintain 15 ml of degradation media per cylindrical samples (8 mm diameter, 1 cm length). Degradation media was regularly replenished when the level of media dropped below the 15 ml line due to evaporation. The solutions were then diluted to 2% H_2O_2 and hydrogen peroxide content was neutralized using catalase (1500 U/mL) for 7 days at 37°C. Complete neutralization was confirmed using a ferric thiocyanate kit (Chemetrics). The neutralization process was repeated until no more traces of H_2O_2 were detected. The concentration of remaining catalase was measured using Pierce Coomassie Plus Protein Assay (ThermoFisher Scientific, Waltham, MA, USA). The solutions were then filtered through a 0.22 µm filter. A serial dilution was performed on the filtered degradation byproducts in cell culture media to analyze their cytocompatibility. The solutions were placed on top of 3T3 mouse fibroblasts pre-seeded in wells for 24 hours as described above. At 3 hours, cell

viability was measured relative to media-only controls using the resazurin assay according to **Equation 2.5**.

2.2.4 Degradation characterization

2.2.4.1 *In vitro* degradation profiles.

Varying concentrations of H_2O_2 (1, 2, and 3%) were prepared as oxidative degradation media to analyze *in vitro* degradation profiles at 37°C. Characterization was focused on oxidative degradation based on previous studies showing that these materials are stable in hydrolytic media[47], [49], [50]. Samples (n=3) were cut into cylindrical geometries (diameter = 8 mm, length = 1 cm) and incubated in vials with 15 ml of media. To replicate previous work, one sample set was used throughout the entire degradation process[26], [29], [30], [34]. Samples were removed from media, washed in 70% ethanol, dried under vacuum at 40°C, weighed at each time point, and then returned to fresh media for continued analysis. This technique is referred to as the 'Literature Method' here. To compare the effects of repeated washing/drying on the *in vitro* characterization process, a parallel study was carried out in which unique samples sets were prepared for each time point. Weights of these sacrificial samples were recorded after washing and drying and then samples discarded. This technique is referred to as the 'Optimized Method' here. In both studies, degradation media was replaced twice every week, and samples were characterized at 1, 2, 3, 4, 6, and 12 weeks. Pore size (2.2.2.3), thermal (2.2.2.5), and spectroscopic (2.2.2.2) analyses were performed at each time point as explained above.

2.2.4.2 Sterilization

Cleaned samples (n=36) were cut in similar cylindrical (diameter = 8 mm, length = 1 cm) shapes as those used in *in vitro* characterization and sterilized via UV-C light (UV sterilizer and sanitizer cabinet, Skin Act, Pacoima, CA, USA) at 240 nm for 4 hours at room temperature. Samples were characterized in terms of mass, Tg, pore size, and surface chemistry to ensure that sterilization did not significantly affect any measured property, **Figure 2.4**.

2.2.4.3 Surgical Procedure

All procedures were performed per policies set by Syracuse University's Institutional Animal Care and Use Committee (IACUC) under the guidance provided by the American Veterinary Medical Association (AVMA). A total of 36 female *Sprague Dawley* rats, aged at 11 weeks were selected to enable easy comparison with previous studies[49]–[54]. The rats were acclimatized to their surroundings for 1 week. For surgeries, each rat was anesthetized by administering 2% inhalation isoflurane with oxygen at 2 ml/min via a nose cone for at least 5 minutes while being placed on a heating pad to maintain body heat. Anesthesia was maintained throughout the procedure. Petroleum jelly was applied to the eye to avoid dehydration. Incision sites (two per rat) were trimmed to remove fur and cleaned using one wipe of skin cleanser (chlorhexidine gluconate) and isopropyl alcohol across the boundary of the intended incision site. Four subcutaneous pockets were created (two per side) by first cutting a small opening using sterilized hemostats and sharp scissors. The pockets were expanded to a length of ~1.5 cm using blunt scissors to break the connective tissue. The outer skin was held open via hemostats and sterilized samples (two per incision) were implanted into each subcutaneous pocket using forceps. The implantation location for each sample was rotated amongst the ventral and lateral locations to avoid sample/location-based bias. Each incision site was then sealed using wound clips (5 mm,

Braintree Scientific). After closing the wounds, incision sites were cleaned using isopropyl alcohol, and the anesthesia cone was removed. Rats were allowed to wake up, placed back into their respective cages (2 per cage), and allowed to rest. Six replicates were prepared for each time point.

2.2.4.4 Post-operative procedure

Two drops of bupivacaine (0.1 ml) were dropped onto each incision site once a day for 72 hours as a pain reliever. A subset (six) of rats were sacrificed at each time point – 1, 2, 3, 4, 6, and 12 weeks – via CO_2 asphyxiation according to the AVMA guidelines on euthanasia. Cervical dislocation was performed to confirm euthanasia before explanting samples from each rat. Out of the samples collected, 5 samples per each formulation were used for *ex vivo* characterization while 1 sample was preserved using 4% formaldehyde and shipped to Histowiz® (Brooklyn, NY, USA) for histological staining.

2.2.4.5 *Ex vivo* sample characterization

Post explantation, samples were cleaned thoroughly to remove attached tissue and blood to enable characterization as per the protocol provided by Zhang et al[55]. Briefly, samples were initially subjected to three enzyme washes for a total period of 72 hours with the surrounding solution replaced every 24 hours. The enzymatic solution contained equal parts of collagenase (500 units/ml buffer), pancreatin (0.5g/100 ml buffer), and trypsin (0.5%). Collagenase buffer contained 0.05 M Tris-HCl (pH 7.5), 0.36 mM $CaCl_2$, and 0.02% w/v sodium azide. Pancreatin buffer contained 0.025 M Tris-HCl (pH 7.5) and 0.02% w/v sodium azide. Samples were rinsed in a 10% Triton X-100 solution for 24 hours, with the solution being replaced every 6 hours to remove any remnants of enzymes. Then, samples were subjected to a deionized water wash for 24 hours,

with water replaced every 3 hours to remove surfactant. Non implanted samples were subjected to the same enzymatic washing procedure as a control. All washed samples were characterized in terms of mass loss, T_g (DSC), pore structure (SEM), and surface chemistry (FTIR). No significant differences were found in non-implanted sample masses before and after washing (p>0.05 for all). Pore sizes of control and DEG foams were reduced after washing, and T_g of control foams was reduced. No notable changes in surface chemistry were found in FTIR analysis. Overall, the enzyme wash had small effects on foam properties; however, due to the changes that were measured, washed foams were used as controls to ensure that the enzyme wash was accounted for in the *in vivo* vs. *in vitro* degradation measurements.

2.2.4.6 Histological assessment

Samples were sectioned along their longitudinal axis, stained with hematoxylin and eosin (H&E), placed in immersion oil, and scanned via 100x objective. To avoid bias, a blind assessment of resulting images was performed by two pathologists. Collagen deposition was measured in each sample by analyzing collagen density and organization (no collagen/organization, immediate density/organization, and high density/organization). A debris score of none, minimal, mild, moderate, and severe was assigned based on the amount of residual fibrin, hemorrhage, and necrosis observed in each sample[56]. Surrounding tissues were ranked based on the level of inflammation observed. Individual inflammatory cells were counted in 9 high power fields (HPFs, defined as ~0.01 mm^2) per sample. Inflammatory cell types that were identified and counted include neutrophils, lymphocytes, eosinophils, plasma cells, and macrophages (including giant cells, erythrophagocytic cells, and hemosiderin-laden macrophages). Each implant was then given an overall tissue response score based on inflammation, neovascularization, and ECM content analysis[38].

2.2.5 Statistical analysis

Measurements are presented as mean ± standard deviation. The number of measurements were maintained at three for all analysis. Student's t-tests (2-sample, assuming unequal variance) were performed between time points as mentioned in each figure legend. Statistical significance was accepted as $p < 0.05$

2.3. Results and Discussion

2.3.1 Density, Pore Structure, and Surface Area

As shown in **Table 2.2**, all foams had comparable pore sizes of ~1100-1300 µm, which enables easy comparison with previously published research on SMP foam degradation[26], [29]. Open pores with high interconnectivity were observed in DEG and NTA-DEG foams, while control foams had relatively closed pores with pinholes between adjacent pores, as shown in **Figure 2.9**. This increased interconnectivity along with sufficiently large pores would allow for nutrient and waste transport and tissue and blood vessel ingrowth during the wound healing stages[57], [58]. Low target densities well below 0.1 g/cm^3 were obtained in all foams, indicating that successful foaming occurred with all formulations. Highly porous, low density foams can be crimped into smaller constricted geometries during shape fixation, which would enable easy implantation. Increased surface areas were observed in foams with larger pores and lower densities, with the highest surface area calculated for 30% DEG foams.

While there are other methods, such as Brunauer–Emmett–Teller (BET) to measure surface area, and Barret Joyner and Helenda (BJH) that can measure pore diameter, pore volume and distribution based on gas absorption techniques, using a traditional technique such as SEM allows for easy comparison with previously published work on biomaterial foams. In previous attempts to use BET to measure surface area of these polyurethane foams, it was observed that the foams underwent saturation before an entire Langmuir isotherm could be plotted. Hence, the equation mentioned in methods section was used to measure surface area for this work, which enables comparison between the synthesized formulations.

Table 2.2 Physical characterization of foam pore size, density, surface area, contact angle, shape recovery (time to 100% volume expansion in 37°C water) and % Shape Fixity. n = 6 for pore size, density, surface area and contact angle. n=3 volume recovery and shape fixity. mean ± standard deviation displayed. *p<0.05 relative to control foam.

Sample	Pore size (µm)	Density (g/cm³)	Surface Area (cm²/g)	Contact Angle (°)	Time to 100 % volume recovery (s)	% Shape Fixity
Control	1100 ± 300	0.045 ± 0.001	1857 ± 431	87 ± 3	230 ± 80	92 ± 6
30% DEG	1300 ± 200 *	0.027 ± 0.002*	22727 ± 217*	61 ± 4*	190 ± 10*	91 ± 5
30% NTA-DEG	1100 ± 100	0.026 ± 0.005*	3466 ± 617*	52 ± 2*	40 ± 20*	86 ± 2

2.3.2 Thermomechanical properties

The contact angle measured on each film followed expected trends based on monomer structures, **Table 2.2**. The highest contact angle of 87° was observed in the control formulation, while 30% DEG had a slightly lower contact angle of 61° due to the presence of increased hydrophilic ether linkages. Ester-containing formulations (30% NTA-DEG) had the lowest contact angle (52°) due to increased hydrophilicity provided by NTA-DEG esters and ethers. The increased pore interconnectivity observed in DEG and NTA-DEG foams may be related to the relatively higher hydrophilicity of these monomers, which increased monomer interactions with surfactants and the aqueous blowing agent during the foaming process.

Dry T_g was found to be above 40°C for all formulations, **Table 2.3**. A dry T_g above room temperature ensures that SMP samples can be stably stored in their secondary shape at ambient conditions without undergoing premature shape memory actuation before the intended time of usage. In this system, heat-induced plasticization is utilized during programming and shape fixing. The polymers are heated above their T_g in the dry state, which breaks hydrogen bonds between urethane linkages to make foams soft and malleable and enable compression into the temporary shape. Subsequent cooling of compressed foams allows for formation of new hydrogen bonds between deformed chains to fix the shape in the required geometry. This shape memory behavior

45

enables foam storage in a temporary, deformed state before implantation. A low-profile shape facilitates the application of foams to narrow or irregularly shaped wounds and/or delivery of foams via catheter. This property has been harnessed in previous *in vitro* and *in vivo* models to demonstrate that SMP foams can be easily implanted into the body.[62], [63] Here, all foams had high shape fixity (>85%) over 24 hours of storage at room temperature, with general decreases in shape fixity with increased hydrophilicity, **Table 2.2**. This result is attributed to more hydrophilic foams absorbing ambient water during storage.

Wet T_g below body temperature ensures that samples can passively recover their original shape once exposed to water after implantation in the body within the required time frame, **Table 2.3**. In general, compressed foams recover their shape when the switching segments (hydrogen bonds between the urethane linkages) are broken, either by heating above the T_g in the dry state or by water-induced plasticization and heating above the reduced wet T_g. In these studies, plasticization and subsequent volume recovery occurred within 4 minutes in across all formulations in *in vitro* tests in 37°C water, as shown in **Table 2.2**. Faster volume recovery in NTA-DEG and DEG foams is attributed to relatively higher hydrophilicity that enables faster water penetration, thereby reducing the time required to plasticize the network and induce shape recovery. Moreover, an open pore structure could also facilitate water penetration in the NTA-DEG foams, which had the fastest volume recovery. If these materials were exposed to water in the body after implantation, a fast volume recovery ensures that foams can rapidly expand to their original shape and seal wounds. This feature has potential benefit in a number of healing applications, such as gunshot wounds that are narrower on the outside and larger towards the inner sides due to the tumbling of bullets within the tissue[66], [67].

	Dry Conditions				Wet Conditions			
Sample	**Elastic Modulus (kPa)**	**Ultimate Tensile Strength (kPa)**	**Ultimate Elongation (mm/mm)**	**T_g (°C)**	**Elastic Modulus (kPa)**	**Ultimate Tensile Strength (kPa)**	**Ultimate Elongation (mm/m)**	**T_g (°C)**
Control	3200 ± 1700	530 ± 230	0.2 ± 0.1	53 ± 2	150 ± 20	55 ± 20	0.4 ± 0.2	30 ± 2
30% DEG	140 ± 40*	90 ± 30*	2.4 ± 0.7*	45 ± 2*	32 ± 6*	40 ± 10*	1.7 ± 0.4*	22 ± 3
30% NTA-DEG	80 ± 30*	90 ± 10*	1.4 ± 0.6*	40 ± 2*	15 ± 3*	70 ± 20*	4.5 ± 1.3*	29 ± 1

Table 2.3 Thermal and mechanical properties of SMP foams. n = 5 for all mechanical measurements. n = 3 for glass transition temperature (T_g) measurements. mean ± standard deviation displayed. *$p<0.05$ relative to control.

Table 2.3 shows tensile properties of samples in both dry and wet conditions as an indication of properties before and after implantation, respectively. Control foams had the highest elastic modulus and tensile strength and lowest elongation under dry conditions, which is attributed to increased crosslinking in the network due to the use of tri-functional polyols with shorter arms (as compared with diols in DEG foams and triols with longer arms in NTA-DEG foams, **Figure 2.1**). As expected, modulus and strength decreased and elongation generally increased in wet conditions, due to softening of SMP foams after water plasticization. DEG and NTA-DEG foams had wet elastic modulus values <30 kPa, which is comparable that of human forearm skin (40 kPa) [64] and of subcutaneous rat tissue (65 kPa).[65] Lower stiffness ensures that samples do not impart unwanted stress onto the surrounding tissues after expanding within the wound site into which they are implanted.

2.3.3 Degradation Analysis: *In Vitro* and *In Vivo* Correlations

2.3.3.1 *In Vitro* Protocol Refinement

During prior *in vitro* studies, it was observed that 30% NTA-DEG foams underwent complete mass loss within 30 days in 3% H_2O_2[30]. Control foams had 100% mass loss within 12 weeks, and 30% DEG foams had 23% mass remaining after 14 weeks in a 3% H_2O_2 solution[34].

The methods used to collect this data is referred to as the 'Literature Method' here. This method subjects samples to repeated washing and drying procedures at each time point and returning characterized samples to media for further testing at later time points.[26], [28], [32], [68], [69]

While analyzing mass loss profiles during *in vivo* degradation, it was observed that 30% NTA-DEG had ~29% mass remaining, 30% DEG foams had 80% mass remaining, and control foams had 62% mass remaining after 12 weeks, **Figure 2.5**. This result shows that while the general trends in mass loss rates remained the same, with 30% NTA-DEG undergoing the fastest degradation, followed by control foams having an intermediate degradation rate, and 30% DEG undergoing the slowest degradation, the overall degradation rate was much slower *in vivo* compared to previously observed *in vitro* degradation rates measured under presumed real-time conditions.

To address this issue, a parallel study was carried out to find testing conditions that could more closely correlate *in vitro* and *in vivo* degradation. In this 'Optimized Method,' multiple concentrations of H_2O_2 were employed, and separate sacrificial samples were used to record mass loss at each time point to better mimic *in vivo* testing procedures and reduce effects of washing/drying on later measurements. At each time point, the sacrificial sample was removed from the degradation media, rinsed in 70% ethanol, vacuum dried, weighed, and characterized. The sacrificial samples were discarded after characterization was complete and not returned to the study.

Significant differences were observed between the degradation profiles obtained in 3% H_2O_2 solution at 37°C using the 'Literature Method' and the 'Optimized Method', as shown in **Figure 2.3a**. Faster degradation was observed in the 'Literature Method,' which was attributed to additional physical erosion experienced by samples due to repeated washing and drying procedures

at each time point. These physical forces were minimized in the 'Optimized Method,' as the samples were not subjected to multiple wash/dry cycles over time. SEM micrographs captured on samples characterized using the 'Optimized Method' demonstrate improved pore morphology retention after 6 weeks compared with 'Literature Method' samples, **Figure 2.3b**. No notable differences were seen during spectroscopic and thermal analyses of samples subjected to the two different methods, **Figure 2.3c-d**. This result indicates the validity of the hypothesis that changing testing procedures reduced undesired physical erosion and did not alter the chemical degradation process of the polymer network.
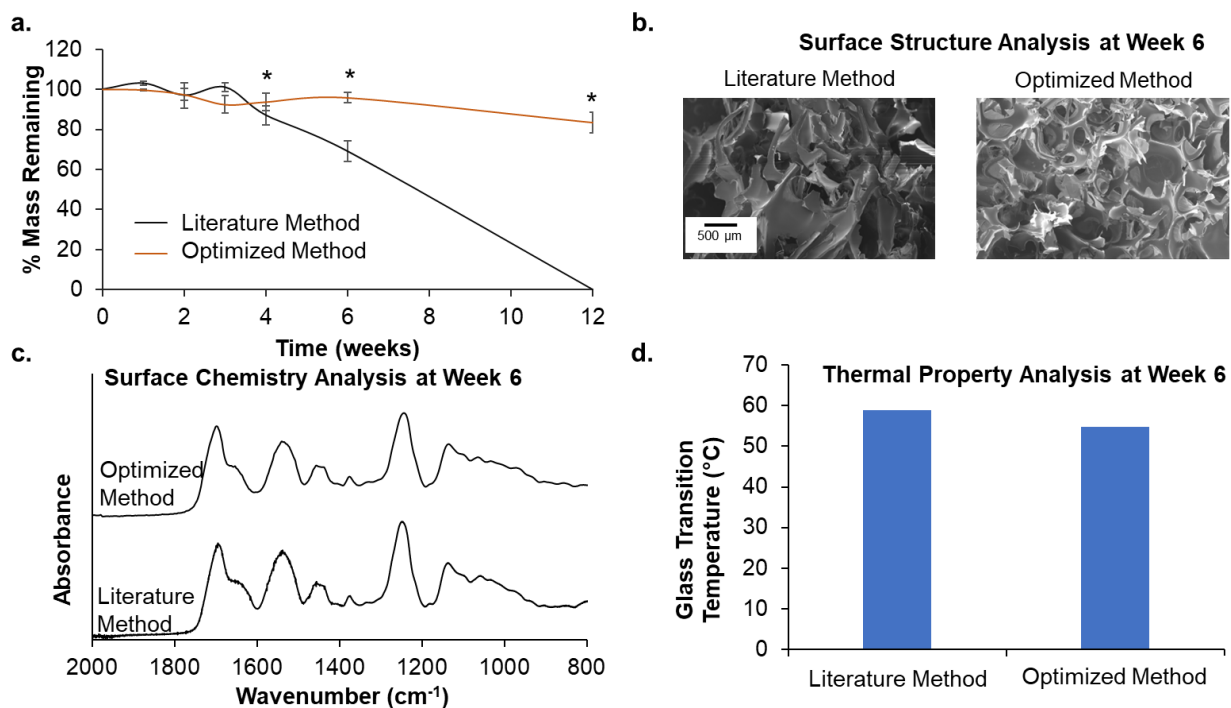
Figure 2.3 Comparison between Literature Method (re-testing samples at each time point) and Optimized Method (testing sacrificial samples once at set time points) of *in vitro* degradation characterization in terms of (a) mass loss, (b) pore structure, (c) surface chemistry, and (d) thermal properties of control foams. *$p<0.05$ between methods, no statistical significance was observed in thermal properties between methods ($p>0.05$).
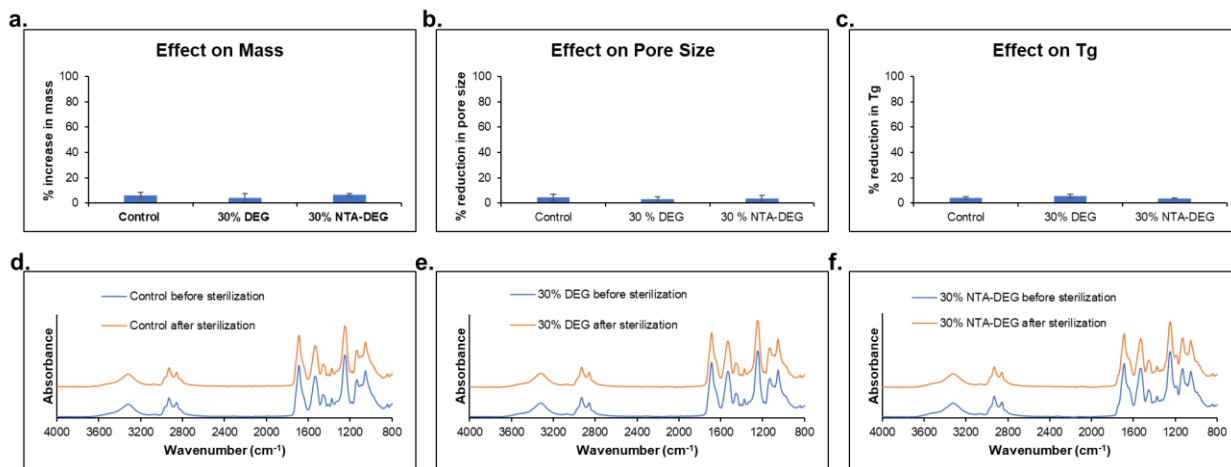
Figure 2.4. Characterization of the effects of UV-C radiation exposure for 4 hours at room temperature on foam (a) mass, (b) pore size, (c) Tg, and (d-f) surface chemistry of Control, 30% DEG, and 30% NTA-DEG foams, respectively. No statistical differences were measured for any characterized property before and after sterilization ($p > 0.05$).
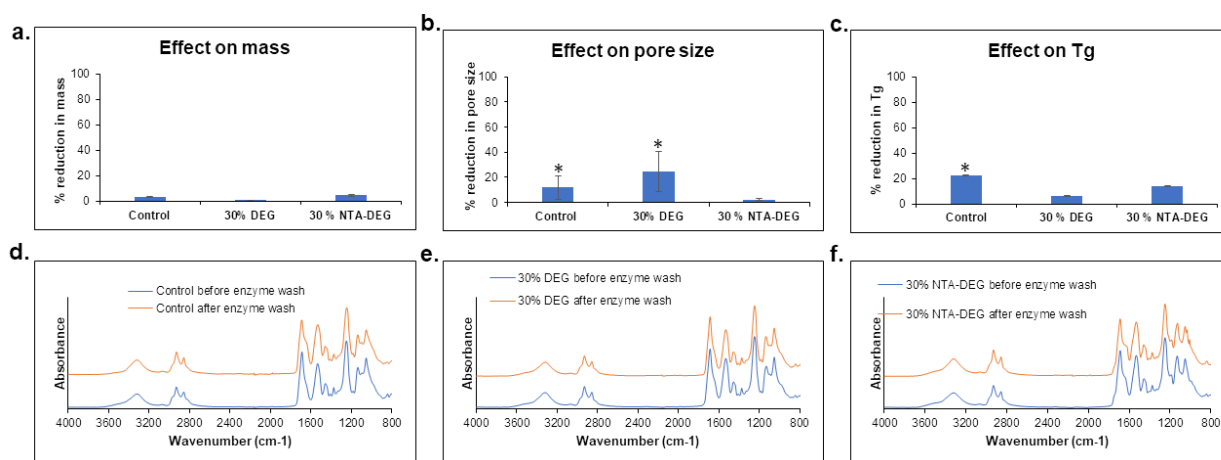
Figure 2.5. Characterization of the effects of the enzyme wash procedure (described in Section 2.4.5) on foam (a) mass, (b) pore size, (c) Tg, and (d-f) surface chemistry of Control, 30% DEG, and 30% NTA-DEG foams, respectively. *$p < 0.05$ relative to sample before washing. No statistical differences were measured for mass before and after sterilization ($p > 0.05$).

2.3.3.2 Mass Loss

After ensuring that unwanted effects of additional physical erosion were minimized and that pre- and post-explantation processing was accounted for (**Figures 2.4 and 2.5**), the optimized method was employed with varying concentrations of H_2O_2 to determine *in vitro* conditions that best mimic *in vivo* degradation for each composition. According to ISO 10993-13, 3% H_2O_2 is reported to have comparable levels of reactive oxygen species (ROS) found in wound sites[65], [66]. However, hydrogen peroxide has a higher stability compared to other ROS, and it can more easily penetrate through samples membrane and tissues and remain within samples for a longer time[72]. Thus it is likely that 3% H_2O_2 provides higher levels of degradative species compared to ROS levels *in vivo*[67], and we therefore chose to characterize degradation in 1 and 2% H_2O_2 to enable comparison between *in vitro* and *in vivo* studies, **Figure 2.6**.
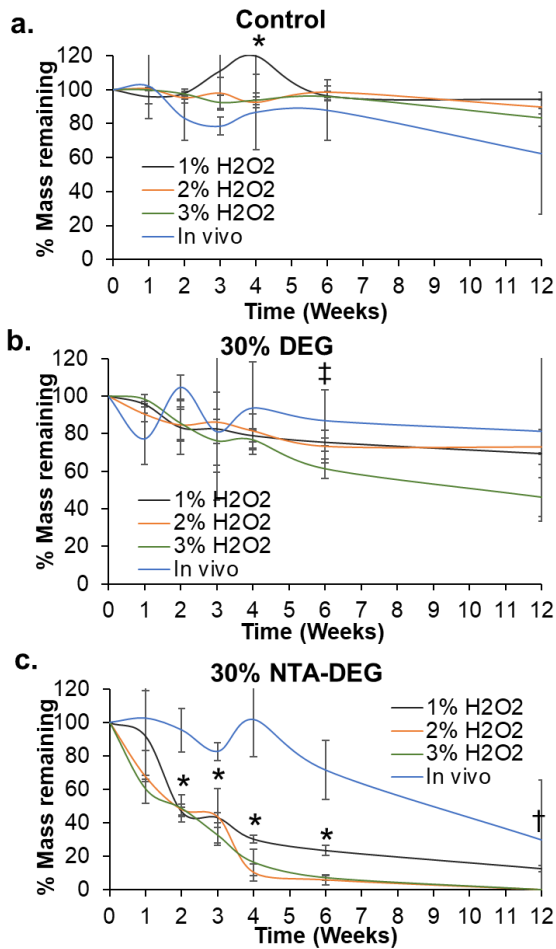
Figure 2.6 Comparison between *in vitro* (n=3) and *in vivo* (n=5) mass loss profiles of (a) control, (b) 30% DEG, and (c) 30% NTA-DEG foams. *In vitro* degradation was carried out in varying concentrations of H_2O_2 (1%, 2%, and 3%). *In vivo* degradation data was collected after subcutaneous implantation in rats over 12 weeks. Mean ± standard deviation is displayed. *p<0.05 between all in vitro measurements and in vivo measurement at same time point. †p<0.05 between 2% and 3% H2O2 measurements and in vivo measurement at same time point. ‡p<0.05 between 3% H2O2 measurements and in vivo measurement at same time point.

In this study, it was found that the H_2O_2 solution that best mimicked *in vivo* degradation conditions depended on the material chemistry and hydrophobicity. The general trends in

degradation rates in each medium were still the same, with the order degradation rate as follows: 30% NTA-DEG > Control > 30% DEG. The mass loss profile for control foams obtained using 3% H_2O_2 was a close match to that obtained *in vivo*, **Figure 2.6a**, with statistically comparable measurements taken out to 12 weeks of degradation. This result can be attributed to the oxidative degradation mechanism of control foams via scission of tertiary amines and high hydrolytic stability, as described in previous work[26].

Compared to control foams, 30% DEG foams are slightly more hydrophilic, which enables faster water penetration, which could increase access of ROS to polymer chains to accelerate degradation. Additionally, DEG foams are susceptible to oxidative degradation of both tertiary amines provided by HPED and ether groups provided by DEG. However, ether linkages can undergo parallel crosslinking during oxidation as previously demonstrated by Christenson et al[68]. This property may lead to simultaneous chain scission to induce degradation and chain crosslinking to increase stability during the degradation process[34], which complicates degradation estimations and slowed overall degradation rates in this SMP foam system. Thus, lower concentrations of 1 and 2% H_2O_2 most closely mimicked *in vivo* degradation profiles for 30% DEG foams, as shown in **Figure 2.6b**, with statistically comparable measurements at all time points until week 6 (p-value = 0.022).

Similarly, a lower concentration of 1% H_2O_2 proved to have a closer match to *in vivo* degradation profiles for 30% NTA-DEG foams, as shown in **Figure 2.6c**, but *in vitro* degradation was significantly faster after 2 weeks for all H_2O_2 concentrations as compared with *in vivo* degradation rates, except for week 12, where 1% H_2O_2 samples had a comparable mass to the *in vivo* samples. These relatively hydrophilic 30% NTA-DEG foams are susceptible to hydrolytic cleavage of NTA-DEG ester groups, oxidative breakdown of tertiary amines on HPED, and

oxidative cleavage and/or crosslinking of ether groups within DEG. In addition to the possible effects of hydrophilicity mentioned above, ester hydrolysis leads to the formation of hydroxyls and carboxylic acids. The acidic byproduct (carboxylic acid) can catalyze hydrolysis to increase the overall degradation rate in aqueous conditions[69]. We hypothesize that samples were protected from reactive agents by fibrous encapsulation after *in vivo* implantation to slow degradation rates relative to the *in vitro* measurements. For further analysis, data collected from degradation in 3% H_2O_2 will be used to analyze control foams, and data collected from incubation in 1% H_2O_2 will be used to analyze 30% DEG and 30% NTA-DEG foams.

2.3.3.3 Physical Analysis: Pore Morphology

Overall, pore morphology was maintained across all formulations during *in vivo* degradation as shown in **Figure 2.7**. Control foams lost their pore structure with visible strut breakage after 4 weeks of *in vitro* degradation in 3% H_2O_2. During *in vivo* degradation, control foam had some strut breakage beginning at week 6, but overall pore structure was maintained throughout the 12 weeks, and no loss in pore structure was seen. Amongst 30% DEG foams, increased pore stability was observed compared to control foams, as expected. During *in vitro* degradation in 1% H_2O_2, overall pore structure was lost after 6 weeks, with some breakage in pore struts observed at week 4. Some strut breakage was observed after 6 and 12 weeks of *in vivo* degradation, but no loss in overall pore structure was seen in 30% DEG foams *in vivo* degradation. The fastest loss in pore structure and earliest occurrence of strut breakage (week 2) was observed in 30% NTA-DEG during *in vitro* degradation in 1% H_2O_2, and complete pore collapse was observed from week 4 onwards. However, during *in vivo* degradation, overall pore structure and interconnectivity were maintained throughout 12 weeks with some strut breakage beginning in week 2 onwards. The maintenance of pore structure and interconnectivity across all formulations

over the entire 12 weeks on implantation show that SMP foams maintain their structural integrity *in vivo* and could therefore serve as a stable scaffold for uniform tissue ingrowth and vascularization in long-term implantation applications.
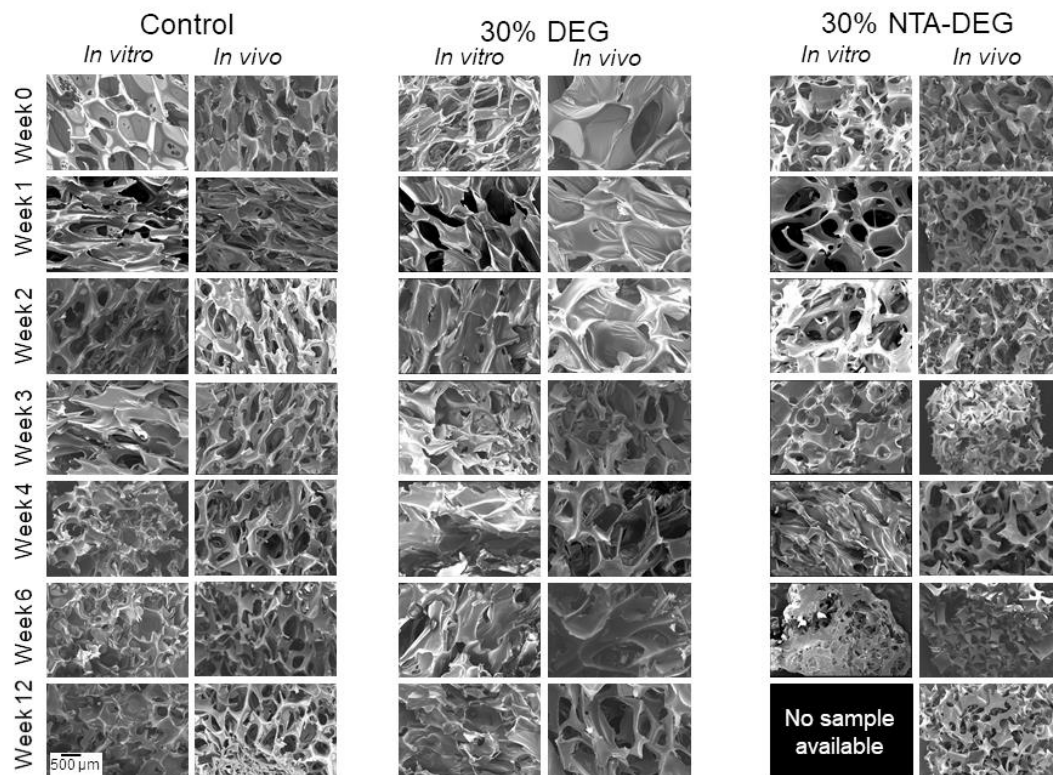
Figure 2.7 Analysis of pore morphology via scanning electron microscopy of samples undergoing *in vitro* degradation (Control in 3% H_2O_2, 30% DEG, and 30% NTA-DEG in 1% H_2O_2) and *in vivo* degradation (subcutaneous implantation in rats). The scale bar of 500 µm applies to all images.

2.3.3.4 Chemical Analysis: Thermal and Spectroscopic Properties

Analysis of T_g throughout the degradation process provides an estimate of the relative crosslink density over time to analyze surface vs. bulk erosion, where surface erosion would result in retention of sample T_g over time, and bulk erosion would cause decreases in T_g throughout degradation. Overall, T_g was maintained throughout the degradation process both *in vitro* and *in*

vivo, as shown in **Figure 2.8**. A significant reduction in T_g was observed for control and 30% DEG foams at 12 weeks of *in vitro* degradation. For 30% NTA-DEG foams, the sacrificial sample was lost by week 12, indicated by a lack of data point here. Maintenance of T_g over the entire 12 weeks can be attributed to high reactivity and low stability of ROS, which limits their diffusion through the sample membranes and restricts degradation to a surface level.
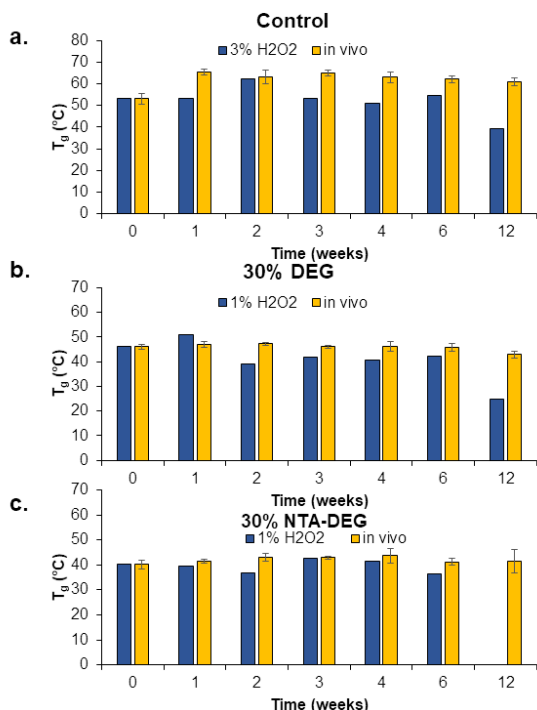
Figure 2.8 Glass transition temperature (T_g) of a) Control, b) 30% DEG, and c) 30% NTA-DEG samples during *in vitro* degradation (blue bars) in 3% H_2O_2 (Control) or 1% H_2O_2 (30% DEG and 30% NTA-DEG) (n=1) and *in vivo* degradation (yellow bars) in subcutaneous pockets in rats (n=3). No statistical differences were observed between *in vitro* and *in vivo* measurements or over time for any formulation (p>0.05 for all).

A shift in the urethane peak from 1680 cm^{-1} to 1688 cm^{-1} and a reduction in the tertiary amine peak at 1050 cm^{-1} was observed across all foams during degradation, **Figure 2.9**. These changes in peaks are attributed to oxidative degradation of tertiary amines present in the monomers

(HPED, TEA, and NTA-DEG) to form primary amines as previously described[26]. A carboxylic acid peak appeared on control foams at 12 weeks of *in vivo* degradation, as seen in **Figure 2.9d**. This change is due to the reduction of tertiary amines in control foams to form primary amines and carboxylic acids[26]. Amongst 30% NTA-DEG foams, a stronger carbonyl peak appears at 1730 cm^{-1} during *in vitro* degradation compared to i*n vivo* degradation as seen in **Figure 2.9c and f**. This change is attributed to the combination of oxidative degradation of tertiary amines and hydrolytic degradation of esters that occurs in these foams in 1% H_2O_2, and the relative changes correlate with observed increased mass loss *in vitro* in these foams.
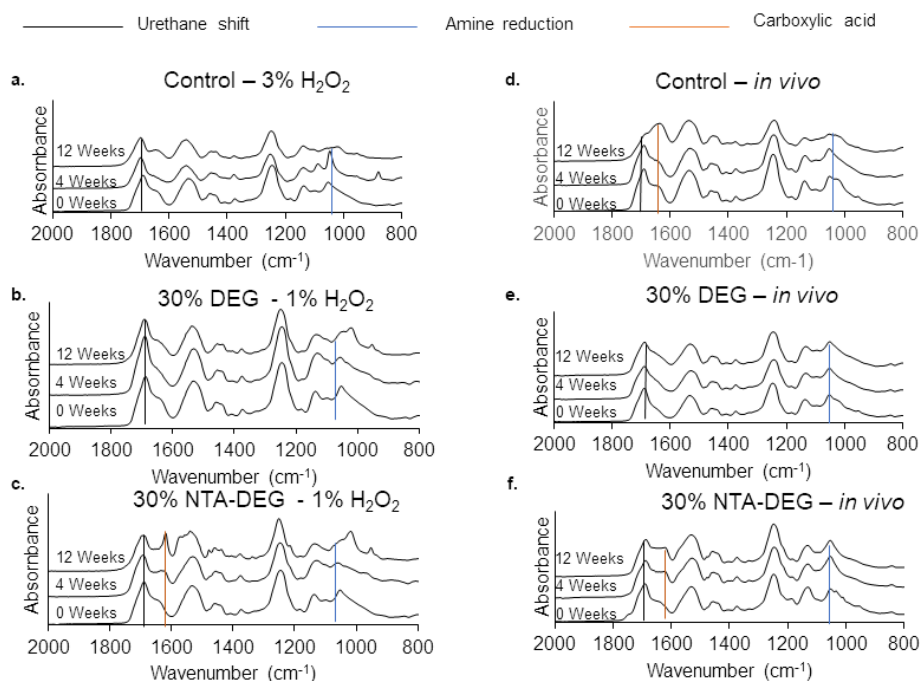
Figure 2.9. Spectroscopic analysis of SMP foams undergoing degradation at 0, 4, and 12 weeks. (a), (b), and (c) represent control, 30% DEG and 30% NTA-DEG undergoing *in vitro* degradation, respectively. (d), (e), and (f) represent control, 30% DEG, and 30% NTA-DEG undergoing *in vivo* degradation, respectively.

2.3.3.5 General considerations for correlating *in vitro* and *in vivo* degradation

As seen here, degradation rates are dependent on surface chemistry, surface area, and porosity, which affect the ability of degradative species to access polymer chains.[76]–[78] It is also important to consider implant location and its impact on degradation. It has been shown that intramuscular degradation rates are higher than subcutaneous degradation rates. This trend has been consistently observed using different polymer compositions and varying animal models.[79]–[81] With the current SMP foam system, it can be observed that degradation is faster after intravenous implantation in comparison with subcutaneous implantation. After 90 days of implantation in an aneurysm model, 40% mass loss of control foams was previously measured, compared with only 30% mass loss at 84 days in the current subcutaneous implant study.[26] Thus, for a given formulation (control foams), degradation may vary based on implant location, and *in vitro* conditions should be altered to account for those potential changes. Specifically, a lower concentration of H_2O_2 is needed *in vitro* to predict slower subcutaneous *in vivo* degradation profiles than would be required to estimate intravenous degradation rates.

Even though the optimized method presented here better mimics the *in vivo* degradation process, the media required to accurately predict *in vivo* degradation is highly complex and depends on the chemical composition of the material under consideration as well. The foams that undergo only oxidative degradation can be more accurately modelled *in vitro* in H_2O_2, allowing for predictions of *in vivo* degradation rates prior to implantation. Ester-containing foams (30% NTA-DEG) undergo degradation via a dual mechanism: hydrolytic degradation of esters and oxidative degradation of ethers and tertiary amines. Furthermore, the breakdown of esters and tertiary amines to form carboxylic acids lowers the pH, which can further catalyze hydrolytic degradation.[74] It is possible that this autocatalysis from ester hydrolysis combined with limited

58

space for acidic byproducts to escape in the vials accelerated *in vitro* degradation in these foams. Additionally, the presence of fibrous tissue likely restricted diffusion of degradative species into foams *in vivo*. While the NTA-DEG foam system is complicated to model *in vitro*, this work provides a significant improvement over previously published work that correlates *in vitro* and *in vivo* degradation profiles of SMP foams. This data presents a framework for assuming that materials that that undergo both hydrolysis and oxidation will degrade more slowly *in vivo*, which could aid in rational selection of formulations for animal testing. Overall, these studies provide a rational framework for the selection of *in vitro* conditions that better mimic implantation conditions to enable a more efficient screening of biomaterials before *in vivo* characterization.

2.3.4 Biological Interactions

2.3.4.1 Cytocompatibility of Foams and Degradation Byproducts

All foams had high cytocompatibility >80% after indirect incubation with 3T3 mouse fibroblasts for 72 hours, as shown in **Figure 2.10a**. Cytocompatibility greater than 75% is considered acceptable for medical devices according to ISO 10993-5 standards[47]. Once initial foam cytocompatibility was confirmed, cells were exposed to fully degraded foam solutions to evaluate safety of degradation byproducts. Degradation byproducts had ~25 to 50% cytocompatibility when tested without any dilution, while the positive control that contained 2% H_2O_2 neutralized by catalase had >75% cytocompatibility. However, a 2X dilution of the byproducts increased viability to ~60-75%, and a 4X dilution further increased cytocompatibility to ~71-100%. All further dilutions had ≥100% viability, as shown in **Figure 2.10b**. The non-diluted solutions represent a case wherein the surrounding cells would be exposed to all the degradation byproducts at once, which is not likely to occur during *in vivo* degradation, as the foams gradually degrade over time and degradation byproducts would likely diffuse away from

the implant site and get eliminated from the body. An increase in cell viability with only a 2-4X

dilution indicates that foam degradation would not cause cytotoxic concerns over the degradation

time frame.
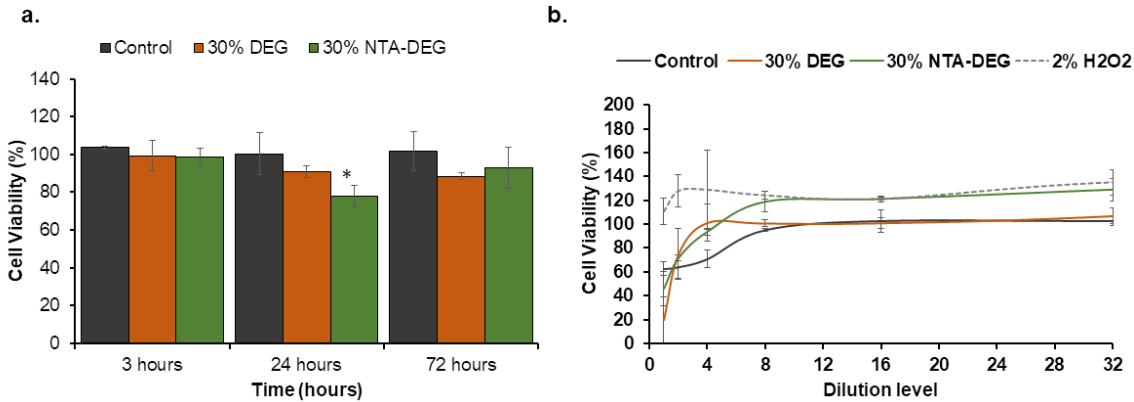
Figure 2.10. Cytocompatibility of foams. (a) Cytocompatibility of 3T3 mouse fibroblasts over 0,

24, and 72 hours (n=3) of indirect contact with foam samples. (b) Dose-response curve of fully

degraded foam solutions and 2% hydrogen peroxide solution control after neutralization with

catalase (n=3). Mean ± standard deviation displayed. *$p<0.05$ relative to positive control.

2.3.4.2 Histological Assessment

Overall, subcutaneous wounds reached a mid-healing stage regardless of foam implant

type, **Figure 2.11**. Central regions of the control foam implants had significant fibrin content and

minimal cellularity at week 1, **Figure 2.11a**. By week 6, high levels of collagen deposition and

cellular infiltration (primarily macrophages) were observed. A healing phase with more prominent

collagen deposition and increased hemosiderin-laden macrophages were seen at 12 weeks. After

implantation of 30% DEG foams (**Figure 2.11b**), abundant fibrin presence and mild cellularity

were observed at week 1, and increased collagen deposition and cellularity (primarily

macrophages) were observed at week 6. A slightly denser extracellular matrix with increased

60

cellularity was seen at week 12. Among the 30% NTA-DEG foams, **Figure 2.11c**, the central regions of the materials had minimum cellularity and abundant fibrin content at week 1. An increase in collagen deposition and inflammatory cells (mostly macrophages) was observed at week 6. At 12 weeks, slightly fewer inflammatory cells were detected in a fibrous background. The type of cells found within each explant tissue across the degradation time is summarized in **Table 2.4**. These results, taken together with the low measured toxicity of degradation byproducts, indicate that SMP foam scaffolds do not induce an undesired immune response during degradation, regardless of chemistry and degradation rate.
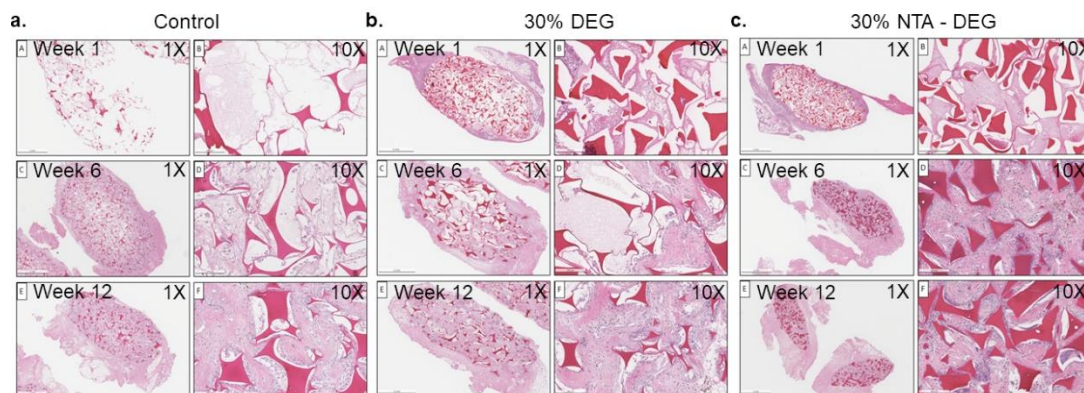
Figure 2.11 Histological assessment of explanted (a) Control, (b) 30% DEG, and (c) 30% NTA-DEG foams at 1, 6, and 12 weeks.

The average *in vivo* subcutaneous implant mass losses per day over the 84 days of implantation were estimated as $0.34 \pm 0.15\%$ for control foams, $0.22 \pm 0.04\%$ for 30% DEG foams, and $0.83 \pm 0.32\%$ for 30% NTA-DEG foams. A reduction in degradation rates was observed from week 6 to week 12, which correlated with the histological observations. Namely, as scar tissue is primarily made up of collagen[70], the gradual observed increase in collagen deposition from low at week 1 to intermediate at week 6 and intermediate-high at week 12 across the foam formulations indicates gradual wound healing and fibrous tissue formation. This formation of scar tissue around

the implanted materials could shield the sample surfaces and limit ROS availability over time to slow down degradation rates. Additionally, the decrease in macrophages over time indicates a lowered immune response that results in reduced ROS concentrations, thereby slowing degradation rates between weeks 6 and 12.

Table 2.4 Cell types within each explant sample throughout 12 weeks of *in vivo* implantation. Scores associated with tissue responses are shown below.

			Control					
			Week 1	Week 2	Week 3	Week 4	Week 6	Week 12
Acute Inflammation		Neutrophils	0.2	0.4	7.9	-	-	-
		Eosinophils	-	-	-	-	-	-
		Macrophages	2.7	9.4	11.1	16	23.2	35
		Erythrophagocytosis	-	-	-	-	-	-
Chronic Inflammation		Hemosiderin-laden macrophages	-	-	-	-	3	9.4
		Plasma cells	-	-	-	-	-	-
		Lymphocytes	-	0.4	0.1	0.4	0.6	1.8
		Giant cells	-	0.2	0.2	1	1.4	0.2
		Collagen (low, intermediate and high density)	Absent	Low	Low	Intermediate	Low-Intermediate	Intermediate
		Debris score (cellular necrosis, fibrin, hemorrhage)	Severe	Severe	Severe	Minimal	Mild	Mild
		Tissue response score (Jessen 2019)	6	5	5	1	2	2
			30% DEG					
			Week 1	Week 2	Week 3	Week 4	Week 6	Week 12
Acute Inflammation		Neutrophils	2.6	0.4	0.2	-	-	-
		Eosinophils	0.6	-	0.3	0.1	0.1	-
		Macrophages	5.1	5.7	23.2	13.5	14.2	18.7
		Erythrophagocytosis	-	0.2	0.2	-	-	-
Chronic Inflammation		Hemosiderin-laden macrophages	-	-	5.9	1.3	3.8	10.1
		Plasma cells	-	-	0.2	-	0.4	-
		Lymphocytes	0.8	0.3	0.2	0.4	0.7	0.6
		Giant cells	-	-	0.9	0.6	1	0.2
		Collagen (low, intermediate and high density)	Low	Low	Intermediate	Intermediate-high	Intermediate	Intermediate-high
		Debris score (cellular necrosis, fibrin, hemorrhage)	Severe	Severe	Minimal	Mild	Moderate	Minimal
		Tissue response score (Jessen 2019)	5	4	2	1	2	2
			30% NTA-DEG					
			Week 1	Week 2	Week 3	Week 4	Week 6	Week 12
Acute Inflammation		Neutrophils	1.9	0.3	0.3	0.3	-	-
		Eosinophils	0.4	0.2	0.2	0.4	1.1	0.1
		Macrophages	1.2	21.6	12.2	28.7	42	25.9
		Erythrophagocytosis	-	-	-	-	-	-
Chronic Inflammation		Hemosiderin-laden macrophages	-	-	7	7	12.6	2.8
		Plasma cells	-	0.1	-	-	-	-
		Lymphocytes	-	0.2	0.2	2.2	1	0.7
		Giant cells	-	0.9	0.4	0.4	0.9	0.8
		Collagen (low, intermediate and high density)	Absent	Low-Intermediate	Low-Intermediate	Intermediate	Intermediate-high	Intermediate
		Debris score (cellular necrosis, fibrin, hemorrhage)	Severe	Minimal	Minimal	Minimal	Minimal	Minimal
		Tissue response score (Jessen 2019)	6	3	2	2	2	2

Tissue response score	
1	Mid-stage healing to healed
2	Mid-stage healing
3	Early to mid-stage healing
4	Early-stage healing
5	Residual blood to early-stage healing
6	Residual blood

2.4 Conclusions

Here, we have shown the ability to tune SMP foam degradation rates *in vivo* by altering monomer chemistry. The dry T_g's above 40°C, high shape fixity, and fast volume recovery allow for stable storage and quick administration of samples at desired implant locations. We identified *in vitro* methods that better mimic *in vivo* degradation rates in comparison with previous studies. As degradation mechanisms get more complex in foams that degrade by both hydrolysis and oxidation, it is more difficult to model *in vivo* degradation using simple *in vitro* media. However, this information can still enable more accurate degradation rate predictions in future studies. Potential approaches to further increase the degradation rates to better match tissue regeneration rates include increasing ester content or adding disulfide linkages. This SMP foam system with tunable degradation rates can be used as a platform to design degradable scaffolds for future tissue regeneration applications.

2.5 References

[1]   G. I. Peterson, A. V. Dobrynin, and M. L. Becker, "Biodegradable Shape Memory Polymers in Medicine," *Adv. Healthc. Mater.*, vol. 6, no. 21, p. 1700694, Nov. 2017.

[2]   I. Dueramae, M. Nishida, T. Nakaji-Hirabayashi, K. Matsumura, and H. Kitano, "Biodegradable shape memory polymers functionalized with anti-biofouling interpenetrating polymer networks," *J. Mater. Chem. B*, vol. 4, no. 32, pp. 5394–5404, 2016.

[3]   Y. S. Joo, J. R. Cha, and M. S. Gong, "Biodegradable shape-memory polymers using polycaprolactone and isosorbide based polyurethane blends," *Mater. Sci. Eng. C*, vol. 91, no. July 2017, pp. 426–435, 2018.

[4]   Y. Guo *et al.*, "A biodegradable functional water-responsive shape memory polymer for biomedical applications," *J. Mater. Chem. B*, vol. 7, no. 1, pp. 123–132, 2019.

[5]   T. Tsujimoto, T. Takayama, and H. Uyama, "Biodegradable shape memory polymeric material from epoxidized soybean oil and polycaprolactone," *Polymers (Basel).*, vol. 7, no. 10, pp. 2165–2174, 2015.

[6]   M. Xie, L. Wang, J. Ge, B. Guo, and P. X. Ma, "Strong Electroactive Biodegradable Shape Memory Polymer Networks Based on Star-Shaped Polylactide and Aniline Trimer for Bone Tissue Engineering," *ACS Appl. Mater. Interfaces*, vol. 7, no. 12, pp. 6772–6781, 2015.

[7]   Z. Deng *et al.*, "Stretchable degradable and electroactive shape memory copolymers with tunable recovery temperature enhance myogenic differentiation," *Acta Biomater.*, vol. 46, pp. 234–244, 2016.

[8]   N. G. Rim *et al.*, "Mussel-inspired surface modification of poly(l-lactide) electrospun fibers for modulation of osteogenic differentiation of human mesenchymal stem cells," *Colloids Surfaces B Biointerfaces*, vol. 91, no. 1, pp. 189–197, Mar. 2012.

[9]   W. L. Webber, F. Lago, C. Thanos, and E. Mathiowitz, "Characterization of soluble, salt-loaded, degradable PLGA films and their release of tetracycline," *J. Biomed. Mater. Res.*, vol. 41, no. 1, pp. 18–29, Jul. 1998.

[10]   L. Lu, C. A. Garcia, and A. G. Mikos, "Retinal pigment epithelium cell culture on thin biodegradable   poly(DL-lactic-co-glycolic   acid)   films," *http://dx.doi.org/10.1163/156856298X00721*, vol. 9, no. 11, pp. 1187–1205, Jan. 2012.

[11]   Y. Feng and J. Guo, "Biodegradable Polydepsipeptides," *Int. J. Mol. Sci.*, vol. 10, no. 2, pp. 589–615, Feb. 2009.

[12]   D. A. Barrera, E. Zylstra, P. T. Lansbury, and R. Langer, "Synthesis and RGD Peptide Modification of a New Biodegradable Copolymer: Poly(lactic acid-co-lysine)," *J. Am. Chem. Soc.*, vol. 115, no. 23, pp. 11010–11011, Nov. 1993.

[13]   L. B. Jiang, D. H. Su, P. Liu, Y. Q. Ma, Z. Z. Shao, and J. Dong, "Shape-memory collagen scaffold for enhanced cartilage regeneration: native collagen versus denatured collagen," *Osteoarthr. Cartil.*, vol. 26, no. 10, pp. 1389–1399, Oct. 2018.

[14]   J. R. Vlcek, M. M. Reynolds, and M. J. Kipper, "Enzymatic Degradation of Glycosaminoglycans and Proteoglycan-Mimetic Materials in Solution and on Polyelectrolyte Multilayer Surfaces," *Biomacromolecules*, vol. 22, no. 9, pp. 3913–3925, Aug. 2021.

[15]   A. Sannino, S. Pappadà, M. Madaghiele, A. Maffezzoli, L. Ambrosio, and L. Nicolais, "Crosslinking of cellulose derivatives and hyaluronic acid with water-soluble carbodiimide," *Polymer (Guildf).*, vol. 46, no. 25, pp. 11206–11212, Nov. 2005.

[16]   A. Marshall, C. Irvin, T. Barker, K. Sage, E. Hauch, and B. Ratner, "Biomaterials with tightly controlled pore size that promote vascular in-growth," 2004.

[17]   S. J. Hollister, "Porous scaffold design for tissue engineering," 2005.

[18]   K. G. Swan and R. C. Swan, "Principles of ballistics applicable to the treatment of gunshot wounds," *Surg. Clin. North Am.*, vol. 71, no. 2, pp. 221–239, 1991.

[19]   C. M. Yakacki, R. Shandas, C. Lanning, B. Rech, A. Eckstein, and K. Gall, "Unconstrained recovery characterization of shape-memory polymer networks for cardiovascular applications," *Biomaterials*, vol. 28, no. 14, pp. 2255–2263, May 2007.

[20]   A. J. Boyle *et al.*, "In vitro and in vivo evaluation of a shape memory polymer foam-over-wire embolization device delivered in saccular aneurysm models," *Journal of Biomedical Materials Research - Part B Applied Biomaterials*, vol. 104, no. 7. pp. 1407–1415, 2016.

[21]   H. T. Beaman *et al.*, "Hemostatic Shape Memory Polymer Foams with Improved Survival in a Lethal Traumatic Hemorrhage Model," *Acta Biomater.*, vol. 137, pp. 112–123, 2022.

[22]   R. Xie *et al.*, "Self-fitting shape memory polymer foam inducing bone regeneration: A rabbit femoral defect study," *Biochim. Biophys. Acta - Gen. Subj.*, vol. 1862, no. 4, pp. 936–945, Apr. 2018.

[23]   H. Xie, X.-Y. Deng, C.-Y. Cheng, K.-K. Yang, and Y.-Z. Wang, "New Strategy to Access

Dual-Stimuli-Responsive Triple-Shape-Memory Effect in a Non-overlapping Pattern," *Macromol. Rapid Commun.*, vol. 38, no. 4, p. 1600664, Feb. 2017.

[24]   J. N. Rodriquez *et al.*, "In vivo tissue responses following implantation of shape memory polyurethane foam in a porcine aneurysm model," *J BiomediMater Res A*, vol. 102, no. 5, pp. 1231–1242, 2014.

[25]   S. L. Jessen *et al.*, "Micro-CT and histopathology methods to assess host response of aneurysms treated with shape memory polymer foam-coated coils versus bare metal coil occlusion devices," *J. Biomed. Mater. Res. Part B Appl. Biomater.*, vol. 108, no. 5, pp. 2238–2249, Jul. 2020.

[26]   A. C. Weems, K. T. Wacker, J. K. Carrow, A. J. Boyle, and D. J. Maitland, "Shape memory polyurethanes with oxidation-induced degradation: In vivo and in vitro correlations for endovascular material applications," *Acta Biomater.*, vol. 59, pp. 33–44, Sep. 2017.

[27]   P. Singhal, W. Small, E. Cosgriff-Hernandez, D. J. Maitland, and T. S. Wilson, "Low density biodegradable shape memory polyurethane foams for embolic biomedical applications," *Acta Biomater.*, vol. 10, no. 1, pp. 67–76, Jan. 2014.

[28]   A. C. Weems, A. Easley, S. R. Roach, and D. J. Maitland, "Highly Cross-Linked Shape Memory Polymers with Tunable Oxidative and Hydrolytic Degradation Rates and Selected Products Based on Succinic Acid," *ACS Appl. bio Mater.*, vol. 2, no. 1, pp. 454–463, Jan. 2019.

[29]   L. K. Jang, G. K. Fletcher, M. B. B. Monroe, and D. J. Maitland, "Biodegradable shape memory polymer foams with appropriate thermal properties for hemostatic applications," *J. Biomed. Mater. Res. Part A*, no. May 2019, pp. 1281–1294, 2020.

[30] A. U. Vakil *et al.*, "Shape Memory Polymer Foams with Tunable Degradation Profiles," *ACS Appl. bio Mater.*, vol. 4, no. 9, pp. 6769–6779, Aug. 2021.

[31] A. C. Weems, J. K. Carrow, A. K. Gaharwar, and D. J. Maitland, "Improving the Oxidative Stability of Shape Memory Polyurethanes Containing Tertiary Amines by the Presence of Isocyanurate Triols," *Macromolecules*, vol. 51, no. 22, pp. 9078–9087, 2018.

[32] S. M. Hasan, G. K. Fletcher, M. B. B. Monroe, M. A. Wierzbicki, L. D. Nash, and D. J. Maitland, "Shape Memory Polymer Foams Synthesized Using Glycerol and Hexanetriol for Enhanced Degradation Resistance," *Polymers (Basel).*, vol. 12, no. 10, p. 2290, Oct. 2020.

[33] A. C. Weems, K. T. Wacker, and D. J. Maitland, "Improved oxidative biostability of porous shape memory polymers by substituting triethanolamine for glycerol," *J. Appl. Polym. Sci.*, vol. 136, no. 35, p. 47857, Sep. 2019.

[34] A. U. Vakil, N. M. Petryk, E. Shepherd, and M. B. B. Monroe, "Biostable Shape Memory Polymer Foams for Smart Biomaterial Applications," *Polymers (Basel).*, vol. 13, no. 23, p. 4084, Nov. 2021.

[35] J. N. Rodriguez *et al.*, "Opacification of shape memory polymer foam designed for treatment of intracranial aneurysms," *Ann. Biomed. Eng.*, vol. 40, no. 4, pp. 883–897, Apr. 2012.

[36] J. Horn *et al.*, "Comparison of shape memory polymer foam versus bare metal coil treatments in an in vivo porcine sidewall aneurysm model," *J. Biomed. Mater. Res. Part B Appl. Biomater.*, vol. 105, no. 7, pp. 1892–1905, Oct. 2017.

[37] I. Standard, M. Vibration, I. Standard, S. E. Cie, and I. Standard, "ISO 10993-13

Identification and quantification of degradation products from polymeric medical devices," vol. 2004, 2004.

[38]   S. L. Jessen *et al.*, "Microscopic Assessment of Healing and Effectiveness of a Foam-Based Peripheral Occlusion Device," *ACS Biomater. Sci. Eng.*, vol. 6, no. 5, pp. 2588–2599, 2020.

[39]   Q. Yang *et al.*, "A cartilage ECM-derived 3-D porous acellular matrix scaffold for in vivo cartilage tissue engineering with PKH26-labeled chondrogenic bone marrow-derived mesenchymal stem cells," *Biomaterials*, vol. 29, no. 15, pp. 2378–2387, May 2008.

[40]   F. Wang, Y. Hu, D. He, G. Zhou, X. Yang, and E. Ellis, "Regeneration of subcutaneous tissue-engineered mandibular condyle in nude mice," *J. Cranio-Maxillofacial Surg.*, vol. 45, no. 6, pp. 855–861, Jun. 2017.

[41]   D. J. Modulevsky, C. M. Cuerrier, and A. E. Pelling, "Biocompatibility of Subcutaneously Implanted Plant-Derived Cellulose Biomaterials," *PLoS One*, vol. 11, no. 6, p. e0157894, Jun. 2016.

[42]   U. Klinge, K. Junge, B. Spellerberg, C. Piroth, B. Klosterhalfen, and V. Schumpelick, "Do multifilament alloplastic meshes increase the infection rate? Analysis of the polymeric surface, the bacteria adherence, and the in vivo consequences in a rat model," *J. Biomed. Mater. Res.*, vol. 63, no. 6, pp. 765–771, Jan. 2002.

[43]   M. W. Laschke, J. M. Häufel, H. Thorlacius, and M. D. Menger, "New experimental approach to study host tissue response to surgical mesh materials in vivo," *J. Biomed. Mater. Res. Part A*, vol. 74A, no. 4, pp. 696–704, Sep. 2005.

[44]   W. M. L. Neethling, R. Glancy, and A. J. Hodge, "Mitigation of calcification and cytotoxicity of a glutaraldehyde-preserved bovine pericardial matrix: improved biocompatibility after extended implantation in the subcutaneous rat model.," *J. Heart Valve Dis.*, vol. 19, no. 6, pp. 778–785, Nov. 2010.

[45]   A. Padsalgikar *et al.*, "Limitations of predicting in vivo biostability of multiphase polyurethane elastomers using temperature-accelerated degradation testing," *J. Biomed. Mater. Res. - Part B Appl. Biomater.*, vol. 103, no. 1, pp. 159–168, 2015.

[46]   S. M. Herting *et al.*, "In vitro cytocompatibility testing of oxidative degradation products," *J. Bioact. Compat. Polym.*, p. 088391152110031, Mar. 2021.

[47]   A. U. Vakil, N. M. Petryk, E. Shepherd, and M. B. B. Monroe, "Biostable Shape Memory Polymer Foams for Smart Biomaterial Applications," *Polymers (Basel).*, vol. 13, no. 23, p. 4084, Nov. 2021.

[48]   P. ISO, "ISO 10993-5:2009 Biological evaluation of medical devices -- Part 5: Tests for in vitro cytotoxicity," *International Organization for Standardization, Geneva*. p. 34, 2009.

[49]   A. U. Vakil *et al.*, "Shape Memory Polymer Foams with Tunable Degradation Profiles," *ACS Appl. Bio Mater.*, vol. 4, no. 9, pp. 6769–6779, Sep. 2021.

[50]   A. C. Weems, K. T. Wacker, J. K. Carrow, A. J. Boyle, and D. J. Maitland, "Shape memory polyurethanes with oxidation-induced degradation: In vivo and in vitro correlations for endovascular material applications," *Acta Biomater.*, vol. 59, pp. 33–44, Sep. 2017.

[51]   M. B. Browning, S. N. Cereceres, P. T. Luong, and E. M. Cosgriff-Hernandez,

"Determination of the in vivo degradation mechanism of PEGDA hydrogels," *J. Biomed. Mater. Res. Part A*, vol. 2014, no. January, p. n/a-n/a, Feb. 2014.

[52]   Z. Wang, S. Wang, Y. Marois, R. Guidoin, and Z. Zhang, "Evaluation of biodegradable synthetic scaffold coated on arterial prostheses implanted in rat subcutaneous tissue," *Biomaterials*, vol. 26, no. 35, pp. 7387–7401, 2005.

[53]   K. Jansen, J. F. A. Van Der Werff, P. B. Van Wachem, J. P. A. Nicolai, L. F. M. H. De Leij, and M. J. A. Van Luyn, "A hyaluronan-based nerve guide: In vitro cytotoxicity, subcutaneous tissue reactions, and degradation in the rat," *Biomaterials*, vol. 25, no. 3, pp. 483–489, 2004.

[54]   A. K. Azab *et al.*, "Biocompatibility evaluation of crosslinked chitosan hydrogels after subcutaneous and intraperitoneal implantation in the rat," *J. Biomed. Mater. Res. Part A*, vol. 83A, no. 2, pp. 414–422, Nov. 2007.

[55]   E. M. Christenson, M. Dadsetan, M. Wiggins, J. M. Anderson, and A. Hiltner, "Poly(carbonate urethane) and poly(ether urethane) biodegradation: In vivo studies," *J. Biomed. Mater. Res. - Part A*, vol. 69, no. 3, pp. 407–416, 2004.

[56]   J. Kim, M. Dadsetan, S. Ameenuddin, A. J. Windebank, M. J. Yaszemski, and L. Lu, "In vivo biodegradation and biocompatibility of PEG/sebacic acid-based hydrogels using a cage implant system," *J. Biomed. Mater. Res. - Part A*, vol. 95, no. 1, pp. 191–197, 2010.

[57]   Z. Zhang, R. Guidoin, M. W. King, T. V. How, Y. Marois, and G. Laroche, "Removing fresh tissue from explanted polyurethane prostheses: which approach facilitates physico-chemical analysis?," *Biomaterials*, vol. 16, no. 5, pp. 369–380, 1995.

[58]   S. L. Jessen *et al.*, "Micro-CT and histopathology methods to assess host response of aneurysms treated with shape memory polymer foam-coated coils versus bare metal coil occlusion devices," *J. Biomed. Mater. Res. Part B Appl. Biomater.*, vol. 108, no. 5, pp. 2238–2249, Jul. 2020.

[59]   C. M. Walthers, A. K. Nazemi, S. L. Patel, B. M. Wu, and J. C. Y. Dunn, "The effect of scaffold macroporosity on angiogenesis and cell survival in tissue-engineered smooth muscle," *Biomaterials*, vol. 35, no. 19, pp. 5129–5137, 2014.

[60]   X. Xiao *et al.*, "The promotion of angiogenesis induced by three-dimensional porous beta-tricalcium phosphate scaffold with different interconnection sizes via activation of PI3K/Akt pathways," *Sci. Rep.*, vol. 5, no. 1, p. 9409, Aug. 2015.

[61]   P. Singhal *et al.*, "Ultra low density and highly crosslinked biocompatible shape memory polyurethane foams," *J. Polym. Sci. Part B Polym. Phys.*, vol. 50, no. 10, pp. 724–737, May 2012.

[62]   T. L. Landsman *et al.*, "Design and verification of a shape memory polymer peripheral occlusion device," *J. Mech. Behav. Biomed. Mater.*, vol. 63, pp. 195–206, Oct. 2016.

[63]   A. J. Boyle *et al.*, "In vitro and in vivo evaluation of a shape memory polymer foam-over-wire embolization device delivered in saccular aneurysm models," *J. Biomed. Mater. Res. Part B Appl. Biomater.*, vol. 104, no. 7, pp. 1407–1415, Oct. 2016.

[64]   M. F. Griffin, B. C. Leung, Y. Premakumar, M. Szarko, and P. E. Butler, "Comparison of the mechanical properties of different skin sites for auricular and nasal reconstruction," *J. Otolaryngol. - Head Neck Surg.*, vol. 46, no. 1, pp. 1–6, 2017.

[65]   A. Karimi, S. M. Rahmati, and M. Navidbakhsh, "Mechanical characterization of the rat

and mice skin tissues using histostructural and uniaxial data," *Bioengineered*, vol. 6, no. 3, pp. 153–160, May 2015.

[66]   D. Demetriades, "Ballistics of Gunshot Injuries," *Trauma Manag.*, pp. 546–557, 2020.

[67]   P. K. Stefanopoulos, G. F. Hadjigeorgiou, K. Filippakis, and D. Gyftokostas, "Gunshot wounds: A review of ballistics related to penetrating trauma," *J. Acute Dis.*, vol. 3, no. 3, pp. 178–185, Jan. 2014.

[68]   A. C. Weems, W. Li, D. J. Maitland, and L. M. Calle, "Polyurethane Microparticles for Stimuli Response and Reduced Oxidative Degradation in Highly Porous Shape Memory Polymers," *ACS Appl. Mater. Interfaces*, vol. 10, no. 39, pp. 32998–33009, Oct. 2018.

[69]   L. K. Jang, G. K. Fletcher, M. B. B. Monroe, and D. J. Maitland, "Biodegradable shape memory polymer foams with appropriate thermal properties for hemostatic applications," *J. Biomed. Mater. Res. - Part A*, vol. 108, no. 6, pp. 1281–1294, 2020.

[70]   D. K. Dempsey *et al.*, "Comparative analysis of in vitro oxidative degradation of poly(carbonate urethanes) for biostability screening," *J. Biomed. Mater. Res. - Part A*, vol. 102, no. 10, pp. 3649–3665, 2014.

[71]   "ISO 10993-13:2010 - Biological evaluation of medical devices - Part 13: Identification and quantification of degradation products from polymeric medical devices." [Online]. Available: https://webstore.ansi.org/standards/iso/iso10993132010?gclid=Cj0KCQiArt6PBhCoARIsAMF5 wagszhYtuzxVwE8jKg6wiSIlrgdvwj5DPhBODDPHDDRwNoHGAjktIw0aAq4JEALw_wcB. [Accessed: 31-Jan-2022].

[72]   C. Dunnill *et al.*, "Reactive oxygen species (ROS) and wound healing: the functional role of ROS and emerging ROS-modulating technologies for augmentation of the healing process," *Int. Wound J.*, vol. 14, no. 1, pp. 89–96, Feb. 2017.

[73]   E. M. Christenson, J. M. Anderson, and A. Hiltner, "Oxidative mechanisms of poly(carbonate urethane) and poly(ether urethane) biodegradation: In vivo and in vitro correlations," *J. Biomed. Mater. Res. - Part A*, vol. 70, no. 2, pp. 245–255, 2004.

[74]   H. A. Smith and J. H. Steele, "The Acid Catalyzed Hydrolysis of Ethyl Esters of Aliphatic Acids," *J. Am. Chem. Soc.*, vol. 63, no. 12, pp. 3466–3469, Dec. 1941.

[75]   J. W. Madden and E. E. Peacock, "Studies on the Biology of Collagen During Wound Healing," *Ann. Surg.*, vol. 174, no. 3, pp. 511–520, Sep. 1971.

[76]   S. C. Ghosh, J. S. Y. Ngiam, A. M. Seayad, D. T. Tuan, C. L. L. Chai, and A. Chen, "Copper-catalyzed oxidative amidation of aldehydes with amine salts: Synthesis of primary, secondary, and tertiary amides," *J. Org. Chem.*, vol. 77, no. 18, pp. 8007–8015, 2012.

[77]   K. Bergstad and J. E. Bäckvall, "Mild and Efficient Flavin-Catalyzed H2O2 Oxidation of Tertiar Amines to Amine N-Oxides," *J. Org. Chem.*, vol. 63, no. 19, pp. 6650–6655, 1998.

[78]   J. R. Martin *et al.*, "A porous tissue engineering scaffold selectively degraded by cell-generated reactive oxygen species," *Biomaterials*, vol. 35, no. 12, pp. 3766–3776, 2014.

[79]   N. Olmo, J. Turnay, J. G. Gavilanes, M. A. Lizarbe, and J. I. Herrera, "Subcutaneous and intramuscular implantation of sepiolite-collagen complexes," *J. Mater. Sci. Mater. Med.*, vol. 3, no. 4, pp. 239–244, Jul. 1992.

[80]   G. BEUMER, C. VANBLITTERSWIJK, and M. PONEC, "Degradative behaviour of polymeric matrices in (sub)dermal and muscle tissue of the rat: a quantitative study," *Biomaterials*, vol. 15, no. 7, pp. 551–559, Jun. 1994.

[81]   F. Sabri *et al.*, "Histological Evaluation of the Biocompatibility of Polyurea Crosslinked Silica Aerogel Implants in a Rat Model: A Pilot Study," *PLoS One*, vol. 7, no. 12, p. e50686, Dec. 2012.

Chapter III

Magnetically Actuated Shape Memory Polymers for

On-Demand Drug Delivery

3.1   Introduction

Drug delivery systems can include a combination of drug carriers, manufacturing techniques, and routes to delivering a therapeutic drug to its target site to achieve the required therapeutic effect. Depending on the release mechanism, drug delivery can be categorized as targeted delivery or controlled release. Targeted delivery involves drug release at the target site without affecting any surrounding tissues.[1][2] Controlled release of drugs at a specific interval and rate is employed to achieve a sustained drug release.[3] An ideal drug delivery system ensures that the drug is available for the desired duration, above the minimal effective concentration and below the maximum tolerable concentration, while not displaying any adverse physiological effects on surrounding tissues.[4]

Over 90% of hospitalized patients undergo some form of infusion therapy in which drugs are delivered intravenously.[5] While this method allows access to the entire body via the bloodstream and enables administration of large volumes of drug infusions, there are several limitations associated with intravenous infusions, including uneven drug distribution and the inability to reach the target site at the desired dosage.[6] Intravenous administration could result in drugs reaching non-targeted tissues/organs and having adverse effects on healthy tissues. Repeated intravenous administration can cause pain at the site of injection and increases the patient's risk of bacterial infection, requiring strict aseptic conditions at all times.[7]

An alternative for controlled drug delivery includes transdermal patches.[8] This system involves the transport of drugs across the skin from either a reservoir or matrix loaded with drugs. A major limitation of transdermal patches is that very few drug products have been developed that successfully transport across the skin due to the barrier provided by the stratum corneum of the epidermis layer of skin.[9] This approach, therefore, requires that the drug molecule be small enough to penetrate the skin. One method to overcome these limitations involves the use of microneedle patches that penetrate the skin to allow a larger range of drugs to be administered.[10] However, microneedle patches have lower dosage accuracy compared to hypodermic needles.[11]

Another approach to overcome these limitations involves the use of on-demand pulsatile drug delivery. Pulsatile drug delivery is the rapid release of a drug within a short period followed by a specified lag time with little or no drug being released.[12] This technique requires the use of an external trigger to initiate drug release from a drug-loaded polymer composite at the desired location and provides control over drug delivery timing, location, and concentration. Multiple on-demand drug delivery systems have been developed that utilize an external stimulus to trigger drug release. Chunder et al. developed a pH-responsive scaffold by electrospinning poly(acrylic acid) and poly(allylamine hydrochloride).[13] Methylene blue was used as a model cationic drug that was released at low pH. This system requires that drugs be cationic or anionic and requires control over pH, which limits its applicability.

Light-triggered on-demand drug release from an implanted depot was developed by Carling et al.[14] This approach utilizes a biphenyl derivative that is photocleaved by blue light irradiation to release a hydrophobic cargo, dexamethasone. While this system shows promise in subcutaneous implants, light-triggered systems could have limited applicability in deep implantation sites. To that end, Satarkar et al. developed magnetic hydrogel nanocomposites that

can be actuated remotely to trigger on-demand drug release.[15] In that work, N-isopropyl acrylamide hydrogels were loaded with magnetic nanoparticles and were exposed to high-frequency alternating magnetic fields to enable the release of vitamin B12 over time. An increase in drug release was observed upon application of the alternating magnetic field, and drug release was controlled upon exposure to the alternating magnetic field every hour over 12 hours, with 10 minutes of magnetic actuation at each time point.

The magnetically-responsive approach is promising, but more robust control over drug delivery could be attained by using shape memory polymers (SMPs) whose shape change can be triggered remotely. SMPs are smart materials that are prepared in an original shape and can be temporarily deformed and stored in a secondary shape after exposure to an external stimulus. The original shape can be recovered upon exposure to a second external stimulus. Shape recovery of SMPs can be actuated by a range of triggers including temperature, pH, and electrical or magnetic impulse.[16] Polydiocitrate-based shape memory elastomers with drug releasing capabilities were developed by Serrano et al.[17] Hydrophobic microdomains within the polymer were used as reservoirs to entrap and subsequently release hydrophobic drugs. Exposing the polymers to PBS at varying temperatures (above and below their transition temperature) altered the drug release from the polymer composite, thus providing a thermally induced drug release over 700 hours. However, thermal actuation of SMPs is limited to temperatures below ~45°C in the body to minimize potential thermal damage to cells.

We hypothesized that the benefits of prior magnetically-responsive and SMP approaches could be combined in a single system with unique, user-defined control over release. To that end, we developed magnetically-responsive polyurethane-based SMPs with temporally controlled drug delivery. Polymer compositions were chosen based on previously developed biostable SMPs, and

79

magnetically-responsive polymer composites were prepared by incorporating iron oxide magnetic nanoparticles (mnps).[18], [19] These materials were initially prepared with constant drug loading across the polymer and thermally fixed in a strained temporary shape that limits drug diffusion. Doxorubicin hydrochloride (a relatively hydrophilic chemotherapeutic with a molar mass of 543.5 $g \cdot mol^{-1}$) and 6-mercaptopurine (a relatively hydrophobic immunosuppressant with a molar mass of 152.2 $g \cdot mol^{-1}$) were selected for these studies, since these drugs may have reduced side effects on patients if localized and controlled release can be obtained. Rhodamine (a hydrophilic fluorescent molecule with molar mass of 479.02 $g \cdot mol^{-1}$) was employed as an additional model drug due to its ease of measurement. Drug release was initiated upon mnp excitation via exposure to an alternating magnetic field. Variation in shape recovery rates and subsequent drug release was controlled by altering the polymer chemistry and mnp concentration. Control over drug release within a single implant was achieved by varying the mnp concentration, thus allowing controlled drug release from specified regions of the polymer over multiple triggers. These polymer composites could provide a new option to deliver a single drug at multiple time points or to achieve dual drug release from the same implant at a specified implant location with reduced potential risks to surrounding tissues/organs.

3.2   Materials and Methods

3.2.1 Materials All materials were purchased from Fisher Scientific (Waltham, MA, USA) as reagent grade. Hexamethylene diisocyanate (HDI), sodium borohydride, ferric chloride hexahydrate, phosphate-buffered saline (PBS), dimethyl sulfoxide (DMSO), doxorubicin hydrochloride (Dox), 6-mercaptopurine (6-MP), rhodamine B (Rhod), dibutyl(tin)dilaurate (DBTDL), Sylgard-184 poly(dimethyl siloxane) (PDMS), hydrogen peroxide (H_2O_2, 30%) and methanol were used as purchased. Triethylene glycol (TEG), polypropylene glycol (MW: 2000 Da, (PPG)), and N', N', N, N-tetrakis-2-hydroxypropyl ethylenediamine (HPED) were dried in a vacuum oven at -30 inches Hg vacuum and 40°C overnight before use.

3.2.2   Synthesis.

a. Magnetic particles. In a 250 ml beaker, a ferric chloride ($FeCl_3.6H_2O$) solution (0.1 M in deionized water) was added dropwise to sodium borohydride ($NaBH_4$, 2.5 M in deionized water) at a ratio of 4:1 ($FeCl_3:NaBH_4$). The solutions were mixed constantly using a magnetic stir plate (Fisher Scientific, Waltham, MA, USA) at 1050 rpm. The reaction produces bubbles and was allowed to continue until no more bubble formation was observed (~1 hour). Magnetic particles were allowed to settle at the bottom of the beaker and then washed twice using deionized water and twice using methanol. Particles were centrifuged (Sorvall X4F Pro MD, Thermo Scientific, Waltham, MA, USA) at 10,000Xg for 10 minutes at room temperature during each washing step. Washed particles were dried at 50°C overnight, and any clusters were crushed using a glass rod. Particle size was determined via dynamic light scattering using a Zetasizer Ultra (Malvern

Panalytical, Westborough, MA, USA). Approximately 1 mg of particles were added to 5 ml DI water in a disposable 10x10 polystyrene cell and sonicated for five minutes before testing. A graph of intensity (%) vs. particle size (d, nm) was analyzed to confirm the particle size.

b. Polymers. All synthesis was performed in a glove box (Labconco, Kansas City, MO, USA) while maintaining a dry inert atmosphere using nitrogen passed through a drying train (Labconco, Kansas City, MO, USA) to maintain relative humidity below 200 ppm. The composition of each formulation is shown in Table 3.1, and component structures are shown in Figure 1a. All compositions included HDI as the isocyanate component, and a combination of PPG, TEG, and/or HPED was employed as the hydroxyl component to form polyurethanes. First, the drug/dye (Dox, 6-MP, Rhod) and mnps were weighed out into a speed mixer cup, shown in Table 3.1. In short, 5 mg of drug/dye was added to each test sample (10 g), and either 50 mg or 100 mg of mnps was added to each sample (10 g). Then, the monomers and catalyst (DBTDL) were added and mixed in a speed mixer (FlackTek, Landrum, SC, USA) at 3500 rpm. The duration of mixing varied depending on the reactivity of each component, as shown in Table 3.1. The monomers were then allowed to react in an oven in the speed mixer cup at 50 °C for 48 h.

Formulations with dual compositions were prepared in a two-step process. The components for PPG TEG were mixed in a speed mixer and then poured immediately onto a petri dish lined with a Teflon liner. One-half of the petri dish was blocked using a PDMS mold to prevent

the reaction components from spreading across the entire petri dish. The petri dish was immediately placed in an airtight container in an oven at 50 °C for 48 h. The PDMS mold was then peeled off, and the HPED TEG mixture was mixed and poured onto the remaining half of the petri dish while leaving the PPG TEG side intact. This mixture was then allowed to react for another 48 h at 50 °C to form a dual SMP with PPG TEG on one side and HPED TEG on the other side.

Table 3.1 Components of synthesized polymer film compositions in wt% with catalyst amount and mixing times. HDI: hexamethylene diisocyanate, PPG: poly(propylene glycol), TEG: triethylene glycol, HPED: hydroxypropyl ethylenediamine, DBTL: dibutyl(tin) dilaurate, Dox: doxorubicin, 6-MP: 6-mercaptopurine, Rhod: rhodamine B.

Sample Name	HDI	PPG	TEG	HPED	DBTDL	Fe_3O_4 particles	Drug (5 mg/10 g)	Mixing time (sec)
PPG TEG	29.4	50.8	19.8	0	0.8	50 mg	Dox 6-MP Rhod	15
						100 mg	Dox 6-MP Rhod	
HPED PPG	29.6	51.0	0	19.4	0.8	50 mg	Dox 6-MP Rhod	30
						100 mg		
HPED TEG	55.8	0	22.4	21.8	0	50 mg	Dox 6-MP Rhod	60
						100 mg		
Dual- R	29.4	50.8	19.8	0	0.8	100 mg	Rhod	15
Dual- L	55.8	0	22.4	21.8	0	50 mg	6-MP	60
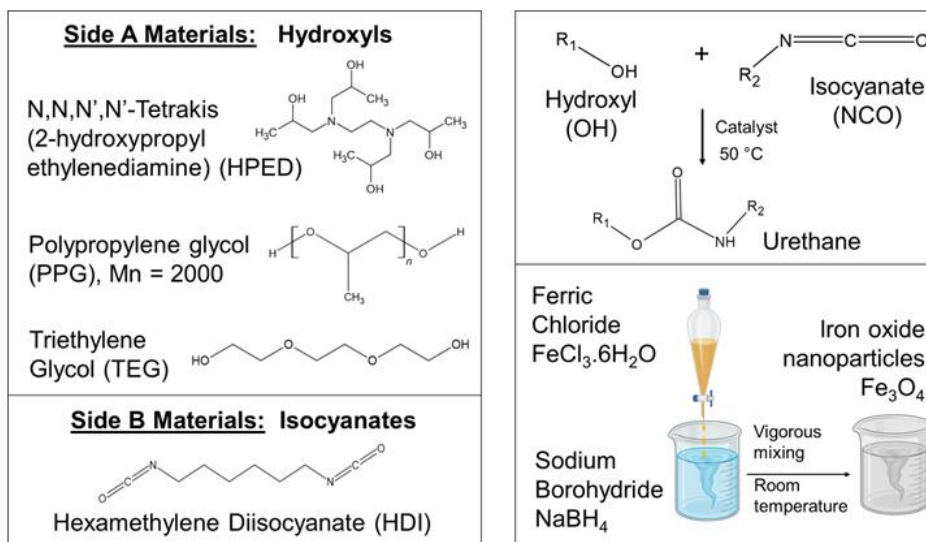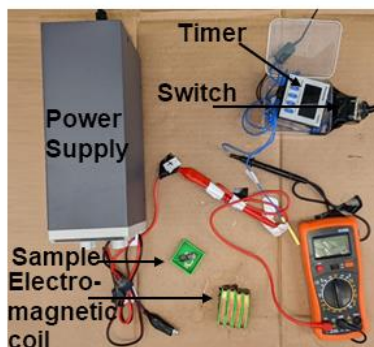
Figure 3.1 (a) Polymer component structures and overview of the synthesis of polyurethane SMP. (**b**) Overview of the synthesis of magnetic nanoparticles. (**c**) Magnetic circuit setup employed for magnetic actuation of SMPs.

3.2.3 Hydrophobicity. Thin slices (2 mm thick, 1.5 cm wide, and 6.5 cm long) were cut from each formulation to measure the contact angle using a goniometer (Model 500, Ramé-hart Co, Succasunna, NJ). Water droplets (0.2 ml, n=3) were placed onto the films and 100 images were captured at a 0.01-second interval using a SuperSpeed U4 series camera. Each image was analyzed using DROPImage software to determine the angle between the water droplet and the material surface.

An average of 100 measurements was used to determine the contact angle for each water droplet.

3.2.4 Mechanical Properties. Tensile testing was performed using a 24 N load cell (Test Resources, Shakopee, MN, USA). Samples (n=3) were cut in a dogbone shape (ASTM D638 Type IV scaled down by a factor of 4) with a gauge length of 6.25 mm and width of 1.5 mm. The thickness of each sample was measured using calipers. Samples were subjected to a tensile force at a rate of 2 mm/min until failure to measure elastic modulus, ultimate tensile strength, and elongation at break. The measurements were carried out on dry and wet samples. To prepare wet samples, specimens were placed in water at 50°C for 4 hours before testing.

3.2.5 Thermal Characterization. A differential scanning calorimeter (DSC Q200, TA Instruments, New Castle, DE, USA) was used to measure the glass transition and melting temperatures of polymers. Dry samples (n=3) were weighed (~3-5 mg) and placed in T_{zero} aluminum pans to be tested. Samples were cooled to -40°C at 10°C/min, kept isothermally for 2 minutes, heated to 120°C at 10°C/min, kept isothermally for 2 minutes, cooled to 50°C at 2°C/min, kept isothermally for 20 minutes, cooled to -40°C at 2°C/min, kept isothermally for 2 minutes, and then heated back to 120°C at 10°C/min. Transition temperatures were measured during the second heating cycle. To test samples in wet conditions, thin slices (n=3) were placed in DI water at 50°C for 4 hours, patted dry, cut to weigh ~ 3 to 5 mg, and placed in T_{zero} aluminum pans with hermetic lids. To measure the transition temperatures, samples were cooled to -40°C at 10°C/min and heated to 120°C at 10°C/min. The transition temperatures were measured in a single heating cycle.

3.2.6   Shape Memory Properties. Samples (n=3) were cut into dogbone shapes (ASTM D638 Type IV scaled down by a factor of 4) with a gauge length of 6.25 mm and width of 1.5 mm. The width of each sample was measured using calipers before testing. Shape memory tests were performed using a dynamic mechanical analyzer (DMA, Q800, TA Instruments, New Castle, DE, USA). The samples were heated to 80°C at 2°C/min and held isothermally for 2 minutes. Then a controlled force was applied at 0.03 N/min to a maximum limit of 18 N until the sample reached 20% strain. Samples were then cooled to -5°C and held isothermally for 2 minutes to ensure shape fixing. The load was released at 0.03 N/min and samples were heated back to 80°C at 2°C/min to measure shape recovery. This procedure was repeated thrice for each sample. Shape fixity (R_f) and Shape Recovery (R_r) were measured in each cycle (N) according to **Equations 1** and **2,** respectively, where ε_m is the maximum strain at loading, ε_u is strain after unloading (fixed shape), and ε_p is the remaining strain after recovery (permanent strain).

$$R_r(N) = \frac{\epsilon_m - \epsilon_p(N)}{\epsilon_m - \epsilon_p(N-1)} \qquad\qquad (1)$$

$$R_f(N) = \epsilon_u/\epsilon_m \qquad\qquad (2)$$

3.2.7   Cytocompatibility. Samples (n=3) that were not loaded with drugs were cut using a 6 mm biopsy punch (Fisher Scientific, Waltham, MA, USA), placed in 15 ml DI water, and sonicated (CPX Digital Series Ultrasonic bath, Fisher Scientific, Waltham, MA, USA) constantly over one week. The surrounding solution was changed every 2 hours during the first two days and then changed twice over the remaining 5 days. On the last day, samples were placed in sterile PBS and sonicated

86

overnight. Samples were then sterilized via UV-C radiation (UV sterilizer and sanitizer cabinet, Skin Act, Pacoima, CA, USA) for 3 hours. NIH/3T3 Swiss Mouse Fibroblasts (ATCC-CCL92, Manassas, VA, USA, passage 6) were seeded onto 24 well plates at a density of 10,000 cells/well and incubated for 24 hours. The cells were cultured with Dulbecco's Modified Eagle Medium supplemented with 10% heat-inactivated fetal bovine serum, and 1% penicillin-streptomycin (P/S, Gibco, Thermo Scientific, Waltham, MA, USA). Cell morphology was assessed using Zeiss Axiovert inverted microscope to confirm uniform cell distribution. Sterilized samples were placed in 0.4 µm Transwell® inserts in a 24 well cell culture plate to measure indirect cytocompatibility at 3, 24, and 72 hours using a Resazurin cell viability assay. At each time point, samples and Transwells® were removed from the plate. The media in each well was replaced with resazurin stain after rinsing with sterile PBS. Fluorescence from cells was measured using a plate reader (FLx800, BioTek Instruments Inc, Winooski, VT, USA) at 570 nm. Cytocompatibility was assessed according to **Equation 3**. Cells (n=3) not exposed to any samples or Transwells® were used as positive cytocompatible controls and cells exposed to 20 µl of 30% H_2O_2 were used as negative cytotoxic controls.

$$Cytocompatibility\ (\%) = \frac{abs570(x) - abs570(negative)}{abs570(positive) - abs570(negative)}\ x\ 100 \qquad (3)$$

3.2.8   Drug Release.

3.2.8.1 Magnetic Circuit. The magnetic coil consisted of 200 turns of 36 AWG magnet winding wire, wound across four coils (3D printed acrylonitrile butadiene styrene, 5 cm long, 2 cm wide) in parallel to generate a maximum magnetic field strength of 5 mT. A relay switch was used along with a digital timer

(Panasonic LT4H-DC24V) to generate an alternating magnetic field at a frequency of 5 Hz. The main power supply was maintained at a constant 12 V. The setup of the circuit is shown in **Figure 3.1b**. Polymers were subjected to the alternating field by placing the samples in a reservoir (3D printed, 10 ml volume) within the coils for 10 minutes with alternating magnetic field strength of 0.5 mT and 5 Hz frequency.

3.2.8.2 Drug Release Measurements. Samples (n=3) were placed in 6 ml PBS in 20 ml scintillation vials at 37°C. At set time points and/or after exposure to the magnetic field, the surrounding solution was aliquoted and mixed with DMSO (2X dilution) before evaluation via UV-visible light spectroscopy (Evolution 60, Thermo Scientific, Waltham, MA, USA). Drug/dye concentrations were quantified using reference peaks (Rhodamine B: 555 nm, 6-MP: 333 nm, Dox: 480 nm) to assess release over time. Samples containing single polymer composition and a single drug were either subjected to an alternating magnetic field for 40 minutes or placed in an oven at 37°C for 40 minutes to compare drug release with and without exposure to a magnetic field, **Figures 3.5 and 3.6**. Samples containing dual drug combinations, **Figure 3.7**, were subjected to an alternating magnetic field for 10 minutes at each time point (1 hour, 4 hours, and 7 hours) to initiate shape change and subsequent drug release. To compare release rates between strained and unstrained samples, different amounts of strains were applied to samples depending on their stretchability (assessed based on their elastic deformation range during tensile testing). HPED TEG and

HPED PPG samples were stretched at 20% strain, while PPG TEG was stretched to 40% strain, **Figure 3.5b**.

3.2.9 **Statistics** ANOVA with Tukey's post hoc was used to compare sample measurements. Statistical significance was taken as $p<0.05$.

3.3   Results and Discussion

3.3.1   Hydrophobicity. PPG TEG had the highest water contact angle of 92°, followed by HPED PPG at 69°, and HPED TEG at 58° as seen in **Figure 3.2a**. An increase in hydrophobicity was observed amongst the samples with PPG in the polymer network, and PPG incorporation resulted in a waxy outer layer that helped to repel water and delay polymer wetting. In general, major factors that contribute to increased hydrophobicity are network homogeneity and longer carbon chains.[20] PPG has a relatively higher carbon content compared to the other hydroxyl-containing monomers shown in **Figure 1a**. The PPG TEG formulation is a linear polymer (vs. crosslinked networks that form with HPED polyols), which enables increased component mobility during polymerization and likely results in higher network homogeneity to further contribute to increased hydrophobicity.
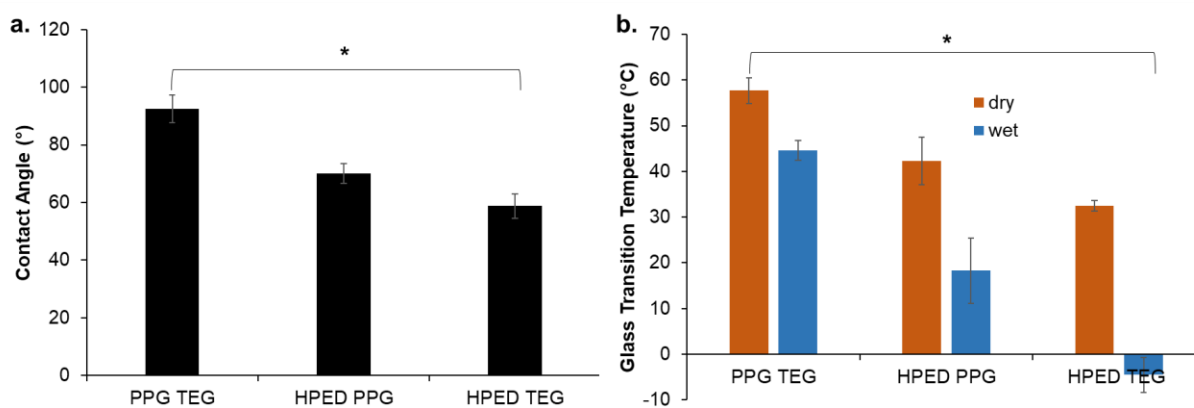
Figure 3.2 (a) Contact angle and (b) glass transition temperature in dry and wet conditions. Mean ± standard deviation displayed. n = 3. *$p < 0.05$ between all formulations and measurement conditions.

3.3.2   Thermal Characterization. A dry glass transition temperature above room temperature would enable stable storage of polymers in their temporary/deformed state during regular storage. A wet glass transition temperature above 37°C would prevent deformed SMPs from changing shape after implantation unless they have been exposed to a localized

increase in temperature (i.e., upon exposure to the magnetic field). Thus, glass transition temperatures were measured in wet and dry conditions for the synthesized polymers, **Figure 3.2b**. All polymers had dry glass transition temperatures above room temperature. The PPG TEG polymer had the highest wet glass transition temperature at 44°C, which is attributed to its increased hydrophobicity. Thus, this polymer has the potential to stably stay in its secondary shape after implantation. In general, wet glass transition temperature trends followed contact angle measurements, with HPED TEG having the lowest wet glass transition temperature due to its increased hydrophilicity, **Figure 3.2b**.

3.3.3 **Mechanical Properties.** A lower elastic modulus and higher elongation at break enable polymer deformation and fixing in the secondary shape. PPG TEG had the lowest elastic modulus of 80 kPa and the highest elongation at a break of 680% in dry conditions, **Table 3.2**. HPED TEG had the highest elastic modulus of 595 kPa, the highest ultimate tensile strength of 29,200 kPa, and lower elongation at a break of 170%. The highly cross-linked network of HPED TEG provides the stiffest polymer, while linear PPG TEG is less stiff, which enables higher elongation at break. It was observed that HPED PPG and HPED TEG formulations underwent plastic deformation upon stretching beyond 40% strain, which limits the strain that can be applied during shape fixing.

Table 3.2 Tensile properties of SMP films. Mean ± standard deviation displayed. n = 3.						
Sample	**Elastic Modulus (kPa)**		**Elongation at Break (%)**		**Ultimate Tensile Strength (kPa)**	
	dry	**wet**	**dry**	**wet**	**dry**	**wet**
PPG TEG	80 ± 35	4 ± 2	680 ± 210	1050 ± 450	8300 ± 3200	1770 ± 120
HPED PPG	46 ± 4	21 ± 2	85 ± 9	94 ± 14	2660 ± 330	1570 ± 70
HPED TEG	595 ± 75	25 ± 2	170 ± 50	40 ± 14	29,200 ± 4000	730 ± 340

3.3.4 Shape Memory Properties. All formulations had shape fixity and recovery above 75%, **Figure 3.3**. This property enables stable fixing of the temporary shape and recovery of the primary

shape upon exposure to a stimulus (i.e., alternating magnetic field). During the tests, all materials were stretched to a maximum of 40% strain to avoid plastic deformation. HPED TEG and HPED PPG formulations utilize net points provided by hydrogen bonding between urethane groups at crosslinking sites to fix their shape. The urethane net points of the PPG TEG formulation are found in the hard segments provided by TEG and HDI, which also rely upon hydrogen bonding to fix their shape. While no significant differences were observed between shape memory properties, PPG TEG had slightly lower shape fixity than the other two formulations. This result could be attributed to the chain mobility restrictions provided by PPG soft segments in this linear polymer.
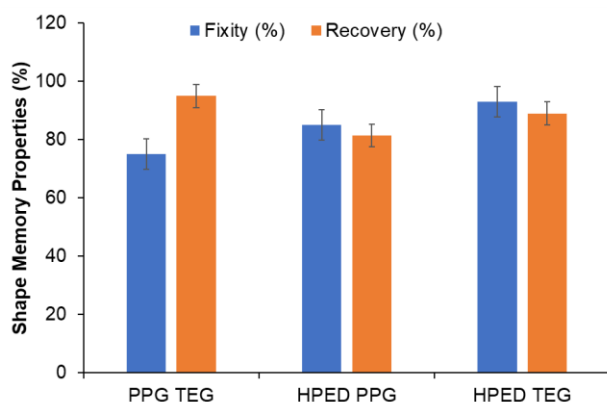
Figure 3.3 Shape memory properties expressed in terms of shape fixity and recovery. Mean ± standard deviation displayed. n = 3. No statistical differences were observed between formulations.

3.3.5 Cytocompatibility. All formulations containing the higher concentration of mnp (100 mg mnp/8 g polymer) had cytocompatibility above 75% over 72 hours, **Figure 3.4**. This result shows that these magnetically-responsive materials are cytocompatible according to ISO 10993-5 standards.[21]
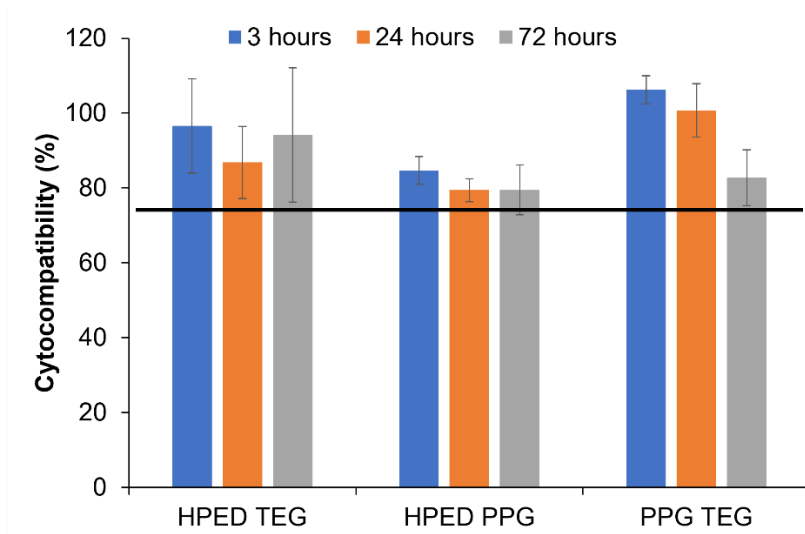
Figure 3.4 Cytocompatibility of 3T3 mouse fibroblasts over 72 hours in the presence of HPED TEG, HPED PPG, and PPG TEG loaded with 100 mg of mnp/8 g of polymer. Mean ± standard deviation displayed. n = 3. The horizontal line denotes ISO 10993-5 standard (75% cytocompatibility).

3.3.6 Magnetic Particles. The size of the paramagnetic Fe_3O_4 particles was determined via dynamic light scattering. The average hydrodynamic particle diameter using DI water as a medium was found to be close to 100 nm, **Figure 3.6a**, thus confirming the formation of mnps with consistent size.

3.3.7 Drug release. Initially, drug release was measured to study the effects of different parameters on release profiles. All release profiles shown were obtained using doxorubicin hydrochloride as the sample drug unless specified otherwise.

3.3.7.1 Effects of polymer formulation. In unstrained samples (containing 100 mg mnp per 10 g sample) with the application of a magnetic field, it was observed that Dox release rates from PPG TEG were fastest compared to those from HPED PPG and HPED TEG, **Figure 3.5a**. This result can be attributed to the linear network of PPG TEG compared to the

crosslinked networks of HPED PPG and HPED TEG. A highly crosslinked network can physically trap the drugs within the structure, thus limiting drug diffusion to the surrounding medium.

3.3.7.2 Effects of applied strain/shape fixing. Dox release was consistently reduced across all formulations when the polymers were strained and fixed in a secondary shape compared to unstrained polymers in their primary shape, **Figure 3.5b**. By straining the samples, the polymer chains are brought closer together, thus creating a barrier to drug diffusion out of the network. Since PPG TEG can be strained to higher amounts without plastic deformation, the difference in release rates between strained (40% strain) and unstrained conditions was the highest for this formulation. Additionally, the high wet glass transition temperature of PPG TEG samples resulted in minimized shape recovery during testing. Due to the limited stretchability of HPED PPG and HPED TEG films (18 to 20% strain applied here), the differences in release profiles before and after straining these materials were smaller, with no significant difference observed in HPED TEG samples. These results also correlate with wet glass transition temperature measurements, indicating that passive shape recovery after plasticization in 37°C water plays a role in this process as well.

3.3.7.3 Effects of drug hydrophobicity. Drug release rates were also influenced by drug hydrophobicity, **Figure 3.5c**. Due to the limited water solubility of Dox and 6-MP, release was carried out in PBS, and then the solutions were diluted with DMSO in a 1:1 ratio to measure the released drug concentration. It was observed that Rhod, which has a higher solubility in water of 15 mg/ml,[22] had the highest release rate from PPEG TEG, followed by Dox with water solubility of 10 mg/ml, and 6-MP with the lowest solubility of 0.5 mg/ml in a 1:1 combination of DMSO and PBS.[23], [24]
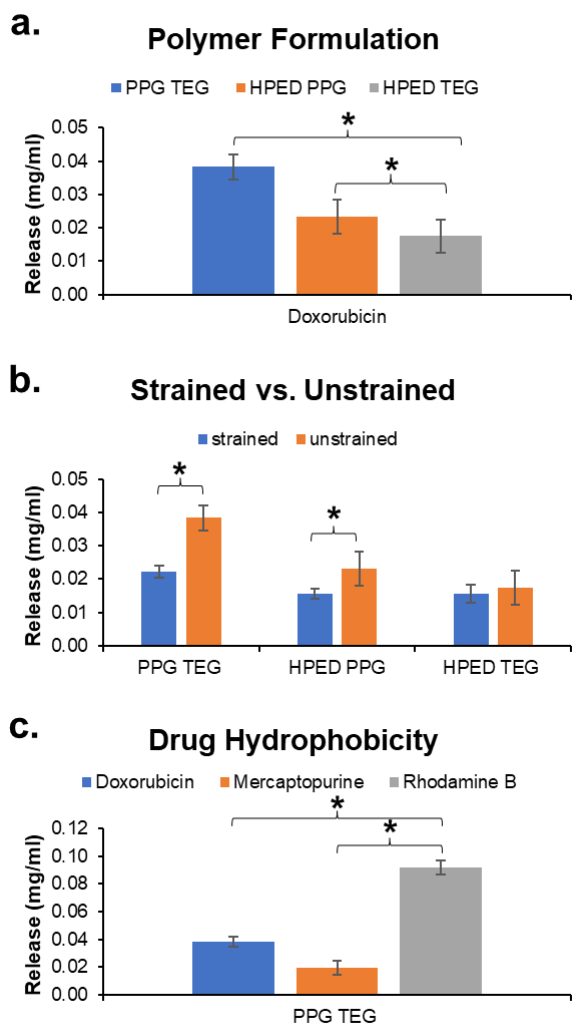
Figure 3.5. Drug release based on the physical and chemical properties of polymers and drugs. (a) Effect of polymer formulation, (b) effect of straining/fixing samples in secondary shapes, and (c) effect of drug hydrophobicity. Mean ± standard deviation displayed. n = 3. *$p<0.05$ between formulations under brackets.

3.3.7.4 Effect of magnetic field. The release of Dox from unstrained polymers was significantly influenced by exposure to an alternating magnetic field, **Figure 3.6b**. Release concentrations were obtained after exposing drug-loaded polymers to an alternating magnetic field for 40 minutes. During this time interval, there was a local increase in the polymer temperature that triggered drug release. The temperature of the surrounding

95

solution was measured using an infrared thermometer to ensure that heat radiated by the magnetic coil and/or the mnp excitation does not transfer to the surroundings. The surrounding solution temperature was $\leq40°C$ during the application of the magnetic field, which should not be harmful to the surrounding cells or tissues. It is hypothesized that exposure to the alternating magnetic field excites the magnetic particles to switch magnetic orientations (north and south) at a frequency of 0.5 Hz. This excitation induces vibrations amongst particles that result in a localized increase in temperature in the polymers, which softens polymer chains to increase drug diffusion out of the network.

3.3.7.5 Effect of mnp concentration. Mnp concentrations can be used as an additional mechanism to control release. Lower mnp concentrations would result in lower localized temperature increases due to smaller vibrations caused by the particles. Thus, reducing mnp concentration resulted in lower drug release during exposure to a magnetic field at the same strength and frequency compared to polymers with higher mnp content, **Figure 3.6c**. The difference in release rates amongst HPED TEG with varied mnp content was lower. This result may be due to increased network crosslink density that limits drug diffusion out of the polymer and/or due to the low wet glass transition temperature, which minimizes the effects of the magnetic field on the already plasticized polymer network.
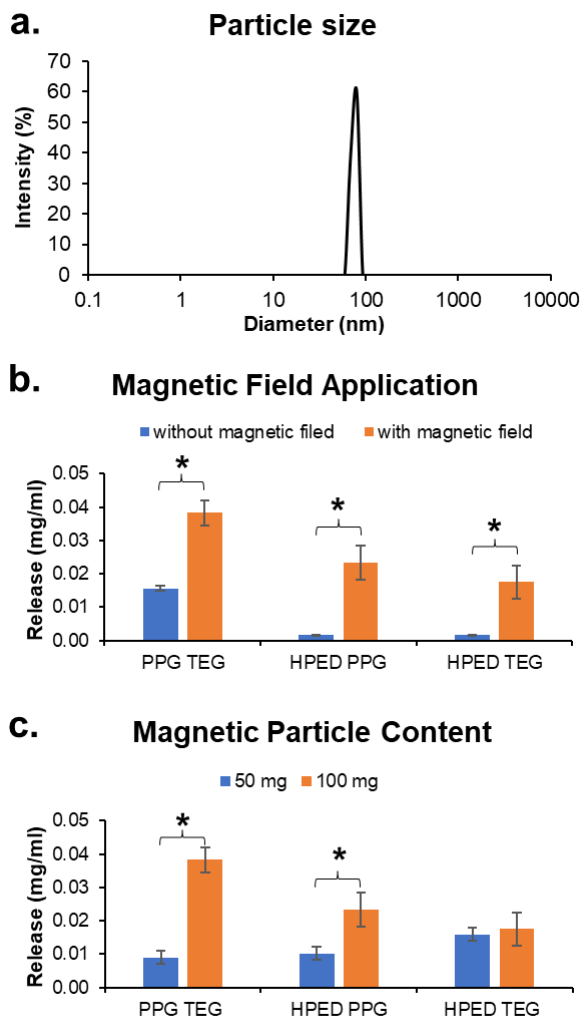
Figure 3.6 Drug release based on magnetic field application. (a) Average magnetic nanoparticle size (n = 5), (b) Effect of a magnetic field, and (c) Effect of magnetic particle content on Dox release. Mean ± standard deviation displayed. n = 3. *$p < 0.05$ between formulations under brackets.

3.3.8 Dual drug release. After comparing the release profiles from individual formulations, a scaffold was prepared to achieve a dual release profile of two different drugs (6-MP and Rhod) from a single polymer composite with varying polymer composition and mnp loading. Films were tested either unstrained in primary shape (**Figure 3.7 c** and **d**) or strained and fixed in secondary shape (**Figure 3.7 a** and **b**). A subset of films were exposed to an alternating magnetic field for 10 minutes at 1, 4, and 7 hours, and drug release was

characterized after each exposure (indicated by arrows on **Figure 3.7 a** and **c** charts). A set of controls was run in which samples were simply incubated in PBS at 37°C without exposure to the magnetic field, **Figure 3.7 b** and **d**. The left side of the sample was composed of HPED TEG with 50 mg mnp and was therefore designed to release 6-MP slowly over time. The right side of the sample was composed of PPG TEG containing 100 mg mnp and was designed to rapidly release Rhod.

The strained, heat-activated samples in **Figure 3.7b** were stored at 37°C in PBS to mimic passive release in body conditions. Minimal drug release was observed in these samples without remote actuation, indicating that drug release can be controlled with application of the magnetic field. The unstrained samples stored at 37°C in PBS had higher release rates (**Figure 3.7d**), showing that the use of SMPs can be used to more finely control drug release. In both tests that were conducted without magnetic actuation, differential release rates were observed, with faster release of rhodamine and slower release of 6-MP.

These trends were also seen in the magnetically-actuated samples, with the highest drug release measured from unstrained samples with application of magnetic field, **Figure 3.7c**. The strained samples with magnetic actuation provided increased control over release, with higher release as compared with unstrained, heated samples and lower release as compared with strained, heated samples and unstrained, magnetically-actuated samples, **Figure 3.7a**.

The difference in release rates between the two sides of the polymer composite demonstrates the ability to control drug release rates. This proof of concept can be utilized in future work to achieve dual drug release of two different drugs with distinct release profiles from a single implant. The heat-activated samples at 37°C in PBS, mimic the body

conditions at 37°C and demonstrate minimal drug release without remote actuation in the strained condition.
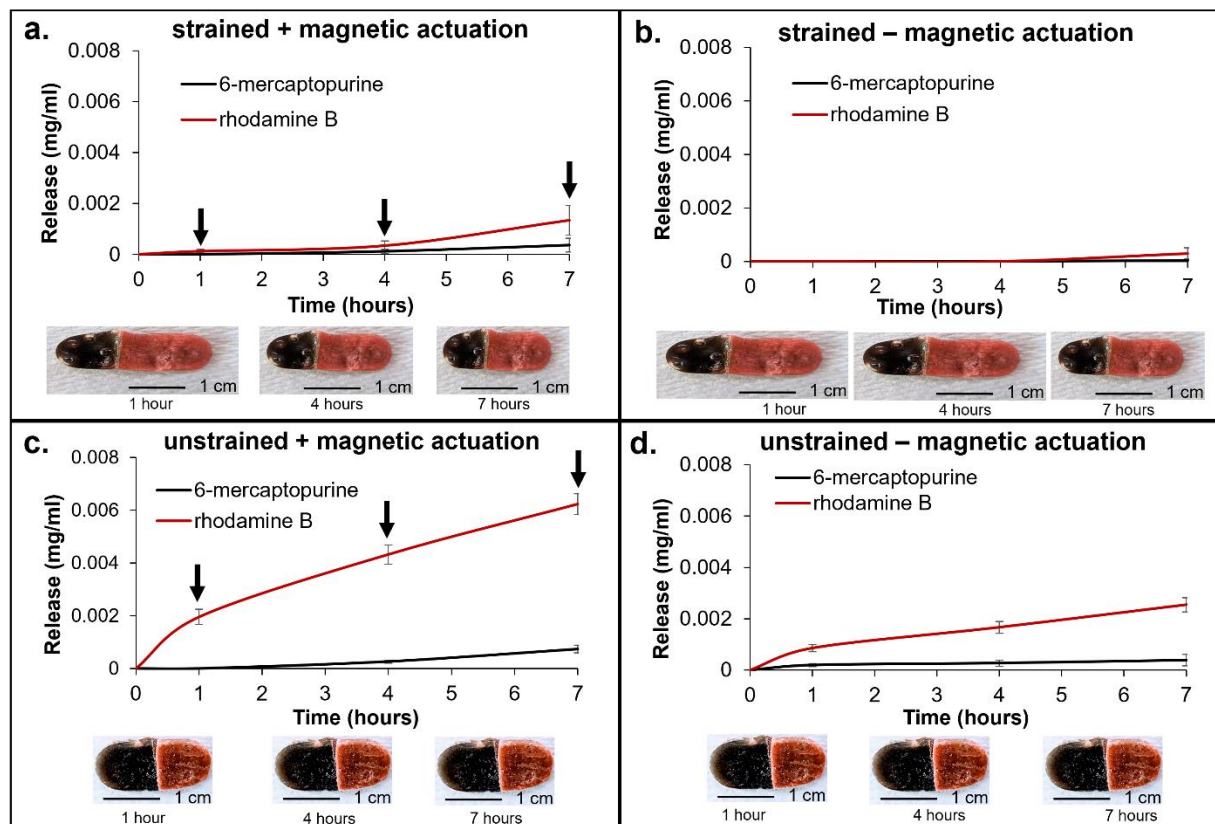
Figure 3.7 Dual drug release from a single scaffold. 6-MP and rhodamine were released from strained polymer samples (a) under magnetic actuation and (b) without magnetic actuation. 6-MP and rhodamine release rates were measured from the same unstrained samples (c) under magnetic actuation and (d) without magnetic actuation. The downward arrow indicates time points at which polymers were exposed to an alternating magnetic field for 10 minutes (a and c) and tested for drug release. Images depicting a change in polymer dimensions (i.e., shape recovery) upon each magnetic field application are presented in (a) and (b), while images in (c) and (d) show that unstrained samples did not change shape during testing. Mean ± standard deviation displayed. n = 3.

3.3.9 Design principles for SMP-based drug delivery devices. Initially, it was hypothesized that PPG TEG would have the slowest drug release rate due to its highest contact angle (**Figure 3.2a**) and highest wet glass transition temperature (**Figure 3.2b**). However, it was observed that PPG TEG had the fastest drug release amongst all the tested formulations (**Figure 3.5a**), which was attributed to its linear thermoplastic form compared to the other polymer compositions (HPED TEG and HPED PPG) that have a chemically crosslinked (thermoset) network. This result shows that the amount of crosslinking within the polymer network has a greater impact on controlled release. Crosslinked networks can physically trap drugs to a greater extent, even in samples with lower transition temperatures and contact angles that are hydrated and plasticized in aqueous conditions.

Magnetic particle content also had a significant impact on drug release, which can improve control compared with prior work that relies upon passive release. For example, Sivak et al., previously developed polyurethane foams for the simultaneous release of two chemotherapeutic drugs, DB-67 and Dox.[25] In that work, hydroxyl and amine groups on the drugs were allowed to react with the isocyanate groups of lysine diisocyanate methyl ester during polyurethane foam synthesis. This system depends on hydrolytic degradation of the polymeric network and subsequent release of the drugs and exhibited extremely slow degradation (<0.1% as of day 70). This slow degradation contributed to extremely slow release of drugs. The fastest release rates (80 mol% release within 70 days) were obtained at 70°C, which renders the system incompatible for biomedical applications.

Transdermal microneedles were previously used to deliver Dox *in vivo* across rat skin by Chen et al.[26] This application achieved robust control over the release of doxorubicin embedded within caprolactone microneedles containing photosensitive nanomaterials.

Infrared light was used to melt the microneedles and subsequently trigger drug release. This method achieved high precision over release rate via the number of on-off cycles used, but is limited to transdermal drug release. The proof of concept shown in this work attains high precision over differential release rates of two drugs by tuning the polymer crosslinking, straining polymers into temporary secondary forms, altering the concentration of mnps, and through the application of an alternating magnetic field. This system could be applied to a similar transdermal patch or as an implanted drug depot in future work to provide on-off release of drugs. Further future work will consider the removal of the drug-delivery vehicles either surgically or via degradation after drug release is achieved.

3.4 Conclusions

This study provides a proof-of-concept for a unique way to tune drug delivery rates and achieve remote on-demand drug delivery from an implanted material via application of an alternating magnetic field. High cytocompatibility of the magnetically-actuated SMPs indicates that these polymers may be suitable for future use in on-demand drug delivery. Tuning the overall polymer network provides varied mechanical and shape memory properties, which influence drug release from the materials. These scaffolds enable control over the frequency and dosage of drug delivery as required. This system could either be used to administer a single drug over multiple time points or to administer multiple drugs simultaneously. The concentration of mnps present can be used to further alter the drug delivery rate. These materials could be implanted at the target site (e.g., a carcinoma), and localized and sustained drug delivery could be triggered remotely as required to avoid multiple intravenous infusion therapies. In future work, drugs could be loaded within microspheres to achieve greater control over release rates based on alterations in the polymer chemistry and crosslink density and the effects of magnetic field application through tissues of varying thickness can be studied to assess the potential use of this system as an implanted drug depots.

3.5   References

[1]   A. Tewabe, A. Abate, M. Tamrie, A. Seyfu, and E. A. Siraj, "Targeted drug delivery —
        from magic bullet to nanomedicine: Principles, challenges, and future perspectives," *J.
        Multidiscip. Healthc.*, vol. 14, pp. 1711–1724, 2021.

[2]   R. K. Tekade, R. Maheshwari, N. Soni, M. Tekade, and M. B. Chougule,
        "Nanotechnology for the Development of Nanomedicine," in *Nanotechnology-Based
        Approaches for Targeting and Delivery of Drugs and Genes*, Elsevier, 2017, pp. 3–61.

[3]   C. D. Delivery, *Controlling drug delivery*, vol. 8, no. 3. 1999.

[4]   A. Hillery and K. Park, Eds., *Drug Delivery: Fundamentals and Application*, Second (2n.
        Boca Raton: CRC Press, 2016.

[5]   M. Husch, C. Sullivan, D. Rooney, C. Barnard, M. Fotis, and J. Clarke, "Insights from the
        sharp end of intravenous medication errors: implications for infusion pump technology,"
        Qual Saf Heal. Care, vol. 14, pp. 80–86, 2005.

[6]   A. Vijayakumar, E. Sharon, J. Teena, S. Nobil, and I. Nazeer, "A clinical study on drug-
        related problems associated with intravenous drug administration," *J. Basic Clin. Pharm.*,
        vol. 5, no. 2, p. 49, 2014.

[7]   B. R. King, "Alternative Routes of Drug Administration," *Emerg. Med. News*, vol. 27, no.
        8, pp. 23–24, Aug. 2005.

[8]   Y. H. Yun, B. K. Lee, and K. Park, "Controlled Drug Delivery: Historical perspective for
        the next generation," *J. Control. Release*, vol. 219, pp. 2–7, Dec. 2015.

[9]   M. R. Prausnitz, S. Mitragotri, and R. Langer, "Current status and future potential of

transdermal drug delivery," *Nat. Rev. Drug Discov.*, vol. 3, no. 2, pp. 115–124, Feb. 2004.

[10] M. R. Prausnitz, "Microneedles for transdermal drug delivery," *Adv. Drug Deliv. Rev.*, vol. 56, no. 5, pp. 581–587, Mar. 2004.

[11] S. H. Bariya, M. C. Gohel, T. A. Mehta, and O. P. Sharma, "Microneedles: an emerging transdermal drug delivery system," *J. Pharm. Pharmacol.*, vol. 64, no. 1, pp. 11–29, Jan. 2012.

[12] P. Pflegel, "Pulsatile Drug Delivery- Current Applications and Future Trends. Herausgegeben von Robert Gruny, Genf, Hans E. Junginger, Leiden, und Nikolaos A. Peppas, West Lafayette (Indiana). Stuttgart 1993, 186 Seiten, zahlreiche Abbildungen und Tabellen. ISBN 3-804," *Pharm. Unserer Zeit*, vol. 23, no. 4, pp. 265–266, Jan. 1994.

[13] A. Chunder, S. Sarkar, Y. Yu, and L. Zhai, "Fabrication of ultrathin polyelectrolyte fibers and their controlled release properties," *Colloids and Surfaces B: Biointerfaces*, vol. 58, no. 2. pp. 172–179, 2007.

[14] C. J. Carling, M. L. Viger, V. A. Nguyen Huu, A. V. Garcia, and A. Almutairi, "In vivo visible light-triggered drug release from an implanted depot," *Chem. Sci.*, vol. 6, no. 1, pp. 335–341, Dec. 2014.

[15] N. SATARKAR and J. HILT, "Magnetic hydrogel nanocomposites for remote controlled pulsatile drug release," *J. Control. Release*, vol. 130, no. 3, pp. 246–251, Sep. 2008.

[16] Q. Zhao, M. Behl, and A. Lendlein, "Shape-memory polymers with multiple transitions: complex actively moving polymers."

[17] M. C. Serrano, L. Carbajal, and G. A. Ameer, "Novel biodegradable shape-memory

elastomers with drug-releasing capabilities," *Adv. Mater.*, vol. 23, no. 19, pp. 2211–2215, May 2011.

[18]   A. U. Vakil, N. M. Petryk, E. Shepherd, and M. B. B. Monroe, "Biostable Shape Memory Polymer Foams for Smart Biomaterial Applications," *Polymers (Basel).*, vol. 13, no. 23, p. 4084, Nov. 2021.

[19]   M. Ramezani and M. B. B. Monroe, "Biostable Segmented Thermoplastic Polyurethane Shape Memory Polymers for Smart Biomedical Applications," *ACS Appl. Polym. Mater.*, vol. 4, no. 3, pp. 1956–1965, Mar. 2022.

[20]   W. Chen, V. Karde, T. N. H. Cheng, S. S. Ramli, and J. Y. Y. Heng, "Surface hydrophobicity: effect of alkyl chain length and network homogeneity."

[21]   P. ISO, "ISO 10993-5:2009 Biological evaluation of medical devices -- Part 5: Tests for in vitro cytotoxicity," *International Organization for Standardization, Geneva*. p. 34, 2009.

[22]   "Product Information - rhodamine B," no. 8610, p. 58333030, 2017.

[23]   "Product Information - doxorubicin-(hydrochloride)," vol. 9, no. 16143, p. 48108, 2013.

[24]   "Product Information 6-mercaptopurine," no. 8610, p. 58333030, 2017.

[25]   W. N. Sivak, J. Zhang, S. Petoud, and E. J. Beckman, "Simultaneous drug release at different rates from biodegradable polyurethane foams," *Acta Biomater.*, vol. 5, pp. 2398–2408, 2009.

[26]   M. C. Chen, M. H. Ling, K. W. Wang, Z. W. Lin, B. H. Lai, and D. H. Chen, "Near-infrared light-responsive composite microneedles for on-demand transdermal drug delivery," *Biomacromolecules*, vol. 16, no. 5, pp. 1598–1607, May 2015.

Chapter IV

Antimicrobial shape memory polymer hydrogels for

chronic wound dressings

4.1   Introduction

Wound care is a multibillion-dollar industry with $20 billion in annual costs[1]. Wounds that fail to heal within the expected time frame (~4 weeks)[2] and do not respond to regular wound care treatment are considered chronic wounds[3]. On average, chronic wounds affect approximately 2% of the American population annually[1][4]. These slow-healing wounds can cause severe pain and discomfort due to prolonged inflammation, and they are highly susceptible to infection. In severe cases, non-healing wounds require amputation. For example, in a study performed by a general hospital in Indonesia, it was found that 48% of diabetic foot ulcer patients required lower extremity amputation.[5]

Currently, chronic wound treatment options primarily involve cleaning the wound repeatedly, debridement, application of wound dressings, compression stockings/bandages, and antibiotics. More complex and expensive approaches include hyperbaric oxygen therapy, ultrasound and electromagnetic therapy, negative pressure wound therapy, and skin grafts. Repeated debridement and wound cleaning along with frequent bandage replacement can cause further discomfort and increased infection risks. Thus, improved wound dressing materials that effectively cover wounds and conform to wound walls to block entry of external bacteria could improve outcomes in chronic wounds. One such option involves moderately adsorbent hydrocolloids that can absorb small amounts of wound exudate and seal the wound.[6] However, there is a possibility that hydrocolloids can trap the bacteria already present in the wound, rendering them unsuitable in cases where chronic wounds are already infected.

Alternatively, complete wound closure could be achieved by injectable hydrogels. Hydrogels are three-dimensional crosslinked polymer networks that can absorb large amounts of water (up to 10 times their dry weight). Hydrogels are typically made up of water-soluble polymers, and their

crosslinked networks are resistant to dissolution in the body. Hydrogels can either be termed as permanent gels[7] formed by a chemically crosslinked network, or physical gels[8] formed by reversible physical interactions, such as hydrogen bonding or Van der Waals forces. Hydrogels have a high potential to mimic the native skin extracellular matrix due to their high tunability and hydrated molecular structure[9]. Both natural[10], [11] and synthetic[12], [13] hydrogels have been explored as potential candidates to treat skin defects. Some injectable hydrogels include Pluronics that comprises a triblock copolymer of polyoxyethylene (PEO) and polyoxypropylene (PPO). Pluronics have been used for continuous and controlled drug delivery at the implant site.[14][15] Curcumin-loaded injectable Pluronic hydrogels were combined with gelatin to accelerate chronic burn healing and reduce scar formation.[16] These composite hydrogels promoted the adhesion and proliferation of fibroblasts, indicating good cytocompatibility.

Another option for improved chronic wound filling is shape memory polymers (SMPs). SMPs are 'smart' materials that can be deformed and stored in a temporary geometry and then triggered to return to their original shape upon exposure to an external stimulus, such as heat, pH, electrical impulse, or alternating magnetic field. SMP foams have been developed that utilize body temperature heating as a stimulus to trigger shape change.[17]–[19] Here, we developed synthetic poly(ethylene glycol) (PEG)-based polyurethane SMP hydrogels as a potential wound dressing material. The high hydrophilicity of PEG could increase exudate absorption and subsequent swelling of hydrogels, allowing the hydrogels to maintain a moist environment, which may reduce pain.[20] Antifouling properties of PEG could minimize adherence to underlying wounds.[21] By combining PEG with a polyurethane network, shape memory properties can be achieved. Here, these hydrogels were prepared as porous foams. These foams can be compressed and stored into a constricted temporary geometry that enables easy application to wounds. Then, the hydrogel foams

can expand back to their primary shape after implantation and heating to body temperature to fill up and seal irregularly shaped wounds.

In addition to effectively filling chronic wounds, one major concern with synthetic hydrogels involves reducing infection risks. To prevent antibiotic overuse, plant-based phenolic acids have proven beneficial as non-drug-based antimicrobials that are effective against multi-drug resistant organisms (MDROs).[22], [23]. Phenolic acids work by destabilizing bacteria cytoplasmic membrane, altering the permeability of the bacteria plasma membrane, inhibiting extracellular microbial enzymes, directly altering microbial metabolism, and/or depriving microbes of the substrate required for growth.[24] Previously, phenolic acids were chemically crosslinked into polyurethane networks to provide antimicrobial scaffolds.[23] To simplify scaffold fabrication and enable phenolic acid release over time, we focused on the physical incorporation of phenolic acids into these SMP hydrogels to provide antimicrobial scaffolds. In addition to antimicrobial properties, the hydroxyl groups on the phenol rings can potentially hydrogen bond to urethane linkages in these hydrogels to increase the net points and improve the shape memory properties. Increased shape fixity allows more stable storage in the temporary shape before implantation, and increased shape recovery enables rapid would filling upon implantation.

In this research, we prepared polyurethane SMP hydrogels as bulk scaffolds and foams with varying PEG molecular weights. Phenolic acids, including cinnamic acid (CA), p-coumaric acid (pCA), and caffeic acid (Caff), were physically incorporated into the hydrogel network at low and high concentrations. The resulting polymers were then characterized in terms of shape memory and antimicrobial properties. Retention of antimicrobial properties in the scaffolds and the surrounding media was characterized over one month of storage in phosphate-buffered saline.

4.2 Materials and Methods

4.2.1 Materials. Polyethylene glycol ($M_n = 4000$ Da and $M_n = 6000$ Da), triethanolamine (TEA), glycerol ethoxylate ($M_n = 1000$ Da), dibutyltin dilaurate (DBTDL), hexamethylene diisocyanate (HDI), granulated sodium chloride (NaCl), cinnamic acid (CA), trans-p-coumaric acid (pCA), caffeic acid (Caff), chloroform, dimethyl sulfoxide (DMSO), acetone, isopropanol, and Contrad® solution were purchased from Fisher Scientific (Waltham, MA, USA). All chemicals used were reagent grade. PEG 4000, PEG 6000, and glycerol ethoxylate were dehydrated under vacuum overnight to remove any trace amounts of moisture before use. Sodium chloride granules were segregated using mesh screens to obtain fine granules within the 300 to 500 µm size range and dehydrated under vacuum overnight before use.

4.2.2 Hydrogel Synthesis. Two formulations were used as the basis on which the chemical and surface modification were studied. A combination of diols (PEG) and triols (TEA and glycerol ethoxylate) was used in each formulation. To ensure structural integrity and three-dimensional network formation, at least 80% of the hydroxyl groups were from the triols. The compositions of both formulations are shown in **Table 4.1** on a weight basis that includes the amount of catalyst and monomers used. A schematic representation of hydrogel formation is shown in **Figure 4.1**. Side A materials represent the hydroxyl-containing components, and Side B materials denote isocyanate-containing components, which were combined to prepare a polyurethane hydrogel. All hydroxyl components were dissolved in chloroform before the addition of HDI. Then, the catalyst, DBTDL, was added. All additions were performed in a glove box at <4% relative humidity under an inert nitrogen atmosphere. The reaction components were mixed in a speed mixer (Flacktek,

Landrum, SC, USA) at 3500 rpm for 30 seconds. Reaction mixtures were poured onto 90 mm diameter polystyrene Petri dishes lined with a Teflon liner to form hydrogel films.

A subset of reaction mixtures was mixed with sodium chloride granules before speed-mixing to form 70% porous (volume basis) foams. To ensure 70% porosity, the total volume of monomers was first estimated based on the density of each monomer. Then, the volume of NaCl added to each formulation was measured using a graduated cylinder to be 70% of the total monomer volume. Both films and foams were allowed to react in an oven for 24 hours at 50°C to ensure complete reaction and then vacuum dried under -1015 mbar at 40°C to remove excess chloroform from the network. Foams were stored in water for 48 hours with the water changed at 24 hours to wash out NaCl and provide open pores. Hydrogel films and foams were washed with water twice, 20% Contrad®, isopropanol, and then acetone to remove catalysts and unreacted monomers. All washing volumes were 20 times the volume of samples. After washing, samples were dried overnight under a vacuum. Phenolic acids (CA, pCA, and Caff) were physically incorporated into the dry hydrogel network by soaking the hydrogels in 5 and 10 wt% phenolic acid solutions in DMSO overnight at 50°C. Samples were then dried for 72 hours under a -1015 mbar vacuum at 40°C to ensure complete removal of DMSO. Dried samples were cut to required shapes for specific testing as described in the following sections.
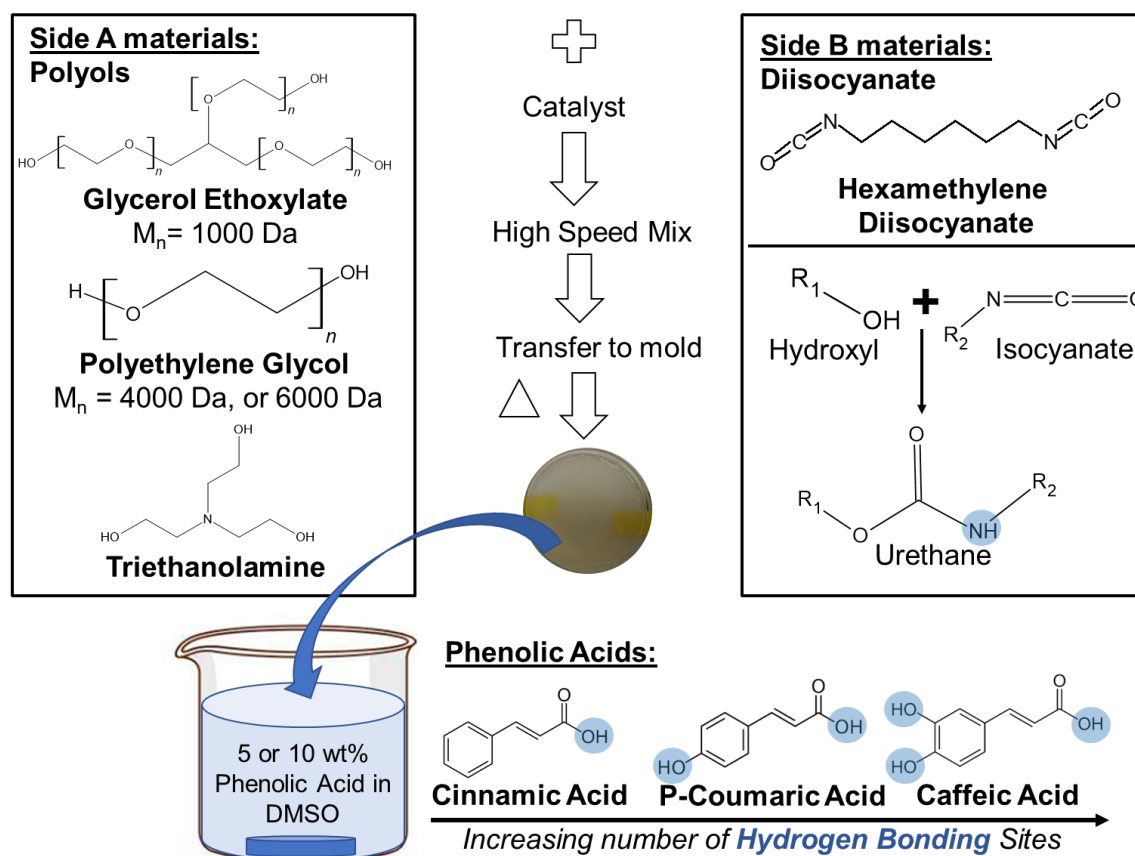
Figure 4.1 Synthesis of PEG 4000 and PEG 6000 hydrogels loaded with phenolic acids.

Table 4.1 Reactive components of synthesized base hydrogel compositions in wt% with resulting gel fraction and swelling ratios. Mean ± standard deviation displayed. n = 3.

Sample Name	HDI	PEG 4000 (4000 Da)	PEG 6000 (6000 Da)	TEA	Glycerol ethoxylate (1000 Da)	DBTDL	Gel fraction (%)	Swelling Ratio
PEG 4000	14.38	61.55	- -	3.06	20.51	0.49	97.7 ± 0.3	1.92 ± 0.02
PEG 6000	10.92	- -	70.16	2.32	15.6	0.99	96.6 ± 0.4	2.57 ± 0.02

4.2.3 Spectroscopic Analysis. The surface chemistry of dry hydrogel films was analyzed using a Nicolet i70 attenuated total reflectance (ATR)-Fourier transform infrared (FTIR) spectrometer (Fisher Scientific, Waltham, MA, USA) at 4 cm^{-1} resolution using OMNIC software (Fisher Scientific, Waltham, MA, USA). An average of 16 scans was used to

generate a spectrum to confirm the physical absorption of phenolic acids onto the hydrogels.

4.2.4 **Gel fraction and swelling ratio**. Post synthesis and before washing, 6 mm diameter punches were cut from hydrogel films and dried under vacuum at -1015 mbar at 40°C for 24 hours to remove any chloroform used as a solvent. For gel fraction measurements, the samples were weighed (initial dry weight) and placed in chloroform at 50°C for 24 hours to wash out any unreacted components. The washed samples were then vacuum dried again at -1015 mbar and 40°C and weighed again (dried sample weight) to measure gel fraction according to **Equation 1**. Parallelly, a second set of dried samples was weighed, placed in water at 50°C for 24 hours, and weighed again in the wet state to measure the swelling ratio according to **Equation 2**.

$$Gel\ fraction = \frac{initial\ dry\ weight}{dried\ sample\ weight}\ x\ 100\% \qquad (1)$$

$$Swelling\ ratio = \frac{swollen\ weight - dry\ weight}{dry\ weight} \qquad (2)$$

4.2.5 **Phenolic acid loading.** To measure phenolic acid loading, cylinders were weighed in the dry state after gel fraction measurements (i.e., after removing unreacted components) and then loaded with phenolic acids as described in Section 4.2.2. Samples were dried under vacuum again, and the difference in dry masses before and after loading was taken as the mass of physically incorporated phenolic acids.

4.2.6 **Thermal analysis**. Thermal analysis was performed on hydrogel films before and after phenolic acid incorporation. A thermogravimetric analyzer (TGA Q500, TA instruments, Newcastle, DE, USA) was used to identify the temperature at which 3% mass loss occurs

by heating 10 mg of the dry sample across a temperature range from 0 to 600 °C at 10°C/min. This temperature was used as the upper limit at which samples were heated to identify their melting temperatures (T_m) using a differential scanning calorimeter (DSC Q200, TA Instruments, Newcastle, DE, USA). Dry sample slices (3 to 5 mg) were loaded in t-zero aluminum pans. During the analysis, samples were equilibrated at -60°C, kept isothermally for 2 minutes, heated to 100 °C at 10°C/min, kept isothermally for 2 minutes, cooled to -60°C at -10°C/min, kept isothermally for 2 minutes and heated back to 100°C at 10°C/min. The T_m was measured as the endothermic peak minima temperature during the second heating cycle.

4.2.7 Shape memory properties. A dynamic mechanical analyzer (DMA Q800, TA Instruments, Newcastle, DE, USA) was used in controlled force mode to measure shape fixity and shape recovery ratios as an indication of the overall shape memory behavior of hydrogel films before and after the physical incorporation of phenolic acids. Samples (n=3) were cut from the prepared hydrogel films using a dog bone punch according to ASTM D638 Type IV (scaled down by a factor of 4; length: 6.25 mm, width: 1.5 mm). The samples were heated to 60°C and kept isothermally for 2 minutes. Then, a controlled force was applied to stretch the samples to a 40% strain at 0.03 N/min. The maximum force applied was limited to 18 N. Samples were then cooled to -5°C and kept isothermally for 2 mins to ensure shape fixing. Samples were unloaded at 0.03 N/min and heated back to 60°C at 3°C/min to measure shape recovery. This cycle was repeated thrice, and recovery ratio (R_r) and fixity ratio (R_f) were measured at each cycle using **Equations 3** and **4**, respectively, where ϵ_u is the strain after unloading (the fixed shape), ϵ_m is the maximum strain at loading, and ϵ_p is the remaining strain after recovery (permanent strain).

$$R_r(N) = \frac{\epsilon_m - \epsilon_p(N)}{\epsilon_m - \epsilon_p(N-1)} \tag{3}$$

$$R_f(x) = \epsilon_u/\epsilon_m \tag{4}$$

To test the shape memory properties of foams, samples (n=3) were cut into cylinders (diameter = 6 mm, length = 1 cm), heated above their transition temperature, and crimped radially using a radial compression crimper (Blockwise Engineering, Tempe, AZ, USA) into a temporary low-profile geometry, A Nitinol wire (diameter = 3 mm) was passed through the foam samples to hold them in place, and foams were allowed to expand in a water bath at 37°C. Images were captured using a camera at 5 second intervals over 10 minutes. Volume was measured at each interval using the diameter and the length of the cylinder in the images. Images were analyzed using ImageJ to quantify foam dimension over time, and % volume recovery was measured at each time point (t) according to **Equation 5**. Volume recovery was plotted over the expansion time frame.

$$\text{Volume recovery (\%)} = \frac{\text{sample volume (t)}}{\text{expanded volume}} \times 100\% \tag{5}$$

4.2.8   Mechanical properties. To test compressive mechanical properties, 8 mm punches (n=3) were cut from the foams and incubated with phenolic acid solutions overnight. Samples were then dried under a -1015 mbar vacuum at 40°C for two days to ensure complete removal of DMSO. Samples were soaked in DI water at 50°C for 3 hours to allow them to swell. Control hydrogels without phenolic acids were simply swollen in DI water. Before testing, wet samples were removed from the water, lightly patted, and cut to ensure that the diameter to height ratio was maintained at 2:1. Samples were compressed using a 24 N load cell (Test Resources, Shakopee, MN, USA) until failure. Compressive modulus was measured from 0 to 2% strain.

115

4.2.9 **Antibacterial property evaluation**. *Escherichia coli* (*E. coli,* 397E strain, ATCC, Manassas, VA, USA) was used to test the antimicrobial efficacy of phenolic acid-containing hydrogels. Samples (n=3) were punched from hydrogel films and sterilized via UV-C radiation for 3 hours. Silver-based foam dressings (AREZA MEDICAL, Dallas, TX, USA) were cut to similar dimensions as the samples and served as positive (antimicrobial) controls. Hydrogels without phenolic acid incorporation served as negative controls. *E. coli* was cultured as previously described[25]. Briefly, bacteria were incubated in 5 ml sterile lysogeny broth (LB, prepared at 25 g/L of deionized water and autoclaved) at 37°C. After 16 hours, 1 ml of the bacteria solution was transferred to 10 ml of fresh LB and incubated at 37°C until the bacteria reached the logarithmic growth period, at which an optical density of 0.6 at an absorbance of 600 nm was achieved. The optical density was measured using a plate reader (FLx800, Bio-Tek Instruments, Inc.). Then, 100 µl of this bacteria solution was added to each well-containing sample and incubated for 1 hour. The bacteria were diluted by a factor of 10^6 using LB and 3, 10 µl drops were pipetted onto an LB-agar plate from each well. Plates were incubated at 37°C overnight. Images were captured at each drop location after 18 hours, and colony forming unit (CFU) density was qualitatively assessed as a measure of sample antimicrobial properties as previously described.[26]

To characterize antimicrobial property retention, samples were incubated in PBS (2 ml per sample) at 37°C for up to 30 days. PBS was replaced and stored for characterization of surrounding media every 10 days, and a set of samples were removed from PBS at 0, 10, 20, and 30 days for characterization of scaffold properties. The antimicrobial properties of all samples and surrounding media were measured together at the end of the 30-day study.

116

4.2.10 Phenolic acid release. Phenolic acid release from hydrogels was assessed using a UV-vis spectrophotometer (Evolution 60, Fisher Scientific, Waltham, MA, USA). Phenolic acid concentrations were quantified using a reference peak (CA: 270 nm; Caff: 254, 274, and 384 nm; and pCA: 345 nm) to assess release rates over time. To measure release rates, samples with PAs were placed in a microcentrifuge tube containing 2 ml of 1X PBS and incubated at 37°C. Triplicates were prepared for each sample. Separate samples were prepared for each time point – 10, 20, and 30 days. At each time point, the sample was removed from the surrounding media to analyze the bacterial interaction mentioned in the earlier section. The tubes were then agitated via a vortex and 600 µl of PBS was removed to analyze bacterial interactions of the surrounding media. The remaining 1400 µl of PBS from each sample was diluted with 1400 µl DMSO to ensure the complete solubility of phenolic acids in the solution before measuring the PA content using a UV-vis spectrophotometer. The dilution level was taken into consideration while measuring PA release rates. The structure of each PA is shown in **Figure 2a-c**. Control hydrogels were stored in PBS for 1 week, and UV-vis was employed on the surrounding media to ensure that no hydrogel leachables could contribute to the PA release measurement. No measurable absorbance values were obtained with the controls at the wavelength of interest.

4.2.11 Cytocompatibility. Cytocompatibility of samples was measured using 3T3 Swiss mouse fibroblasts (ATCC-CL92; ATCC, Manassas, VA, USA). Cells were cultured in Dulbecco's modified Eagle's medium supplemented with 10% heat-inactivated fetal bovine serum (FBS) and 1% penicillin-streptomycin (P/S, Gibco) at 37°C/ 5% CO_2 for 24 hours). Cells were used at passage 13 after 3 days of culture and seeded onto a 24-well tissue culture

117

polystyrene plate at 10,000 cells/well for 24 hours at 37°C, 5% CO_2. To test the effects of phenolic acids, hydrogel samples were soaked in phenolic acid solutions for 24 hours at 50°C, cut using a 6 mm biopsy punch while swollen, vacuum dried at 40°C and -1015 mbar for 72 hours, and sterilized via UV-C radiation sterilizer (UV sterilizer and sanitizer cabinet, Skin Act, Pacoima, CA, USA) for 3 hours. Sterilized samples were placed in 0.4 µm Transwell® inserts above cells seeded in 24 well plates to measure indirect cytocompatibility of samples. Cells were incubated with samples (n=3) at 37°C, 5% CO_2 for 24 hours. Cells incubated without samples were used as positive (cytocompatible) controls, and cells exposed to 200 µl of 70% methanol for 24 hours were used as negative (cytotoxic) controls. Cytocompatibility was assessed via Live/Dead assay (ThermoFisher Scientific, Waltham, MA, USA). Cells were stained with green-fluorescent calcein-AM (live cells) and red-fluorescent ethidium homodimer-1 (dead cells) for 15 minutes at 37°C while covered with aluminum foil to protect cells from direct light exposure. Cells were imaged via an inverted microscope (Leica, DMI6000) at 10X magnification to determine the number of live (green) and dead (red) cells. Three images were captured per sample well. Cytocompatibility was measured according to **Equation 6**. Additionally, resazurin assay was used to assess cytocompatibility of PEG 4000 and PEG 6000 hydrogels with and without phenolic acids incorporation over a period of one week. Cytocompatibility was measured based on the fluorescence emission 570nm using a plate reader (FLx800, BioTek Instruments, Inc) as per equation 7.

$$\text{Cytocompatibility (\%)} = \frac{\text{live cells}}{\text{total number of cells}} \times 100\% \qquad (6)$$

$$\text{Cytocompatibility (\%)} = \frac{\text{abs570(x)}}{\text{abs control}} \times 100\% \qquad (7)$$

4.2.12 Statistical analysis. Measurements are presented as mean ± standard deviation. The number of measurements was maintained at three for all analysis. Student's t-tests (2-sample, assuming unequal variance) were performed between controls and phenolic acid hydrogels as mentioned in each figure legend. For comparisons between multiple groups, ANOVA with Tukey's post hoc was performed. Statistical significance was accepted as $p < 0.05$.

4.3   Results

4.3.1   Gel fraction and swelling ratio. Both polymer compositions had gel fractions above 96% indicating a complete reaction of a highly crosslinked polymer network, **Table 4.1**. In general, swelling ratios of PEG 4000 hydrogels were approximately double the initial dry weight, with swollen PEG 6000 hydrogels swelling more than 2.5 times their original dry weight.

4.3.2   Phenolic acid incorporation. Successful phenolic acid absorption was confirmed via the presence of characteristic peaks corresponding to phenolic rings of CA, pCA, and Caff in the FTIR spectra (C=C at ~1650 cm^{-1}, C-C at ~1509 cm^{-1}, and =C-H at ~1216 cm^{-1}), which are not visible in the control PEG hydrogels. Representative spectra of PEG 4000 hydrogels are shown in **Figure 4.2a-c**; similar observations were made in the PEG 6000 spectra before and after phenolic acid incorporation. Physical absorption of phenolic acids from the 10% solutions was statistically higher compared to the respective 5% solutions, **Figure 4.2d**. A general increase in phenolic acid absorption was also observed with increased PEG molecular weight in PEG 6000 hydrogels.
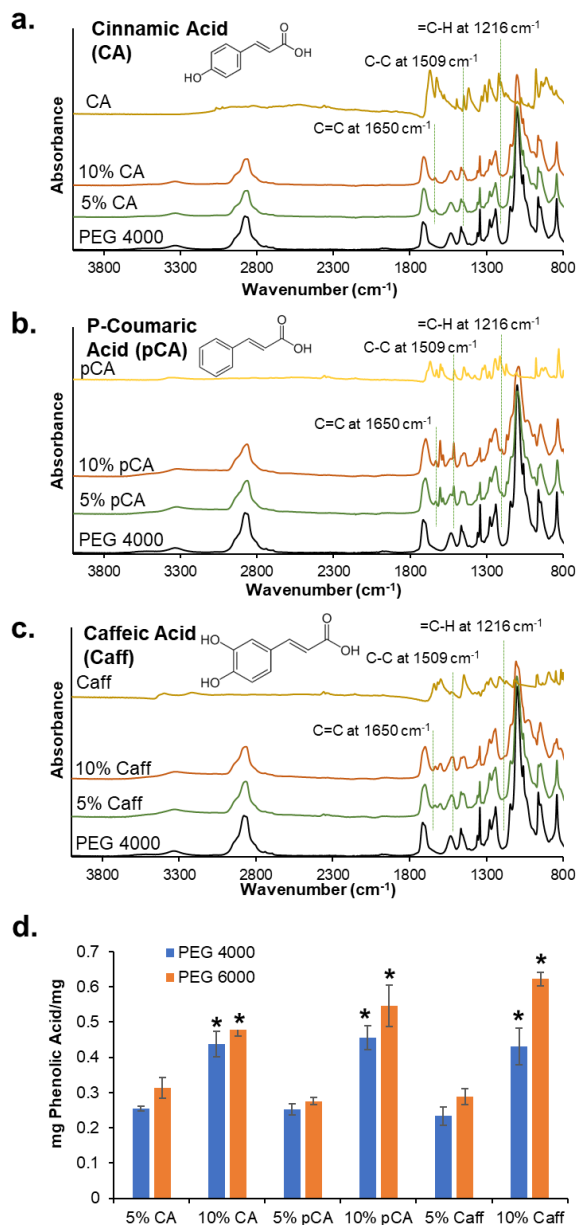
Figure 4.2 Fourier transform infrared spectroscopy of PEG 4000 hydrogel samples before and after physical incorporation of (a) cinnamic acid, (b) p-coumaric acid, and (c) caffeic acid. (d) Phenolic acid loading in PEG 4000 and PEG 6000 hydrogels. Mean ± standard deviation displayed. n = 3. *$p < 0.05$ between formulations under brackets.

4.3.3 **Mechanical properties**. Compressive modulus was measured on foams with 70% porosity (described in **section 4.2.2**) before and after phenolic acid incorporation, **Figure 4.3**. Overall, compressive modulus values range from 88 kPa to 148 kPa for PEG 4000-based hydrogels and from 46 kPa to 107 kPa for PEG 6000-based hydrogels. A general decrease in compressive modulus with increased CA content was observed, whereas pCA incorporation increased compressive modulus. Caff incorporation did not significantly alter the compressive modulus of PEG 4000 hydrogels, but an increase in compressive modulus is seen with increased Caff content in PEG 6000 hydrogels.
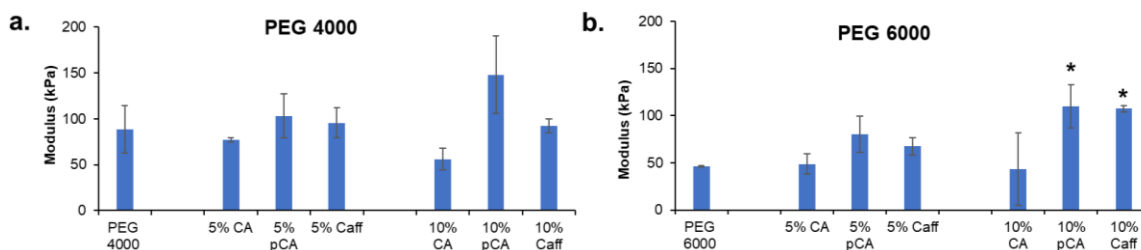
Figure 4.3 Compressive modulus of (a) PEG 4000 and (b) PEG 6000 hydrogels in the wet state before and after physical incorporation of phenolic acids. Mean ± standard deviation displayed. n = 3. *p<0.05 relative to PEG control without phenolic acid incorporation.

4.3.4 **Thermal properties**. All hydrogels had T_m's between 30 and 40°C, **Figure 4.4a-b**. Slight increases in T_m were observed after cinnamic acid incorporation in both formulations. An overall reduction in T_m occurs as the phenolic acid content increases from 5% to 10%, with larger variations in T_m observed in PEG 4000 hydrogels compared to PEG 6000 hydrogels.

4.3.5 **Shape memory properties**. Dynamic mechanical analysis was used to measure the shape memory properties of hydrogel networks, **Figure 4.4c-f**. Shape fixity and recovery of PEG 4000 controls were high (>92%) and were slightly increased after 5% phenolic acid incorporation. Higher phenolic acid content PEG 4000 hydrogels displayed a general

reduction in shape fixity and shape recovery, with larger differences observed in 10% pCA and 10% Caff hydrogels. Shape fixity was high (~90%) for all PEG 6000 hydrogels, and phenolic acid incorporation increased fixity, with minimal variations based on phenolic acid content or type. PEG 6000 control hydrogels had relatively low shape recovery (57%), which was increased to >80% after phenolic acid incorporation at low and high concentrations.
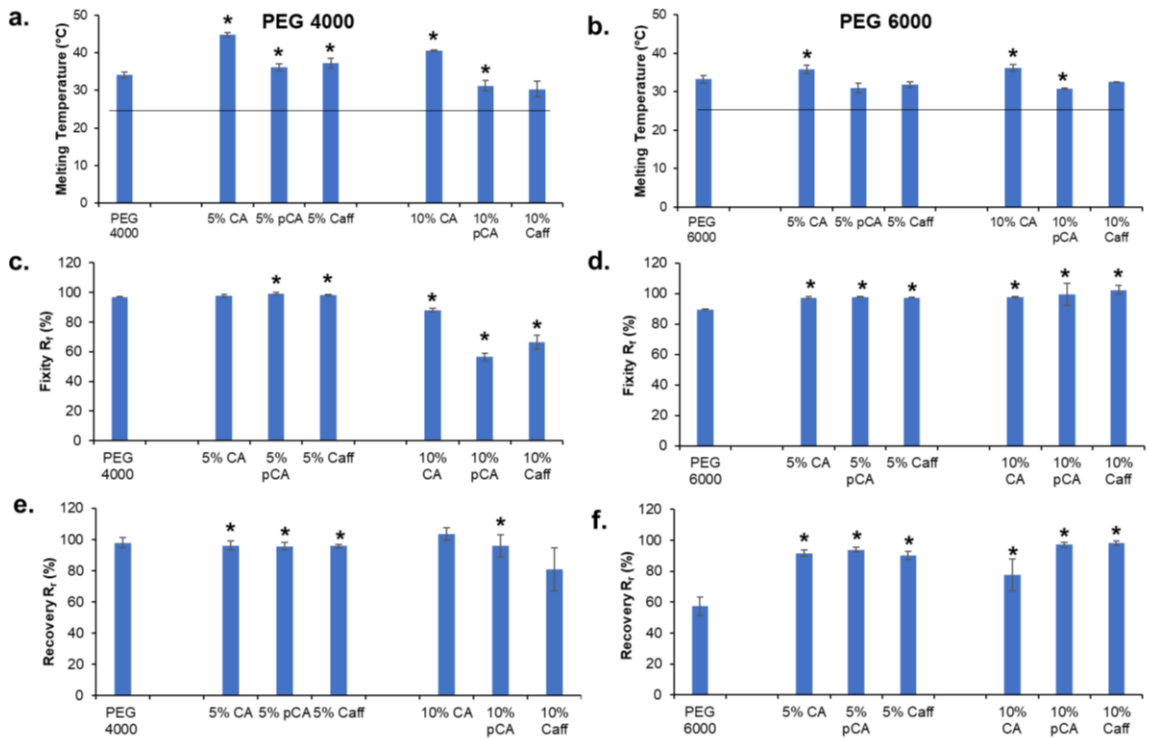
Figure 4.4 Melting temperatures of (a) PEG 4000 and (b) PEG 6000 hydrogels before and after phenolic acid incorporation were measured using differential scanning calorimetry. The horizontal lines denote room temperature to indicate potential for shape fixity during storage. Shape memory properties (fixity: (c-d) and recovery: (e-f)) of (c) and (e) PEG 4000 and (d) and (f) PEG 6000 hydrogels before and after phenolic acid incorporation measured using dynamic mechanical analysis. *$p<0.05$ relative to PEG control without phenolic acid incorporation.

4.3.6 **Antimicrobial properties**. CA hydrogels had initially high antimicrobial properties, as evidenced by low CFU counts at 0 days of incubation in PBS, **Figure 4.5**. Antimicrobial properties were quickly diminished by 10 days, when high numbers of CFUs were present. CFU density generally increased over 20-30 days of CA hydrogel incubation in PBS. The pCA and Caff hydrogels had excellent antimicrobial properties on days 0 and 10, with 6minimal CFUs present, **Figure 4.6**. The 10% pCA and Caff hydrogels retained antimicrobial properties at 20 days, whereas an increase in CFUs was observed in the 5% pCA and Caff hydrogels. By 30 days, all hydrogels had minimal antimicrobial properties. Upon analyzing the antimicrobial properties of the surrounding PBS solutions, it was observed that CA hydrogel solutions had negligible CFUs at 10 days. CFU densities were generally high in PBS surrounding CA hydrogels after 20 and 30 days, indicating that the majority of CA was released within 10 days, **Figure 6**. PBS from the other hydrogels at 10 days did not inhibit CFU formation. There was a slight reduction in CFUs observed in PBS surrounding pCA and Caff hydrogels at 20 days. An increase in CFUs was observed at 30 days in all hydrogel solutions. No clear trends were observed between the antimicrobial properties of corollary PEG 4000 and PEG 6000 formulations.
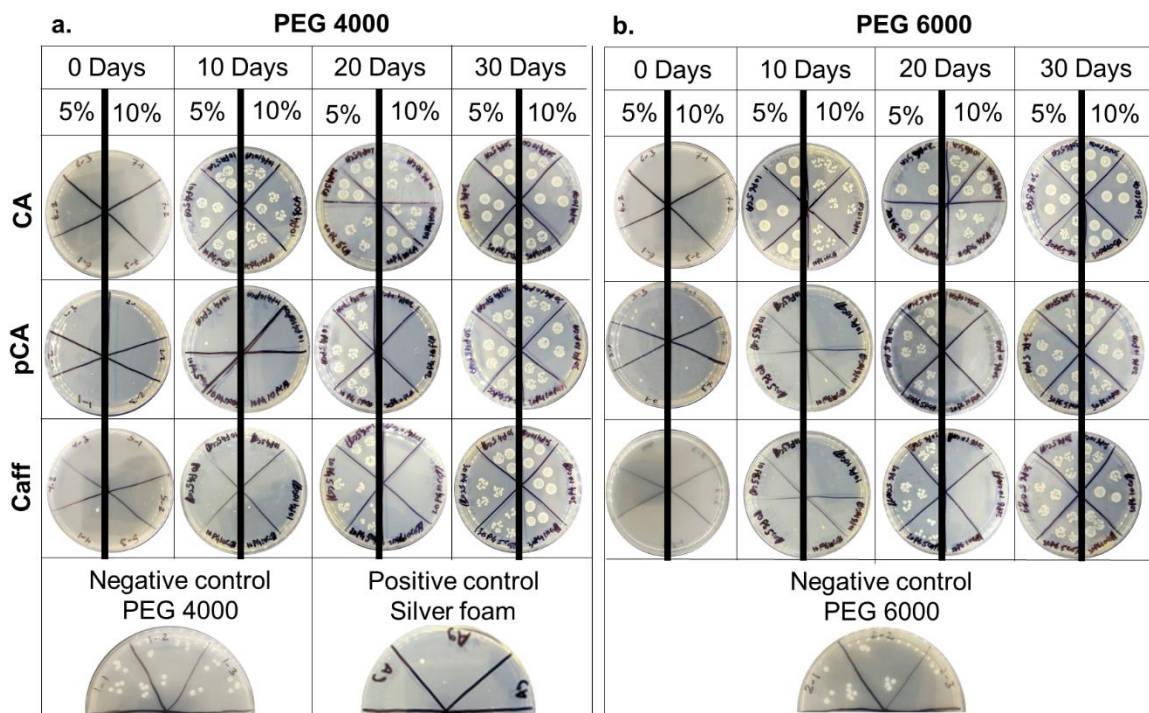
Figure 4.5 Antimicrobial properties of (a) PEG 4000 and (b) PEG 6000 hydrogels before and after physical incorporation of phenolic acids over 30 days of storage in phosphate-buffered saline. The left side denotes 5% and the right side denotes 10% phenolic acid incorporated into the respective hydrogel controls, shown in the lowest row. Images of colony forming units are displayed.
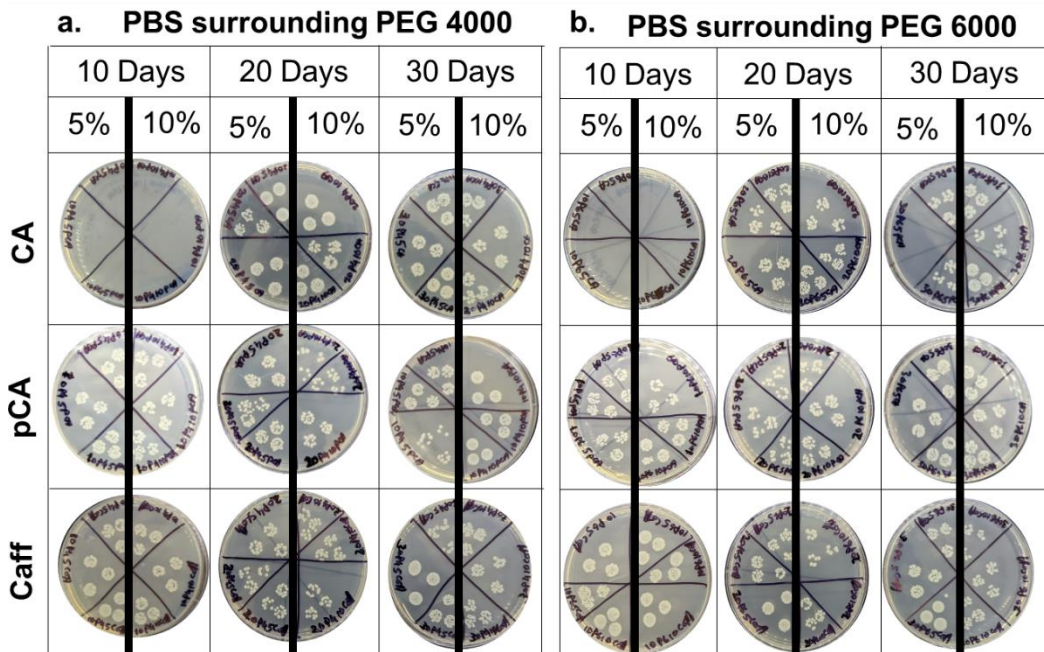
Figure 4.6 Antimicrobial properties of surrounding PBS solutions in which phenolic acid-containing (a) PEG 4000 and (b) PEG 6000 hydrogels were incubated. Solutions were tested at 10, 20, and 30 days. Images of colony forming units are displayed.

4.3.7 **Phenolic acid release.** As seen in **Figure 4.7**, an initial release was observed during the first 10 days across all hydrogel formulations. Between 10 and 20 days, the phenolic acid release was slower compared to the first 10 days, and minimal additional release was observed between 20 and 30 days. Overall, increased phenolic acid release was observed amongst hydrogels with higher phenolic acid content (10% vs. 5%) and higher PEG molecular weight (PEG 6000 vs. PEG 4000). Additionally, as the number of ring hydroxyls was increased on the phenolic acids (CA < pCA < Caff), lower release rates were observed.

4.3.8 **Cytocompatibility**. Control hydrogels had high cytocompatibility (>90%) over 24 hours, **Figure 4.8**. In general, cytocompatibility was reduced with an increase in phenolic acid content from 5% to 10%. The overall cytocompatibility of CA and pCA hydrogels was

maintained above the ISO – 10993 standards (>75% cytocompatibility).[27] However, Caff hydrogels had lower cytocompatibility below 75%, with larger reductions in cytocompatibility (<50%) observed in hydrogels with 10% Caff content. When tested over one week period, both CA, (**Figure 4.8c**) and pCA, (**Figure 4.8d**) containing hydrogels exhibited satisfactory cytocompatibility.
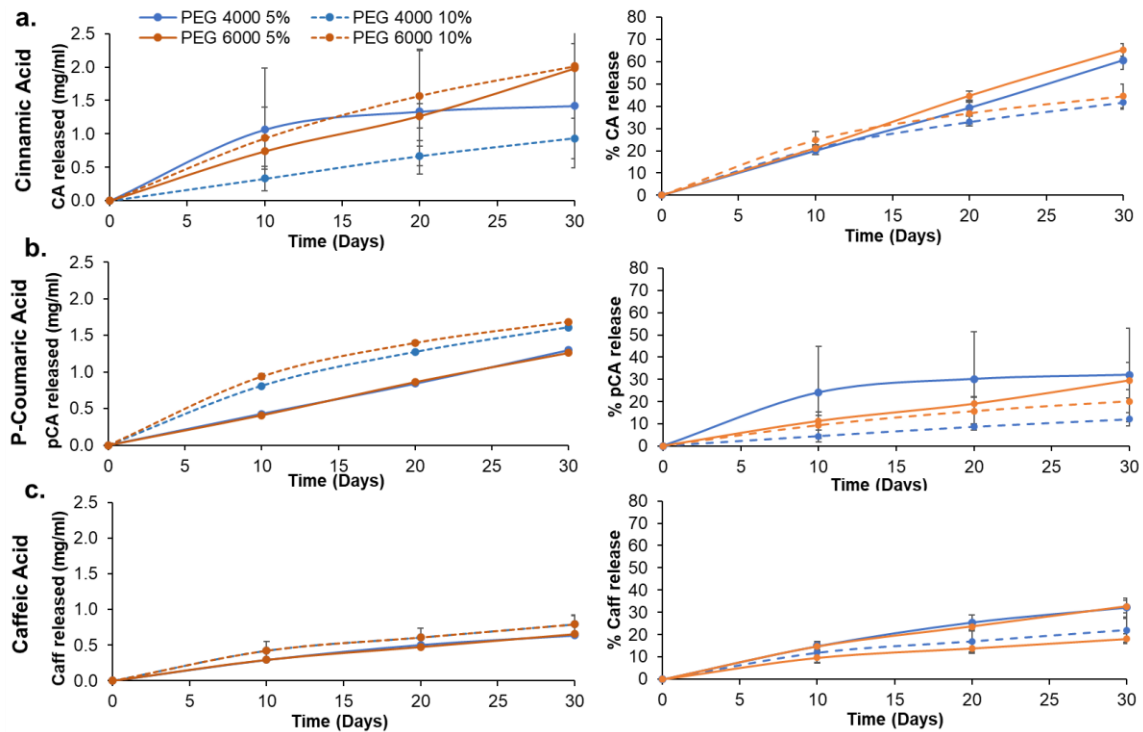
Figure 4.7 Quantification of (a) Cinnamic Acid, (b) p-Coumaric Acid, and (c) Caffeic Acid released from the hydrogel networks over 30 days measured using UV-vis spectroscopy. Quantifications are provided in mg phenolic acid/ml of PBS (left column) and percent release relative to initial incorporation (right column). Mean ± standard deviation displayed. n = 3. Legend in top left applies to all charts.
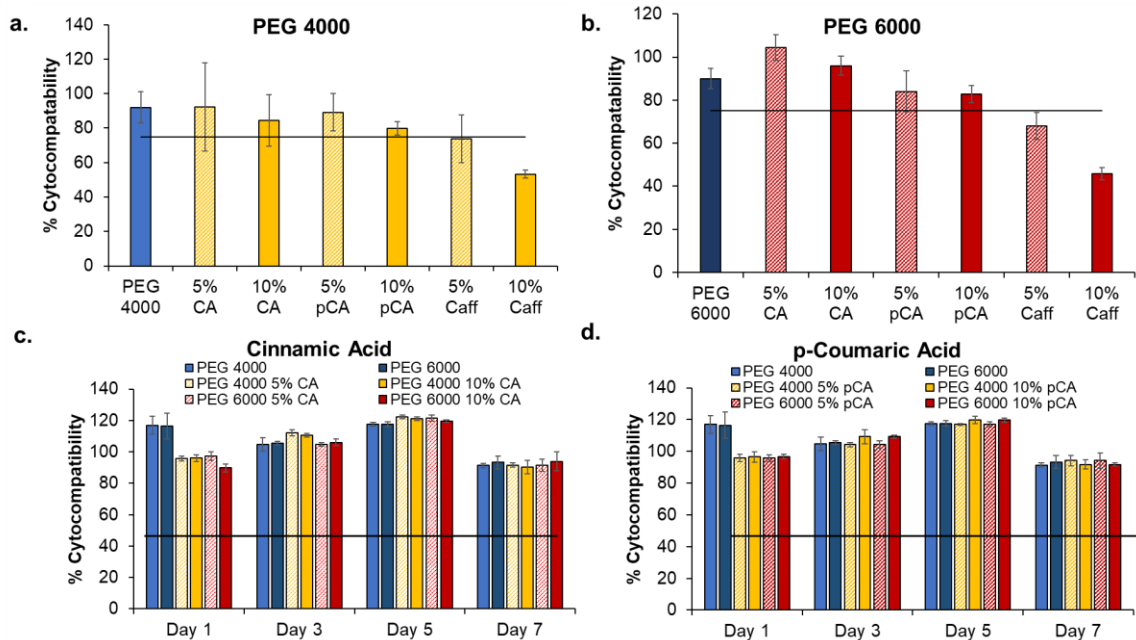
Figure 4.8 Cytocompatibility of 3T3 mouse fibroblast cells over 24 hours in the presence of (a) PEG 4000 and (b) PEG 6000 hydrogels before and after the physical incorporation of phenolic acids. Cytocompatibility of 3T3 mouse fibroblasts over 1 week in the presence of (c) Cinnamic Acid and (d) p-Coumaric Acid containing hydrogels. Mean ± standard deviation displayed. n = 3. The horizontal line denotes the ISO standard (75% cytocompatibility). No statistical significance observed amongst samples over one week within the same group.

4.3.9 Volume Recovery of Foams. Upon identification of hydrogels that had antimicrobial properties and cytocompatibility, volume recovery of radially crimped foams was characterized in 37°C water as an initial indication of foam dressing expansion in the body, **Figure 4.9**. Incorporating phenolic acids resulted in a faster volume recovery in both PEG 4000 and PEG 6000 foams. PEG 4000 foams generally had slower expansion, with controls reaching maximum volume recovery at ~6 minutes, **Figure 4.9a**. Inclusion of 10% CA and

10% pCA increased PEG 4000 volume expansion rates to reach a maximum volume within ~4 minutes. PEG 6000 control foams recovered very rapidly and took ~30 seconds to recover 100% of their original volume. PEG 6000 foams with 10% CA and 10% pCA recovered 100% of their original volume within 5 to 15 seconds, as seen in **Figure 4.9b**.
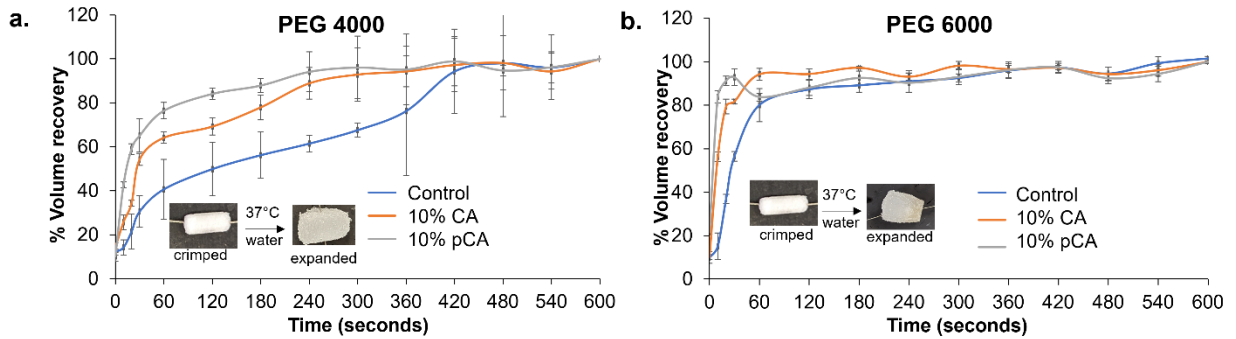
Figure 4.9 Volume recovery of (a) PEG 4000 and (b) PEG 6000 control foams compared with foams with cinnamic acid and p-coumaric acid. Mean ± standard deviation displayed. n = 3.

4.4 Discussion

This work describes a new shape memory polymer hydrogel system. We demonstrate the capability to simultaneously improve shape memory properties and impart antimicrobial capabilities to a polymer network post-fabrication. This modification approach can be applied to any polymer system that has the potential to form hydrogen bonds with phenolic acids to enable physical incorporation into the network. Furthermore, the system could be employed with other small molecule drugs of interest that contain hydrogen bonding sites.

The increased swelling ratio amongst the PEG 6000 hydrogels can be attributed to a longer polymer chain length, which results in relatively lower crosslink density and increased water absorption.[20] The increased swelling ratio in PEG 6000 hydrogels correlated with increased phenolic acid absorption. This result was expected, as the phenolic acids get absorbed onto the hydrogels via diffusion during swelling. It is hypothesized that phenolic acids are stabilized by hydrogen bonding between the urethane groups within the polymer network and the hydroxyl groups on the phenolic acids (i.e., carboxylic acid end groups of all three phenolic acids and hydroxyls on phenolic rings of pCA and Caff).

The reported elastic modulus of skin is between 420 kPa and 850 kPa;[28], [29] an overall compressive modulus of the SMP hydrogels below 150 kPa ensures that hydrogel wound dressings would not impart excessive stress to the surrounding wound walls post-swelling. The lower compressive modulus of PEG 6000 hydrogels can be attributed to a longer monomer length that results in a lower crosslink density.[30] These mechanical property measurements were taken on water-swollen hydrogels, in which the hydrogen bonds between urethane groups in the polymer network are plasticized.[31] A general increase in compressive modulus after the physical incorporation of phenolic acids, particularly in the PEG 6000 hydrogels, is attributed to hydrogen

130

bonds between phenolic acids and the polymer network to increase physical cross-linking. Therefore, phenolic acid incorporation provides a simple tool for tuning hydrogel modulus independently of network chemistry. While the focus of this work was not on finely tuning scaffold stiffness, this concept could be applied to any biomaterial system with hydrogen bonding sites as a new method for altering modulus.

The new intermolecular hydrogen bonds formed between the hydroxyl and urethane groups disrupt the regular hydrogen bonds of the polyurethane network, which can alter the melting temperatures. The changes in melting temperature were larger in the PEG 4000 hydrogels, which we hypothesize is due to the shorter PEG chains that cannot form crystals as readily.[20] In these gels, small amounts of phenolic acids acted as crosslinkers between chains, increasing crystal stability and corollary T_m's. Higher concentrations of phenolic acids with multiple hydrogen bonding sites (pCA and Caff) had the opposite effect and reduced T_m; in these hydrogels, the phenolic acids act more like plasticizers, separating polymer chains and reducing crystal stability. Similar trends can be seen in the PEG 6000 hydrogels, but the overall effects of phenolic acids on T_m were reduced in the PEG 6000 formulations.

The synthesized polyurethane hydrogels demonstrate shape memory properties around their T_m. All measured T_m's were above room temperature, and shape fixity was high across all formulations. In general, trends in shape fixity and recovery of PEG 4000 hydrogels after phenolic acid incorporation matched trends in T_m, with increased shape memory properties after incorporation of low amounts of phenolic acids and reductions in shape memory properties in hydrogels with higher concentrations of pCA and Caff. PEG 6000 hydrogels all exhibited increases in shape fixity and recovery after phenolic acid incorporation, with larger increases observed with higher numbers of hydrogen bonding sites on the phenolic acids. This result indicates that phenolic

acids act more like crosslinkers in the PEG 6000 hydrogels, stabilizing the temporary shape and enabling faster and more complete recovery to the primary shape.

This system provides a novel mechanism for tuning thermal and shape memory properties of polymer networks that could be applied to a range of shape memory polymers. Higher thermal transitions and shape fixity enables fixation and storage in the temporary shape at room temperature without premature recovery before implantation. Improvements in shape recovery would enable expansion to the permanent shape after implantation to fill wounds with dressing materials. When these materials are exposed to water, hydrogen bonds that stabilize the secondary shapes are plasticized to soften the hydrogel and enable shape recovery at lower temperatures. This effect was seen in **Figure 4.9**, where hydrogel foams expanded to their primary shape in 37°C water. Furthermore, 10% CA and 10% pCA foams had a faster volume recovery due to the plasticization of urethane linkages by the phenolic acids. These shape recovery properties could be harnessed for wound filling in future work. Dry, compressed hydrogels could be applied to wound beds, where they would expand after heating to body temperature to fill irregular wound shapes. Then, the hydrogels would swell to maintain a moist wound environment. Then, the hydrogels would swell to maintain a moist wound environment.

All phenolic acid hydrogels had initially high antimicrobial properties with minimal CFUs compared with negative controls. Retention of antimicrobial properties over time of incubation in PBS was dependent on the number of hydrogen bonding between phenolic acids and the polyurethane hydrogel network. Namely, more rapid loss of antimicrobial properties in CA hydrogels can be attributed to the absence of free hydroxyls on the phenolic ring of CA, which limits strong intermolecular bonding with the polymer network and allows CA to be more easily

released. These release results were corroborated by the high antimicrobial properties of surrounding PBS at 10 days and the relatively large amount of CA released in this time frame.

Hydrogels with pCA and Caff better retained antimicrobial properties, particularly in higher phenolic acid content samples; negligible CFUs were observed in 10% pCA and Caff hydrogels at 20 days, while 5% pCA and Caff hydrogels had significantly more CFUs at 20 days in comparison with corollary 10% samples. By 30 days, CFU counts were high after incubation with all hydrogels, indicating that the concentration of phenolic acids remaining in the hydrogels at this time point was not sufficient for imparting antimicrobial efficacy to the hydrogels.

At 10 days, the pCA and Caff solutions had high CFU densities. It is hypothesized that the amount of pCA and Caff released in the first 10 days was too low to affect the antimicrobial properties of the surrounding solutions. On day 20, there are slightly lower densities of CFUs amongst the pCA and Caff solutions compared to the day 10 results, indicating that the amount of pCa and Caff released between 10 and 20 days imparted surrounding media with antimicrobial properties. The phenolic acid release slowed after 20 days, and thus minimal release occurred between days 20 and 30. A high density of CFUs was observed after incubation of bacteria with surrounding PBS on day 30. The IC50 values for CA, pCA, and Caff against *E. coli* at 24 hours were previously measured to be 2 to 3 mg/ml. [32] The negative controls have an average of 13 CFUs. At a 10^6 dilution level, the net CFU/ml during *in vitro* testing can thereby be estimated at 13×10^6. This is comparable to the average CFU/ml found in a typical chronic wound as shown by Bowler et al [33], thus indicating that hydrogels with 10% pCA have potential to inhibit bacterial growth in an infected chronic wound. The net amount of phenolic acid release between 20 and 30 days was below this IC50 value, substantiating the observed increases in CFU formation at 30 days. It is also possible that the phenolic acids were not stable within this time frame and that they

experienced a loss in antimicrobial activity over time to reduce effects on surrounding media. This point warrants further investigation in future work.

In general, pCA and Caff had slower release profiles, which is attributed to their higher number of hydrogen bonding sites. These release results provide a rational framework for the selection of phenolic acids based on the number of hydrogen bonding sites. If an earlier release is desired, phenolic acids with fewer intermolecular interaction sites (e.g., CA) should be selected, while phenolic acids with more hydroxyl groups (e.g., pCA and Caff) would be preferred for long-term antimicrobial properties.

The high cytocompatibility of CA and pCA hydrogels provides a preliminary indication that these materials could serve as wound dressing materials. The low cytocompatibility of Caff hydrogels echoes previously obtained results wherein the cytocompatibility of Caff solutions dropped significantly over 24 hours.[25] Caff is known to inhibit genes via functional interactions with MCF-7 human breast cancer cells that exhibited very low cytotoxicity[34]. Thus, Caff may not be an ideal candidate for use in wound dressings. In our previous work, the silver dressing that was used as a positive control in the antimicrobial testing had very low cytocompatibility (30%).[35] Thus, CA and pCA provide options for the addition of antimicrobial properties into hydrogels to reduce infection risks without affecting surrounding mammalian cells.

Apart from the observed improvements in shape memory and antimicrobial properties, phenolic acids also have several other functionalities that may be beneficial in wound healing. For example, phenolic acids are antioxidants that can scavenge reactive oxygen species (ROS) by inhibiting ROS-generating enzymes and chelation with ROS-forming ferrous (Fe^{2+}) ions.[36] The reduction of ROS could aid the chronic wound healing process and reduce chronic inflammation that is caused by excessive ROS.[37]–[39] In general, these hydrogels provide a promising platform for

future development as chronic wound dressing materials. Additionally, this work provides novel

methods to tune hydrogel properties without changing the overall network chemistry.

4.5 Conclusions

This study presents a simple technique to tune polymer structures independently of overall network chemistry, impart easy-to-control antimicrobial properties, and improve shape memory properties post-fabrication. The number of hydroxyl groups present in the incorporated phenolic acids influences the extent to which the material properties can be tuned (i.e., whether incorporated phenolic acids act more as crosslinkers or plasticizers). These considerations could be applied to the incorporation of other drugs/bioactive agents into biomaterials via hydrogen bonding to control release while tuning material properties. The polymer molecular weight also affected the extent to which the properties could be altered, providing an additional level of control. These hydrogel materials have appropriate thermal properties to enable stable storage in the low-profile shape and fast actuation after implantation to rapidly fill wounds. Improved shape recovery after phenolic acid incorporation could ensure that wounds are completely sealed. Increased phenolic acid content and intermolecular interaction sites allowed for longer antimicrobial property retention, providing a framework for the selection of phenolic acids based on desired antimicrobial time frames. Finally, appropriate cytocompatibility indicates that these hydrogels may be suitable for future development as chronic wound dressings that reduce infection risks. Based on the data collected here, PEG 6000 hydrogels with 10% pCA has the best potential for use for chronic wound treatment due to their favorable shape memory properties, cytocompatibility, and sustained antimicrobial efficacy.

4.6 References

[1] K. Järbrink *et al.*, "The humanistic and economic burden of chronic wounds: a protocol for a systematic review," *Syst. Rev.*, vol. 6, no. 1, Jan. 2017.

[2] G. S. Schultz *et al.*, "Wound bed preparation: a systematic approach to wound management," *Wound Repair Regen.*, vol. 11 Suppl 1, no. SUPPL. 1, Mar. 2003.

[3] G. A. Bray, "Chronic wound care," *www.thelancet.com*, vol. 372, 2008.

[4] "Chronic Wound Care Market Size, Share | Global Industry Trends [2027]." [Online]. Available: https://www.fortunebusinessinsights.com/industry-reports/chronic-wound-care-market-100222. [Accessed: 15-Mar-2022].

[5] T. G. D. Pemayun, R. M. Naibaho, D. Novitasari, N. Amin, and T. T. Minuljo, "Risk factors for lower extremity amputation in patients with diabetic foot ulcers: a hospital-based case–control study," *Diabet. Foot Ankle*, vol. 6, no. 1, p. 29629, Jan. 2015.

[6] S. P. Holmes, S. Rivera, P. B. Hooper, J. E. Slaven, and S. K. T. Que, "Hydrocolloid dressing versus conventional wound care after dermatologic surgery," *JAAD Int.*, vol. 6, pp. 37–42, Mar. 2022.

[7] Q. Chai, Y. Jiao, and X. Yu, "Hydrogels for biomedical applications: Their characteristics and the mechanisms behind them," *Gels*, vol. 3, no. 1, 2017.

[8] E. Lih, J. S. Lee, K. M. Park, and K. D. Park, "Rapidly curable chitosan-PEG hydrogels as tissue adhesives for hemostasis and wound healing," *Acta Biomater.*, vol. 8, no. 9, pp. 3261–3269, 2012.

[9] J. Koehler, F. P. Brandl, and A. M. Goepferich, "Hydrogel wound dressings for bioactive treatment of acute and chronic wounds," *Eur. Polym. J.*, vol. 100, no. August 2017, pp. 1–11, 2018.

[10] H. Gholizadeh *et al.*, "Application of a Thermosensitive In Situ Gel of Chitosan-Based Nasal Spray Loaded with Tranexamic Acid for Localised Treatment of Nasal Wounds," *AAPS PharmSciTech*, vol. 20, no. 7, pp. 1–12, Oct. 2019.

[11] M. Mattioli-Belmonte *et al.*, "Chitin Nanofibrils Linked to Chitosan Glycolate as Spray, Gel, and Gauze Preparations for Wound Repair:," *http://dx.doi.org/10.1177/0883911507082157*, vol. 22, no. 5, pp. 525–538, Jul. 2016.

[12] J. K. Li, N. Wang, and X. S. Wu, "Poly(vinyl alcohol) nanoparticles prepared by freezing–thawing process for protein/peptide drug delivery," *J. Control. Release*, vol. 56, no. 1–3, pp. 117–126, Dec. 1998.

[13] L. Deng, H. Lu, C. Tu, T. Zhou, W. Cao, and C. Gao, "A tough synthetic hydrogel with excellent post-loading of drugs for promoting the healing of infected wounds in vivo," *Mater. Sci. Eng. C*, p. 112577, Nov. 2021.

[14] B. Shriky *et al.*, "Pluronic F127 thermosensitive injectable smart hydrogels for controlled drug delivery system development," *J. Colloid Interface Sci.*, vol. 565, pp. 119–130, 2020.

[15] H. Madry *et al.*, "Thermosensitive Hydrogel Based on PEO–PPO–PEO Poloxamers for a Controlled In Situ Release of Recombinant Adeno-Associated Viral Vectors for Effective Gene Therapy of Cartilage Defects," *Advanced Materials*, vol. 32, no. 2. 2020.

[16] D. Trung Nguyen *et al.*, "Dual Interactions of Amphiphilic Gelatin Copolymer and Nanocurcumin Improving the Delivery Efficiency of the Nanogels," *Polymers (Basel).*, vol. 11, p. 814, 2019.

[17] A. U. Vakil *et al.*, "Shape Memory Polymer Foams with Tunable Degradation Profiles," *ACS Appl. bio Mater.*, vol. 4, no. 9, pp. 6769–6779, Aug. 2021.

[18] P. Singhal, W. Small, E. Cosgriff-Hernandez, D. J. Maitland, and T. S. Wilson, "Low

density biodegradable shape memory polyurethane foams for embolic biomedical applications," *Acta Biomater.*, vol. 10, no. 1, pp. 67–76, Jan. 2014.

[19] S. M. Hasan, L. D. Nash, and D. J. Maitland, "Porous shape memory polymers: Design and applications," *J. Polym. Sci. Part B Polym. Phys.*, vol. 54, no. 14, pp. 1300–1318, 2016.

[20] J. P. E. Junker, R. A. Kamel, E. J. Caterson, and E. Eriksson, "Clinical Impact Upon Wound Healing and Inflammation in Moist, Wet, and Dry Environments," *Adv. Wound Care*, vol. 2, no. 7, pp. 348–356, Sep. 2013.

[21] S. Lowe, N. M. O'Brien-Simpson, and L. A. Connal, "Antibiofouling polymer interfaces: Poly(ethylene glycol) and other promising candidates," *Polym. Chem.*, vol. 6, no. 2, pp. 198–212, 2015.

[22] G. G. F. Nascimento, J. Locatelli, P. C. Freitas, and G. L. Silva, "Antibacterial activity of plant extracts and phytochemicals on antibiotic-resistant bacteria ," *Brazilian Journal of Microbiology* , vol. 31. scielo , pp. 247–256, 2000.

[23] M. B. B. Monroe, A. D. Easley, K. Grant, G. K. Fletcher, C. Boyer, and D. J. Maitland, "Multifunctional shape memory polymer foams with bio-inspired antimicrobials," *ChemPhysChem*, vol. 19, no. 16, pp. 1999–2008, Aug. 2018.

[24] H. Dietrich and M. S. Pour Nikfardjam, "Influence of Phenolic Compounds and Tannins on Wine-Related Microorganisms," in *Biology of Microorganisms on Grapes, in Must and in Wine*, H. König, G. Unden, and J. Fröhlich, Eds. Cham: Springer International Publishing, 2017, pp. 421–454.

[25] J. Liu, C. Du, H. T. Beaman, and M. B. B. Monroe, "Characterization of phenolic acid antimicrobial and antioxidant structure–property relationships," *Pharmaceutics*, vol. 12,

no. 5, p. 419, May 2020.

[26] B. Herigstad, M. Hamilton, and J. Heersink, "How to optimize the drop plate method for enumerating bacteria," *J. Microbiol. Methods*, vol. 44, no. 2, pp. 121–129, Mar. 2001.

[27] P. ISO, "ISO 10993-5:2009 Biological evaluation of medical devices -- Part 5: Tests for in vitro cytotoxicity," *International Organization for Standardization, Geneva*. p. 34, 2009.

[28] C. Pailler-Mattei, S. Bec, and H. Zahouani, "In vivo measurements of the elastic mechanical properties of human skin by indentation tests," *Med. Eng. Phys.*, vol. 30, no. 5, pp. 599–606, Jun. 2008.

[29] P. G. Agache, C. Monneur, J. L. Leveque, and J. De Rigal, "Mechanical properties and Young's modulus of human skin in vivo," *Arch. Dermatol. Res.*, vol. 269, no. 3, pp. 221–232, Dec. 1980.

[30] S. Lee, X. Tong, and F. Yang, "The effects of varying poly(ethylene glycol) hydrogel crosslinking density and the crosslinking mechanism on protein accumulation in three-dimensional hydrogels," *Acta Biomater.*, vol. 10, no. 10, pp. 4167–4174, 2014.

[31] T. Pretsch, I. Jakob, and W. Müller, "Hydrolytic degradation and functional stability of a segmented shape memory poly(ester urethane)," *Polym. Degrad. Stab.*, vol. 94, no. 1, pp. 61–73, Jan. 2009.

[32] J. Liu, C. Du, H. T. Beaman, and M. B. B. Monroe, "Characterization of Phenolic Acid Antimicrobial and Antioxidant Structure – Property Relationships," *Pharmaceutics*, vol. 12, no. 5, p. 419, 2020.

[33] P. G. Bowler, B. I. Duerden, and D. G. Armstrong, "Wound Microbiology and Associated Approaches to Wound Management," *Clin. Microbiol. Rev.*, vol. 14, no. 2, pp. 244–269, Apr. 2001.

[34] H. Rezaei-Seresht, H. Cheshomi, F. Falanji, F. Movahedi-Motlagh, M. Hashemian, and E. Mireskandari, "Cytotoxic activity of caffeic acid and gallic acid against MCF-7 human breast cancer cells: An in silico and in vitro study," *Avicenna J. Phytomedicine*, vol. 9, no. 6, p. 574, 2019.

[35] C. Du, J. Liu, D. A. Fikhman, K. S. Dong, and M. B. B. Monroe, "Shape Memory Polymer Foams With Phenolic Acid-Based Antioxidant and Antimicrobial Properties for Traumatic Wound Healing," *Front. Bioeng. Biotechnol.*, vol. 10, Feb. 2022.

[36] N. R. Perron and J. L. Brumaghim, "A review of the antioxidant mechanisms of polyphenol compounds related to iron binding," *Cell Biochem. Biophys.*, vol. 53, no. 2, pp. 75–100, Mar. 2009.

[37] C. Dunnill *et al.*, "Reactive oxygen species (ROS) and wound healing: the functional role of ROS and emerging ROS-modulating technologies for augmentation of the healing process.," *Int. Wound J.*, vol. 14, no. 1, pp. 89–96, Feb. 2017.

[38] N. Bryan, H. Ahswin, N. Smart, Y. Bayon, S. Wohlert, and J. A. Hunt, "Reactive oxygen species (ROS) - a family of fate deciding molecules pivotal in constructive inflammation and wound healing," *Eur. Cells Mater.*, vol. 24, pp. 249–265, 2012.

[39] T. Hussain, B. Tan, Y. Yin, F. Blachier, M. C. B. Tossou, and N. Rahu, "Oxidative Stress and Inflammation: What Polyphenols Can Do for Us?," *Oxid. Med. Cell. Longev.*, vol. 2016, 2016.

Chapter V

Conclusions and Future Work

This dissertation focused on developing novel polyurethane-based shape memory polymer scaffolds for multiple biomedical applications. Material fabrication was altered based on the intended application. Thermo-mechanical properties were assessed to confirm that the materials meet the required criteria for implantation. Cytocompatibility of materials was evaluated to confirm the materials are safe to use for their intended biomedical applications.

5.1 Biodegradable gas-blown foams for tissue scaffolds

In this project, biodegradable gas-blown foams were synthesized for tissue engineering applications. The degradation rate was tuned by altering the number of degradable linkages and the mechanisms by which the material undergoes degradation. Volume recovery and shape memory properties were altered based on the thermal properties and pore sizes of the resulting foams. To ensure that the foams can maintain their secondary shape under ambient conditions, thermal properties were tuned to obtain a minimum T_g above 40°C by increasing the crosslinking in the polymer network. Pore size was tuned by changing the pre-mix viscosity and balancing the gelling and blowing catalysts to achieve an average pore size of 1000 µm. This pore size ensures appropriate nutrient transfer and aids in the volume recovery process. All foams demonstrated rapid volume recovery within 5 minutes. Rapid expansion from the compressed secondary to the primary shape ensures the foams can seal the wound opening and thereby aid hemorrhage control. Multiple foam formulations (Appendix A and B) were prepared apart from the ones shown in Chapter II to understand the effect of ester and ether content on the overall *in vitro* oxidative degradability of foams in a 3% H_2O_2 solution.

Upon comparing degradation profiles *in vivo*, it was observed that the degradation rates should be increased further to ensure that foams undergo complete degradation within 8 to 12 weeks to match wound healing rates. In future work, this can be achieved by either increasing the number of ester

linkages or incorporating additional degradable linkages to accelerate ester hydrolysis, such as dithiols. Added care must be taken to ensure the transition temperature does not drop at the expense of increasing degradability.

This work provides a framework that can be used as a guide to tuning degradation rates and mechanisms. Degradation rates of thermoset polyurethanes can be increased by incorporating hydrolytically degradable ester linkages and can be slowed down by incorporating ether linkages. The ester and ether-containing foams allow for surface erosion that is beneficial to maintaining scaffold integrity during the degradation process, rather than undergoing bulk erosion as seen in the case of control foams. The shape fixity of these foams allows for use in irregular wound geometries, wherein the entry point of the wound might be smaller than the bulk interior of the wound. Additionally, this work brings forward an important point that predicting degradation rates is not straightforward and is highly dependent on the number of mechanisms through which biomaterial degrades. A single degradation medium is not suitable to predict the subcutaneous degradation rate of all formulations and an appropriate technique must be used for the required prediction.

5. 2 Thermoset and thermoplastic films with controlled drug release

Magnetic polymer composites were developed here to achieve on-demand drug delivery. These scaffolds could be used to administer a single drug at periodic, controlled intervals, or a dual composition scaffold could be used to deliver two drugs simultaneously at specified release rates. This system is particularly advantageous since drug release via remote actuation at the desired site could eliminate complications and inconveniences involved with an intravenous application.

The results obtained from this system could be further applied to hydrogels to improve our understanding of drug loading and release kinetics as an effect of the scaffold network. Drugs can also be loaded in microparticles within the polymers to finely tune release rates in future work. This would also help reduce heterogeneity in the polymer composites. Drug release should be monitored for longer periods in different media, such as 0.1M NaOH or 20% H_2O_2, to enable an understanding of the effects of accelerated hydrolytic and oxidative degradation, respectively, on release profiles as compared with those obtained using PBS.

This work demonstrates the ability to tune drug release profiles as required by altering the polymer composition and magnetic particle content. The polymer composites developed here can be used to load and administer any type of drug irrespective of their composition. This system can be utilized in applications wherein remote shape memory actuation or controlled shape change is desired over long-time frames such as mimicking tissue growth *in vitro*. This shape change can be controlled based on limiting the time for which the magnetic polymer composites are exposed to an alternating magnetic field. The shape change could also be controlled by incorporating magnetic particles in certain sections of a polymer wherein the desired shape change is required.

While this project uses nanoparticles prepared in situ in the interest of procurement costs, commercially available paramagnetic nanoparticles with a lower particle diameter could be used to increase the conductivity and thereby reduce required particle content to provide the same effects on shape recovery. Drug release patterns can also be tested *ex vivo* using pig skin to understand the healing capabilities of this drug-polymer composite.

Doxorubicin is known to lose its toxicity once it loses the attached sugar molecule. This effect could be tested by measuring the cytotoxicity of the surrounding media that contains the leached Dox over time.

Phosphorous containing dendrimers containing rhodamine derivatives that have a stable structure can be used as a chromophore to replace rhodamine B in future work as shown by Wei et al [1] to monitor release patterns over longer time periods (i.e. a month) for a more thorough understanding of the release kinetics.

Compared to traditional techniques to achieve on-demand drug delivery that utilize external triggers, such as ultrasound or electrical impulse, the use of shape memory properties in this system imparts a novel control mechanism for drug release. The shape memory effect can be utilized to alter the drug release rates from the same polymer composition by tuning the extent to which the polymer is deformed. Future studies could be done to study the difference in drug delivery rates based on changes in deformation. Increased amounts of elongation would require a longer time to recover the original shape. Furthermore, the use of shape memory to add control over drug release could be applied to any externally-triggered system to tune drug delivery over time.

5.2 Porous and non-porous hydrogels for infection control in chronic wounds

Here, hydrogels were prepared for the treatment of topical chronic wounds. Phenolic acids were physically incorporated into the hydrogel networks to impart antimicrobial properties and improve shape memory properties. Physical incorporation of phenolic acids via hydrogen bonding resulted in materials that retained antimicrobial properties over 20 days. The shape fixity ratio of PEG 6000 hydrogels was improved by 1.35 times after phenolic acid incorporation compared with that of control formulations, indicating that phenolic acids can be used to tune biological and shape memory properties simultaneously.

While these synthetic hydrogels may be beneficial for the treatment of topical chronic wounds, they could be modified for the treatment of internal wounds as well in future work. For example,

this system could be modified using techniques presented in Chapters 2 and 3 to impart degradability and incorporate chemotherapeutic drugs, such as 6-Mercaptopurine, to enable the use of these synthetic hydrogels for the treatment of Crohn's fistulas.

The key takeaways from this work include the ability to impart antimicrobial properties to any number of previously developed hydrogel systems by physically incorporating phenolic acids provided that hydrogen bonding sites are available. This approach avoids any additional chemical synthesis to impart desired antimicrobial effects. This work also demonstrates the ability to increase shape recovery without altering the chemical compositions of hydrogels, which could be useful for applications where volume recovery is needed.

In addition to the capabilities to impart antimicrobial properties, the shape memory property of these hydrogels can be utilized to deform the material as required prior to implantation into irregularly shaped wounds. For example, this could be used to treat bacterial infection in cylindrical topical wounds that have a narrow opening, but are deep where a traditional bandage cannot reach.

References

[1]   Y. Wei, R. Laurent, J.-P. Majoral, and A.-M. Caminade, "Synthesis and characterization of phosphorus-containing dendrimers bearing rhodamine derivatives as terminal groups," *Arkivoc*, vol. 2010, no. 10, pp. 318–327, Aug. 2010.

Appendix A

Shape Memory Polymer Foams with Tunable

Degradation Profiles*

A1. Introduction

Hemorrhage is the leading cause of potentially survivable death on the battlefield. Up to 90% of preventable deaths are due to uncontrolled bleeding, and approximately 20% of combat casualties result in death before the injured can be transported to a treatment facility.[1–3] The most common hemorrhage treatment includes the use of tourniquets and gauze coated with coagulants. However, gauze is often ineffective at promoting clotting, and improper or prolonged tourniquet use can lead to complications like nerve paralysis, limb ischemia, arrhythmias, and crush syndrome, which can result in amputation above the position of tourniquet.[4,5] This urgent clinical need has led to the recent development of new options for hemorrhage control. For example, XStat® is designed for bleeding control from junctional wounds.[6] XStat contains ~95 oxidized cellulose foams pieces that are injected into the wound using a syringe-like applicator, after which they expand and fill up the wound to apply pressure and induce clotting.[7] Each foam piece must be removed within 4 hours to prevent ischemia, and XStat exhibits a 22-fold increase in removal time compared with gauze.[6,8] This removal process can also lead to re-bleeds of surrounding tissues. Therefore, XStat may not be the best alternative to gauze in remote locations where access to a fixed care facility is limited.

To overcome limitations of current hemostatic dressing options, an ideal hemostatic material is biocompatible, promotes rapid blood clotting, and is degradable. A degradable hemostatic dressing could theoretically be left in place after application to degrade during healing, prolonging the time available to get a patient to a fixed facility and reducing re-bleed risks upon removal. To that end, He et al. prepared oxidized regenerated cellulose (ORC) gauze.[9] In a rabbit liver and ear-artery injury, this material induced hemostasis and degraded fully within 21 days; however, the gauze was forcibly removed by the blood flow from the artery, which reduces it applicability in

traumatic hemorrhage control. Dai et al. developed silver-exchanged calcium-doped mesoporous silica spheres for hemorrhage control.[10] The particles achieved hemostasis within 340 seconds and underwent a 40% weight loss over 42 days in vitro. However, these mesoporous particles have a recorded pore size of 3.2 nm, which is likely too small to facilitate tissue ingrowth.[11] Porous chitosan-based hemostatic microparticles were developed by Li et al.[12] The microspheres exhibit an increase in blood clotting with decreased surface pore size and a 40% weight loss over 4 weeks of lysozyme incubation, but have a pore size of <2 μm. Thus, these microparticles may not be suitable for deep wounds to aid tissue ingrowth.

To address this clinical need, shape memory polymer (SMP) foams are being investigated as hemostatic biomaterials.[13] SMPs are 'smart' stimuli-responsive materials that are synthesized in a primary, permanent shape; triggered using an external stimulus, such as heat or light; and strained/fixed into a temporary, secondary shape that is retained upon removal of the external stimulus. After re-exposure to the stimulus, SMPs regain their primary shape.[14] Heat is used as an external stimulus in this polyurethane SMP foam system, and shape change is designed around the polymer's glass transition temperature (T_g). These foams are biocompatible and capable of promoting rapid blood clotting due to their thrombogenic surface chemistry and high surface area.[15-16]

The shape memory properties allow SMP foam radial compression and storage in a low-profile, temporary geometry at temperatures below their T_g. Foam T_g's are reduced by exposure to water (relative to T_g in dry conditions) due to plasticization of the polymer network.[17] Therefore, SMP foams can be stored compressed at relatively high temperatures (~40-50°C) in the dry state. This smaller volume material can theoretically be packed into deep and/or irregularly-shaped wounds, which is particularly important in gunshot wounds, which often have small entry points

that expand outwards into large internal wound cavities.[18] Once exposed to water present in the blood at body temperature (37°C) the foam T_g is reduced, allowing expansion back to original shape to fill up the space of wound, clotting the blood and reducing further hemorrhage. One of the main advantages of these foams over commercially-available hemostatic materials is that their chemistry can be tuned according to application requirements. The goal of the current work is to modify the SMP foams to degrade after implantation to enable prolonged use and reduce re-bleed risks during removal.

Weems et al. found that SMP foams undergo oxidative degradation via scission of tertiary amines in the monomers.[19] 'Real-time' in vitro degradation studies in 3% H_2O_2 revealed a 50% mass loss over ~100 days. To increase the degradation rate, previous efforts focused on incorporating hydrolytically degradable ester linkages into the polymer network. Singhal et al. added poly(caprolactone) macromers into the system.[20] These foams had a relatively low T_g around 20°C, which limits their stable storage in the secondary shape, and mass losses were slow, even in accelerated degradation media.[21] Weems et al. synthesized succinic acid-based ester-containing foams with higher T_g.[22] However, degradable formulations still had relatively low dry T_g (~37°C) and mass loss rates that are slower than wound healing rates (complete mass loss in 80 days in 2% H_2O_2). To improve upon this system, degradable SMP foams with appropriate thermal properties ($T_g>50°C$) were developed by Jang et al. using ester-containing trifunctional monomers.[23] However, the fastest complete mass loss was observed within 90 days in an accelerated oxidative degradation medium (20% H_2O_2). Thus, SMP foams with appropriate thermal properties and more rapid degradation rates to better match tissue regeneration are still required.

Due to the hydrophobicity of the foams, we hypothesized that clinically-relevant degradation rates (~6 to 8 weeks, based on previous clinical data[24]) could be obtained by increasing the local hydrophilicity around hydrolytically degradable ester groups. To that end, we synthesized new monomers by esterifying nitrilotriacetic acid (NTA) with diethylene glycol (DEG) and incorporated the resulting ester-containing monomer into SMP foams. NTA includes an oxidatively-degradable tertiary amine, DEG increases hydrophilicity next to the hydrolytically-degradable ester linkages, and the ether linkages of DEG are susceptible to oxidative degradation.[20] After characterizing scaffold properties, cytocompatibility, and blood interactions, degradation was assessed in 3% H_2O_2 at 37°C to mimic real-time oxidative degradation in the body and in an accelerated hydrolytic degradation solution (0.1M NaOH).[25,26] Mass loss, pore size/structure, surface chemistry, and T_g were measured over time to establish *in vitro* degradation profiles. These SMPs have the potential to provide an easy-to-use, shape-filling hemostatic dressing that can be left in place during traumatic wound healing.

A2. Materials and Methods

1.   Materials: Hydrogen peroxide (H_2O_2, Certified ACS, 30%), sodium hydroxide (NaOH), ethanol (reagent alcohol), chloroform, nitrilotriacetic acid (NTA), 1-(3-dimethylaminopropyl)-3-ethylcarbodimide HCl (EDC), 4-(dimethylamino)pyridine (DMAP, ≥99%), hexamethylene diisocyanate (HDI), N,N,N',N'-tetrakis-(2-hydroxypropyl)-ethylenediamine (HPED), triethanolamine (TEA), diethylene glycol (DEG), Triton X-100, and Phosphate buffered saline (PBS) were purchased from Fisher Scientific (Waltham, MA) and used as received. Porcine Blood was purchased from Lampire Biological Laboratories (Pipersville, PA). Glutaraldehyde was purchased from Electron Microscopy Sciences (Hatfiled, PA) EPH-190, BL-22, and T-131 were provided by Evonik (Essen, Germany) and used as received.

2.   Synthesis of Ester-Containing Triol: NTA and DEG were added to chloroform at a 1:3 molar ratio with 0.1 mol. eq. of DMAP and 3 mol. eq. of EDC as catalysts, **Figure A1**. The reaction was carried out at 40 °C in a nitrogen environment over molecular sieves, which were added to capture water produced during the esterification reaction. Attenuated total reflectance Fourier transform infrared spectroscopy (ATR-FTIR, Nicolet iS10, Thermo Scientific) was carried out on the reaction product every 24 hours to track its completion according to the introduction of a peak at ~1714 cm^{-1} that corresponds with the C=O of the ester. Upon reaction completion, excess solvent was vaporized using rotary evaporation, and the final product was dried overnight under vacuum. The dried product, NTA-DEG, was analyzed using ATR-FTIR and ^{1}H-nuclear magnetic resonance (NMR, Bruker Avance III HD 400 MHz) spectroscopy to confirm the formation of ester linkages. Successful esterification of DEG was indicated by an ester peak at 1741 cm^{-1} in the FTIR spectra. NMR spectra were collected in $CDCl_3$ at 298 K using TMS/solvent signal as an internal

reference. NTA-DEG: ^{1}H NMR (CDCl$_3$; ppm): 3.64 (t,-CH$_2$CH$_2$OCO-), 3.64 (t,-CH$_2$OH), 3.72(s,-CH$_2$N-), 3.78(t,-CH$_2$CH$_2$OH), 4.25(s, - CH$_2$OCO-). NMR confirmed 85-88% functionalization of NTA carboxylic acids with DEG.
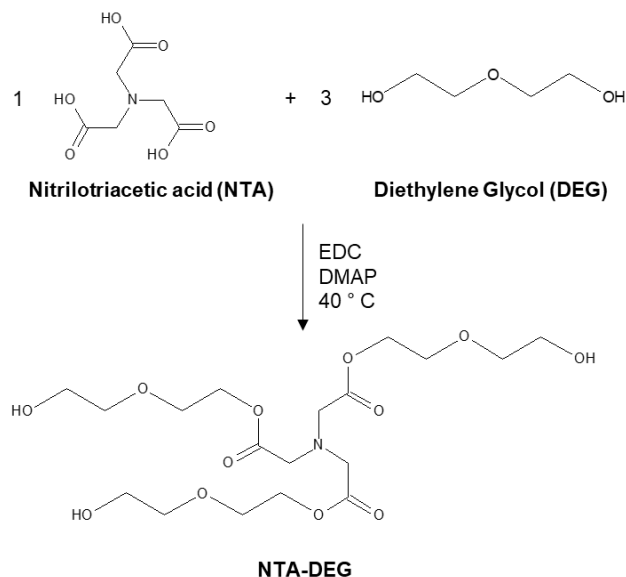
Figure A1. Synthesis of ester-containing monomer, nitrilotriacetic acid (NTA)-diethylene glycol (DEG).

3. Foam synthesis: Polyurethane foams were fabricating using a two-step process. In the first step, an isocyanate (NCO) pre-mix was prepared that contained 100 mol% of required isocyanates from HDI and a fraction of hydroxyl equivalents from HPED, TEA, and NTA-DEG. The pre-mix was reacted at 50°C for 48 hours. The remaining mol% of hydroxyl components were mixed with catalysts (T-131 and BL-22) and a blowing agent (deionized (DI) water). Surfactant (EPH-190) was added to the pre-mix after the 48-hour cure. The NCO pre-mix and hydroxyl components were mixed in a high-speed mixer (Flacktek, Landrum, SC) and poured into a large beaker, which was incubated at 50°C for

5-10 minutes to allow for foam formation. Synthesized foam compositions are shown in **Table A1**.

Sample ID	HDI (wt%)	HPED (wt%)	TEA (wt%)	DEG (wt%)	NTA-DEG (wt%)	EPH 190 (wt%)	T-131 (wt%)	BL-22 (wt%)	Water (wt%)
Control	54.03	27.61	8.05	-	-	6.44	0.46	1.01	2.37
15% NTA-DEG	49.45	25.27	-	3.93	11.23	6.44	1.20	1.01	2.40
30% NTA-DEG	43.10	24.40	-	-	21.71	6.17	1.10	1.23	2.29

Table A1. Synthesized foam compositions.

4. Foam Pore Analysis: Pore sizes of samples were measured using scanning electron microscopy (SEM). Samples (n=3, 1 cm^2) were cut along the vertical and lateral foam axes and sputter-coated with gold using a Denton Vacuum sputter coater before imaging (Jeol JSM 5600) at 35X magnification and 10 kV high vacuum. The micrographs were analyzed using ImageJ software to quantify pore diameters.

5. Density: Samples (n=3) were cut into cubes (1 cm^3) using a hot wire cutter, and the length of each face was measured using digital calipers. Measurements were converted to volumes and samples were then weighed to determine densities.

6. Mechanical Testing: Samples (n=3) were cut in a dog bone shapes (ASTM D638 scaled down by a factor of 4) with a gauge length of 6.25 mm and width of 1.5 mm. The samples were tested in both dry and wet conditions. To measure wet tensile properties, samples (n=3) were placed in 50°C DI water for 5 minutes, and pressed dry prior to fixing

on the tensile tester. Samples were placed into a tensile tester with a 24N load cell and stretched at a rate of 2 mm/min until failure to measure elastic modulus, elongation at break, and ultimate tensile strength.

7. Thermal Analysis: A Q200 differential scanning calorimeter (DSC, TA Instruments, New Castle, DE) was used to measure T_g. Samples (n=3, 3-5 mg) were placed in t-zero aluminum pans and then equilibrated at -40°C, heated to 120°C at 10°C/min, kept isothermally for 2 minutes, cooled to -40°C, kept isothermally for 2 minutes, and heated to 120°C at 10°C/min. Dry T_g was measured as the half-height transition temperature during the second heating cycle. To measure wet T_g, samples (n=3) were placed in 50°C DI water for 5 minutes, pressed dry, and placed in t-zero aluminum pans prior to running a single heating cycle.

8. Swelling Ratio: Cylindrical foam samples (~20-30 mg in dry weight) were cut, cleaned in DI water and 70% ethanol, and dried under vacuum at 40°C. Their dry masses (W_d) were obtained (n = 3), and then they were placed in 37°C water for 1 hr. Samples were patted dry on a laboratory wipe and then weighed to obtain swollen masses (W_w). Swelling ratio (SR) was calculated as:

$$SR = \frac{W_w - W_d}{W_d} \times 100\%$$

9. Shape Memory Behavior: Cylindrical foam samples (1 cm length, 8 mm diameter) were cut, cleaned in DI water and 70% ethanol, and dried under vacuum at 40°C. Cleaned samples were heated to 100°C for 10 minutes. The diameter (n=3) was measured using

digital calipers prior to crimping cylinders in a radial compression crimper (Blockwise Engineering, Tempe, AZ) and cooling them down while crimped. Crimped samples were placed in vials in a dry box containing desiccant for 24 hours and then fixed on a 330 μm Nitinol wire. Their diameters were measured again, and then they were placed in a DI water bath at 37°C. Expansion profiles were captured using a camera that recorded images every 5 seconds for 5 minutes. The images were processed using Insight Toolkit (ITK) to measure the change in diameter over time. Foam area (number of pixels) from each image was normalized against that of the last image with known diameter (measured using calipers after foam was removed from the water bath), and % volume recovery was calculated as:

$$\% \, Volume \, Recovery = \frac{Sample \, Diameter\,(t)}{Initial \, Diameter} \times 100\%$$

Foam diameter vs. time was plotted over the expansion time frame.

10. Spectroscopic Analysis: Surface chemistry of foams was characterized by collecting ATR-FTIR spectra on thin slices of foam at 0.8 cm^{-1} resolution.

11. Cytocompatibility: NIH/3T3 Swiss mouse fibroblasts (ATCC–CCL92) were cultured with Dulbecco's Modified Eagle Medium (DMEM, high glucose GlutaMAX) supplemented with 10% heat-inactivated fetal bovine serum (FBS) and 1% penicillin-strepotomycin (P/S, Gibco) at 37°C/5% CO_2. For all studies, cells (between passages 4 and 6) were used after 3 days of culture. Cells were seeded in a 24 well tissue-culture polystyrene plate at 10,000 cells/well and cultured for 24 hours. Morphology was assessed using a Zeiss Axiovert inverted microscope to confirm even cell distribution. Media was removed, and cells were washed with sterile phosphate buffered saline (PBS) prior to

exposure to samples. Then, cleaned foam pieces were placed in Transwell® inserts in the pre-seeded plates along with fresh DMEM with 10% FBS and 1% P/S. Positive (cytocompatible) controls included wells with empty inserts, and negative (cytotoxic) controls included wells with empty inserts and 0.5% H_2O_2 in media.

Following incubation over 3, 24, and 72 hours, a Resazurin Cell Viability Assay was utilized to quantify cytocompatibility. Transwell inserts and solutions were removed from wells and replaced with the Resazurin cell viability stain for 4 hours at 37°C. Then, a plate reader (FLx800, Bio-Tek Instruments, Inc.) was used to measure absorbance at 570 nm. Cell viability was calculated as:

$$\text{Cell Viability (x)} = \frac{Abs_{570}(x)}{Abs_{Control}} \times 100\%$$

where x is the selected treatment group and the empty insert control is used as a standard that equals 100% viability.

12. Blood Interactions: Porcine blood (Lampire Biological Laboratories, Pipersville, PA, USA) anticoagulated with Na-Citrate upon collection was stored at 4°C for up to 3 weeks from the bleed date. Control, 15% NTA-DEG and 30% NTA-DEG foams were washed and dried prior to characterization in all studies. QuikClot Combat Gauze was included as a clinical control. Blood absorption was analyzed by weighing dry samples (n = 3; ~50 mg) and incubating them in blood at 37°C. Samples were weighed at 24 hrs, and blood absorption was calculated as:

$$\% \, Absorbed = \frac{W_b - W_d}{W_d} \times 100\%$$

Where W_b is the mass of the sample in blood and W_d is the dry mass.

Coagulation time was measured by placing samples (n = 4) in 1.5 ml tubes, with empty tubes serving as negative (non-clotting) controls. Blood was brought to room temperature, and a 1M $CaCl_2$ solution was added to obtain a final concentration of 0.01M $CaCl_2$ and reverse the anticoagulant. Then, 50 µl of blood was added to each sample tube. At each time point (every 6 minutes over 30 minutes), 1 ml of DI water was added to the tubes to stop the clotting process and lyse free red blood cells. Tubes were centrifuged (2300 rpm, 15 min), inverted, and imaged using a digital camera. Then, 200 µl of lysate was pipetted from each tube into a 96 well plate, and absorbance was measured at 540 nm using a Biotek Synergy 2 Multi-Mode Microplate Reader (Winooski, VT, USA) to determine the relative amount of hemoglobin released at each time point.

13. Platelet Attachment: A LDH cytotoxicity assay kit (Cayman Chemical, Ann Arbor, MI) was used to quantify the attachment of platelets to samples. To obtain a standard curve, whole blood was centrifuged at 3000 rpm for 15 minutes to obtain platelet rich plasma (PRP). Multiple concentrations of PRP were prepared by diluting with PBS at 100%, 50%, 25%, 12.5%, and 6.5% to generate a standard. Hemocytometer counts at each PRP concentrations (n=4) were acquired and used to quantify standard values.

SMP foams (n=4) were cut to have equal surface areas and placed in the wells of a 24 well-plate. Gauze was used as a clinical control. Then, 1 ml of whole blood was added to each well and the plate was incubated at 37°C for 30 minutes. Non-attached platelets were washed away with PBS. Samples were transferred to another plate containing 1 ml of fresh PBS and 100 µL 10% Triton X-100 and incubated at 37°C for 1 hour to lyse the attached platelets. Then, 100 µL of supernatant was taken from each sample well and transferred to

a 96 well-plate. The LDH Reaction solution (100 µL) was added to each well, and the plate was incubated for 30 minutes at 37°C on an orbital shaker. Following incubation, absorbances were read on the microplate reader at 490 nm.

15. Platelet Activation: SMP foams (approximately 0.5 cm^3) were incubated in whole blood and rinsed of non-attached platelets. To observe activity states and activation of the attached platelets, samples were prepared for scanning electron microscope (SEM) imaging. Samples were fixed in a solution of 2% glutaraldehyde (Electron Microscopy Sciences, Hatfield, PA, USA) overnight at 4°C. Following fixation, samples were dehydrated in solutions with increasing concentrations of ethanol: 1) 30 minutes in 50% ethanol, 2) 30 minutes in 70% ethanol, 3) 30 minutes in 95% ethanol, 4) 30 minutes in 100% ethanol. Final dehydration was accomplished through drying overnight in a vacuum oven at room temperature, and samples were sputter coated with 5-10 nm of gold. SEM analysis was performed using a Jeol NeoSCope JCM-5000 Scanning Electron Microscope at an operating voltage of 10kV. Random regions of interest were imaged at 1000X and 5000X magnification. Images were analyzed qualitatively for signs of platelet aggregation and morphology change.

16. Degradation Analysis: Cylindrical foams (n=8, 8 mm diameter, 1 cm height) were washed and dried, and initial masses were obtained using a gravimetric scale. Samples were placed in 3% H_2O_2 (real-time oxidative degradation media) or in 0.1M NaOH (accelerated hydrolytic degradation media) at 37°C. Every 3 days, the degradation media was changed. At selected time points, samples were washed with ethanol and dried under vacuum for 24

hours. After drying, samples were imaged using a camera, and masses were measured (n=5). A thin slice was cut from a sacrificial set of foams (n=3) and used to measure pore morphology, T_g, and surface chemistry as described above.

17. Statistical Analysis: Measurements are presented as mean ± standard deviations. Student's T-tests were performed to determine differences between NTA-DEG foams and controls. Statistical significance was taken as $p<0.05$.

A3. Results

1. Structural Properties: All formulations had a pore size of approximately 1100 µm, and both NTA-DEG formulations had comparable pore sizes to the control, **Figure A2**. In general, foam densities were low (<0.06 g/cm³) for all formulations, demonstrating that the NTA-DEG monomer can be incorporated into low density foams. The addition of NTA-DEG resulted in pore opening, with interconnects visible in pore walls (**Figure A2c**), which corresponds with a significantly reduced density in the 30% NTA-DEG foams relative to that of the control foam.
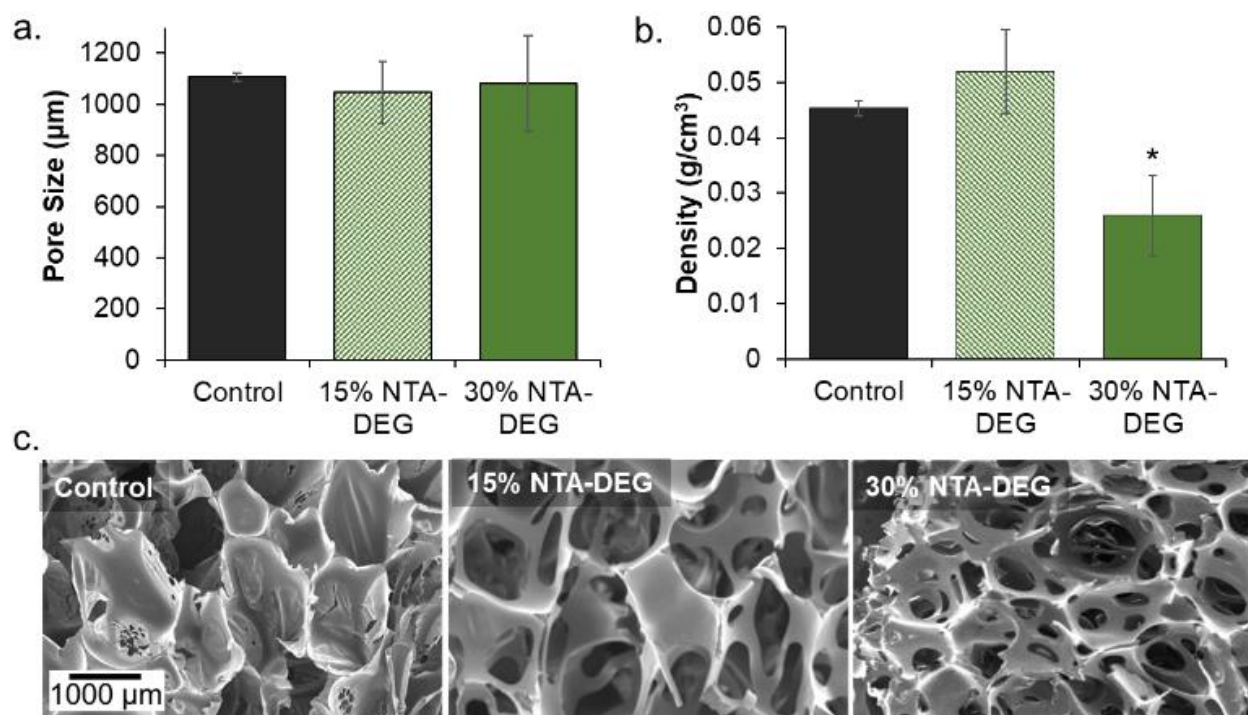
Figure A2. Structural properties of synthesized foams. (a) Average pore size of foams (n=6) measured using SEM micrographs and subsequent SEM analysis. (b) Foam densities (n=3). (c) Representative SEM micrographs of foam samples used for pore analysis. Scale bar of 1000 µm applies to all images. Average ± standard deviation displayed in (a) and (b). *p<0.05 relative to control foam.

2. Thermal Properties: The use of polyol crosslinkers with three (TEA and NTA-DEG) and four (HPED) hydroxyl groups provides an amorphous, highly crosslinked network that is indicated by the absence of melting peaks in the DSC plots. The shape memory properties are designed around the dry and wet T_g's of the system. **Figure A3a** shows that all foam formulations have dry T_g's over 40°C, which ensures that the biomaterials maintain their compressed secondary shape when stored in dry conditions. The wet T_g's are reduced to below 37°C due to plasticization of the network by water, as shown in **Figure A3b**, which allows for actuation of shape memory properties after exposure to water in body temperature blood upon implantation.

3. Hydrophilicity and Shape Memory Behavior: Swelling ratios in water were calculated to provide an indication of material hydrophilicity, **Figure A3c**. Control foams swelled by 55% in 5 minutes, and the effective swelling after 24 hours was 56%. Similarly, 30% NTA-DEG swelled by 64% in 5 minutes and 51% in 24 hours, while 15% NTA-DEG swelled a significantly lower amount of 15% in 5 minutes and by 23% in 24 hours. The statistically similar swelling ratios at the 5-minute and 24-hour time points indicate that equilibrium swelling is reached within the first 5 minutes of water incubation with these foams. Shape memory properties of foams are required to ensure that they expand to their original shape after implantation and exposure to body temperature blood. The volume recovery profiles of the foams in water at 37°C are shown in **Figure A3d**. Control foams expanded back to their original shape within ~200 seconds, while NTA-DEG foams reached 100% volume recovery within ~25 seconds.
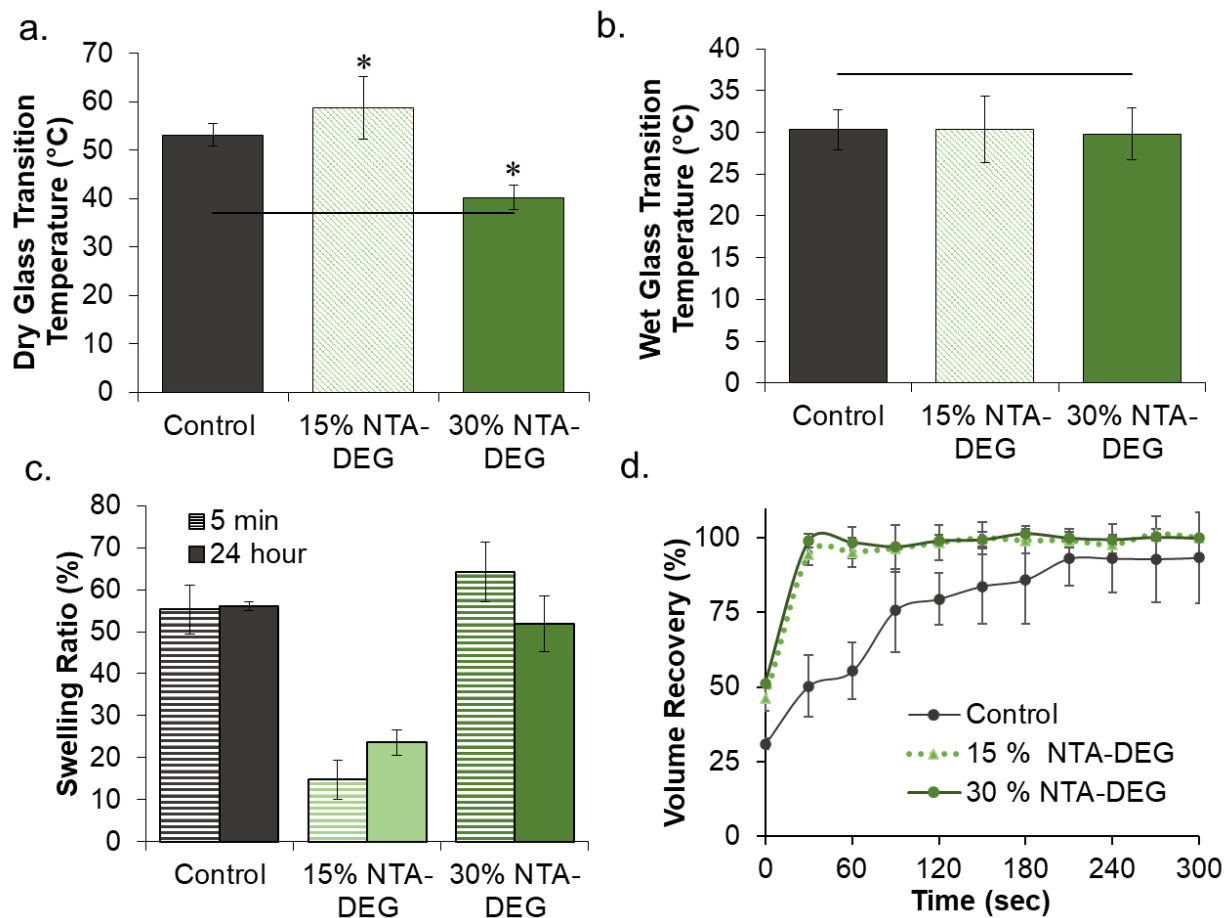
Figure A3. Thermal and shape memory properties of SMP foams. T_g measured via differential scanning calorimetry under (a) dry and (b) wet conditions (n=3). *p<0.05 relative to control. Horizontal lines indicate body temperature (37°C). (c) Volumetric swelling ratios in water at 5 minutes and 24 hours at 37°C (n=3). (d) Volume recovery profiles of foams samples in deionized water at 37°C (n=3). Average ± standard deviation displayed for all data.

4. Tensile Testing: Mechanical testing data are presented in **Table A2**. In general, elastic modulus and tensile strength decreased and maximum elongation increased with the addition of NTA-DEG. These trends were observed in both dry and wet/plasticized conditions. Relative differences in elastic modulus were reduced in wet conditions (15X and 41X decrease between

165

control and 15% and 30% NTA-DEG, respectively, in dry condition vs. 6X and 10X decrease in wet condition). Tensile strength was similar between samples in the wet state, and ultimate elongation differences increased in wet conditions.

Table A2. Tensile properties of shape memory polymer foams in dry and wet conditions. n=3, average ± standard deviation displayed. *p<0.05 relative to control.

Sample	Dry			Wet		
	Elastic Modulus (kPa)	Ultimate Tensile Strength (kPa)	Maximum Elongation (mm/m)	Elastic Modulus (kPa)	Ultimate Tensile Strength (kPa)	Maximum Elongation (mm/m)
Control	3216 ± 1669	528 ± 230	0.17 ± 0.04	153 ± 22	53 ± 21	0.36 ± 0.19
15% NTA-DEG	217 ± 86 *	69 ± 26 *	0.39 ± 0.2	24 ± 5 *	45 ± 20	1.73 ± 0.39
30% NTA-DEG	78 ± 33 *	94 ± 7 *	1.39 ± 0.6 *	15 ± 3 *	70 ± 24	4.53 ± 1.34 *

5. Cell and Blood Interactions: Cell viability was >75% for all samples over 72 hours, **Figure A4a**. Control foams absorbed significantly more blood than gauze and NTA-DEG foams, **Figure A4b**. The lowest blood absorption was measured in 15% NTA-DEG foams, followed by 30% NTA-DEG foams. Clotting times were measured relative to a gauze clinical control, **Figure A4c**. At 6 minutes, all SMP foams had significantly higher free red blood cells (RBCs) relative to the gauze clinical control, indicative of reduced clotting. However, by 12 minutes, all samples had comparable clotting levels.
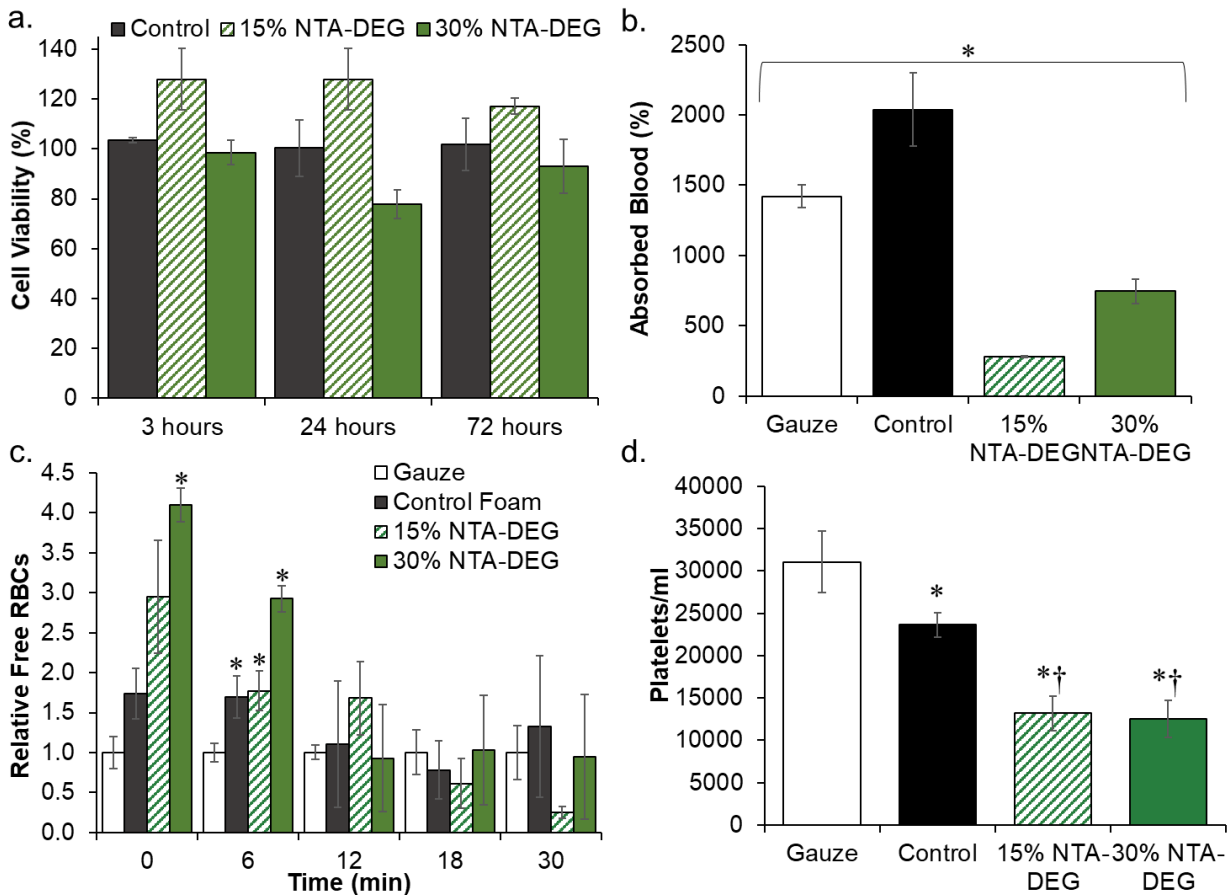
Figure A4. Cell and blood interactions with SMP foams. (a) 3T3 fibroblast viability over 3, 24, and 72 hours (n=3). (b) Blood absorption over 24 hours at 37°C (n=3). *$p<0.05$ between all 4 samples. (c) Blood clotting times in terms of free red blood cells (RBCs) relative to gauze clinical control over 30 minutes (n=4). *$p<0.05$ relative to gauze. (d) Platelet attachment concentrations measured using the LDH assay (n=4). *$p<0.05$ relative to gauze. †$p<0.05$ relative to control foam. Average ± standard deviation displayed for all data.

5. Platelet attachment and activation: Decreasing concentrations of PRP resulted in a linear decrease in platelet numbers that could be used to quantify the concentrations of attached platelets on samples using the LDH assay. As shown in **Figure 4Ad**, the highest levels of platelet

attachment were observed on the gauze clinical control, followed by the SMP control foam. Ester containing foams had significantly lower concentration of attached platelets compared to the controls. Platelets were found on all materials in SEM images. The granules released from cytoplasm of platelets upon activation after attachment can be visualized by the small protrusions seen in **Figure A5**. The gauze clinical control contained areas of thrombus formation, indicated that platelets attached, aggregated, and activated during the 30 minutes of whole blood incubation. All SMP formulations showed evidence of platelet attachment and activation. Aggregates were found on control and 15% NTA-DEG samples, while 30% NTA-DEG samples had lower platelet density.
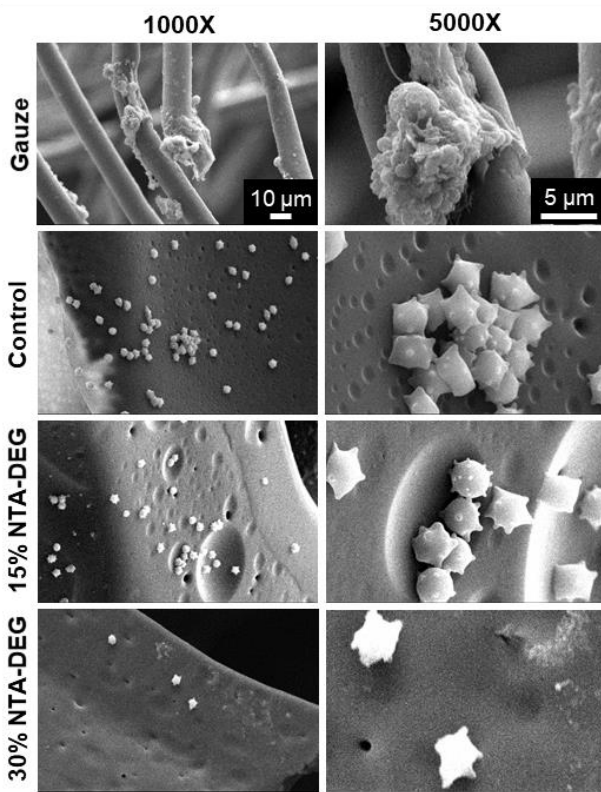
Figure A5. SEM micrographs of attached and activated platelets after incubation in whole porcine blood. Scale bars apply to all images in a given column.

6. Degradation Analysis

6.1 Mass loss and physical erosion: Despite the inclusion of hydrolytically-degradable ester linkages, NTA-DEG foams were relatively stable in 0.1M NaOH, **Figure A6b**. They lost ~20% of their mass within 1-2 weeks, after which mass loss plateaued. In 3% H_2O_2, the 30% NTA-DEG foams underwent linear mass loss (R2 = 0.953) over 30 days, **Figure A6a**. The 15% NTA-DEG foams had a consistent, linear mass loss (R2 = 0.976) in 3% H_2O_2 with full degradation at 100 days. Control foams have initially slow degradation rates, and the rate increased around 42 days until 100% degradation within 72 days (R2 = 0.894). In general, NTA-DEG foams remained in a single piece throughout the degradation process, which indicates that surface erosion occurred in these samples, while control foams start to break apart into smaller pieces after ~42 days, **Figure A7**.

6.2 Thermal Analysis: Variations in T_g throughout degradation provides an indication of relative crosslink densities over time. This information can be used to determine if the materials undergo bulk degradation, where the entire network is attacked at once, or surface degradation, where the network remains relatively stable.[27–29] Retained T_g's throughout the degradation time frame, as shown in **Figure A7,** indicates that the polymer networks remained fairly intact and that degradation occurred primarily on the surface of the materials. This is expected for oxidative degradation, due to the high reactivity of reactive oxygen species.[30] The 15% NTA-DEG foam T_g dropped at 70 days, indicating that bulk hydrolysis may take over as the primary degradation mechanism at this point. [29]
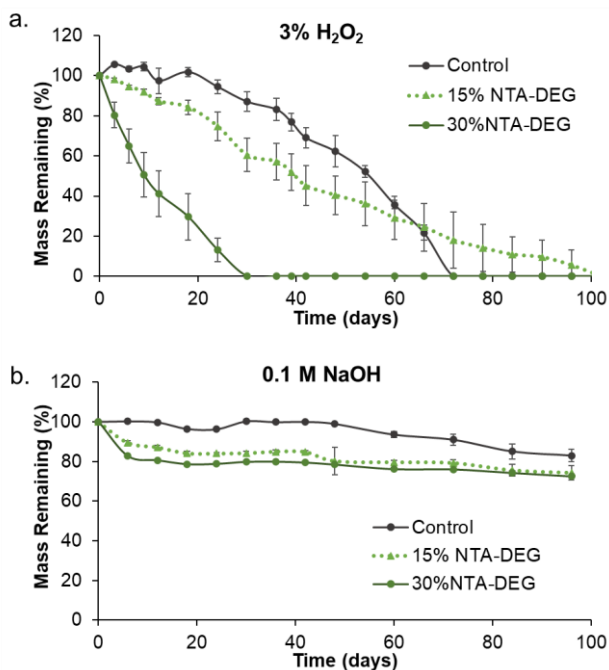
Figure A6. Mass loss of samples as a function of time (n=5) in (a) real-time oxidative degradation media (3% H_2O_2) and (b) accelerated hydrolytic degradation media (0.1M NaOH). Average ± standard deviation displayed.

6.3 Pore Morphology: Pore morphology of foams was observed every two weeks via SEM, as shown in **Figure A8**. In the case of control foams in 3% H_2O_2, the pores began to collapse by 14 days with significant strut breakage by 28 days. Total pore collapse at 42 days corresponds to the macro-scale breaking apart of control foams shown in **Figure A7**. Pore morphology was the most stable in the 15% NTA-DEG foams, with visible pores and interconnects as late as 42 days, despite the increased mass loss in these samples in comparison with the controls (69 ± 5% remaining in control vs. 45 ± 9% remaining in 15% NTA-DEG). The 30% NTA-DEG foams degraded too much for imaging by the 28 day time point, and evidence of significant degradation (loss of struts) can be seen by 14 days.
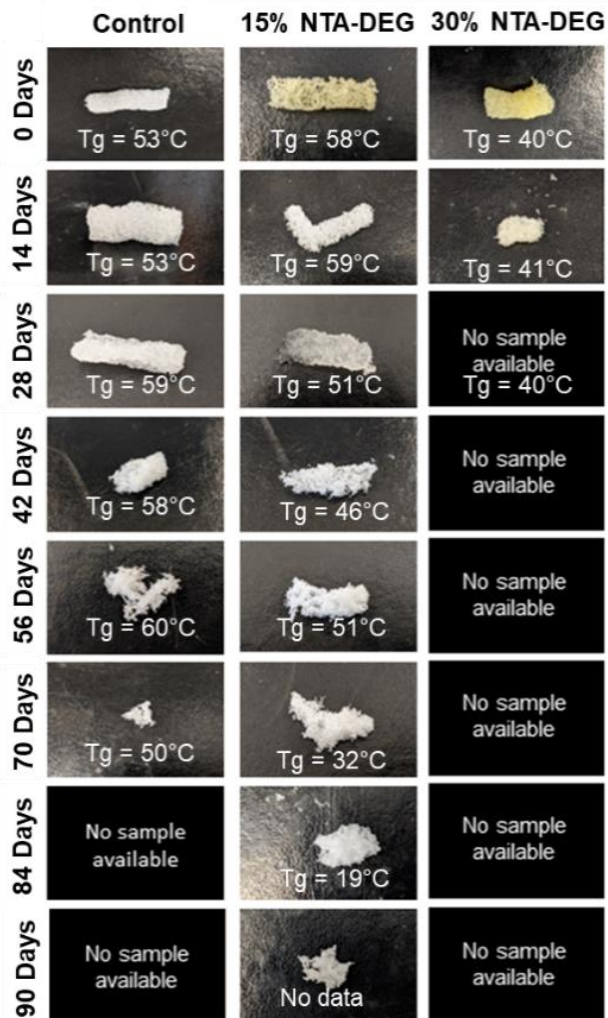
Figure A7. Erosion profile and glass transition temperatures of samples during degradation in 3% H_2O_2. No sample was available for imaging upon almost complete degradation at ~28 days for 30% NTA-DEG foams and at ~84 days for controls.

6.4 Spectroscopic Analysis: As seen in **Figure A9**, a shift in the carbonyl of urethane peak from 1680 cm^{-1} to 1688 cm^{-1} and a reduction in the tertiary amine of HPED and TEA (and NTA for ester-containing foams) at 1050 cm^{-1} is an indication of oxidative degradation across all the formulations, as previously shown.[19,23] Among the NTA-DEG foams, an increase in the carbonyl

of carboxylic acid peak at 1650 cm^{-1} is attributed to carboxylic acid byproduct formation during hydrolytic cleaving of ester linkages.
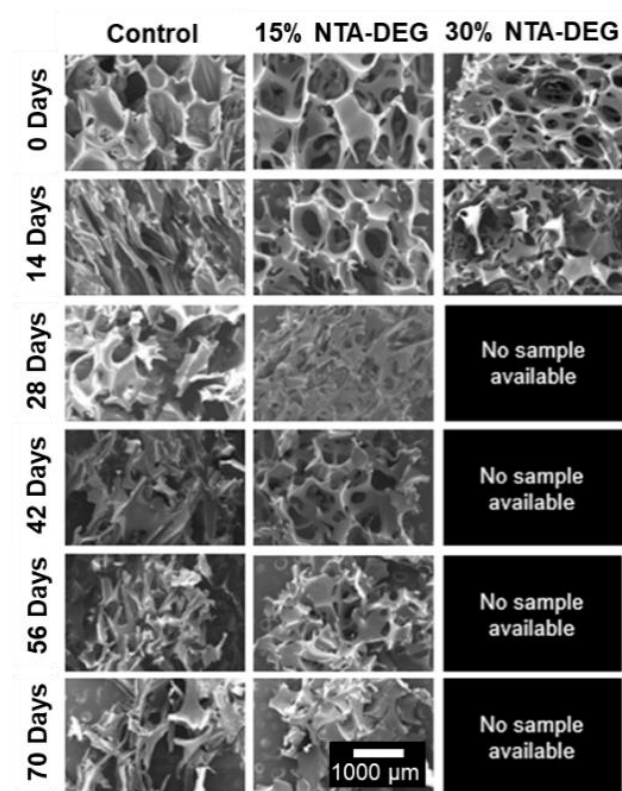
Figure A8. SEM micrographs of samples throughout 10 weeks of degradation in 3% H_2O_2. 30% NTA-DEG degraded completely by the 28 day time point. Scale bar of 1000 μm applies to all images.
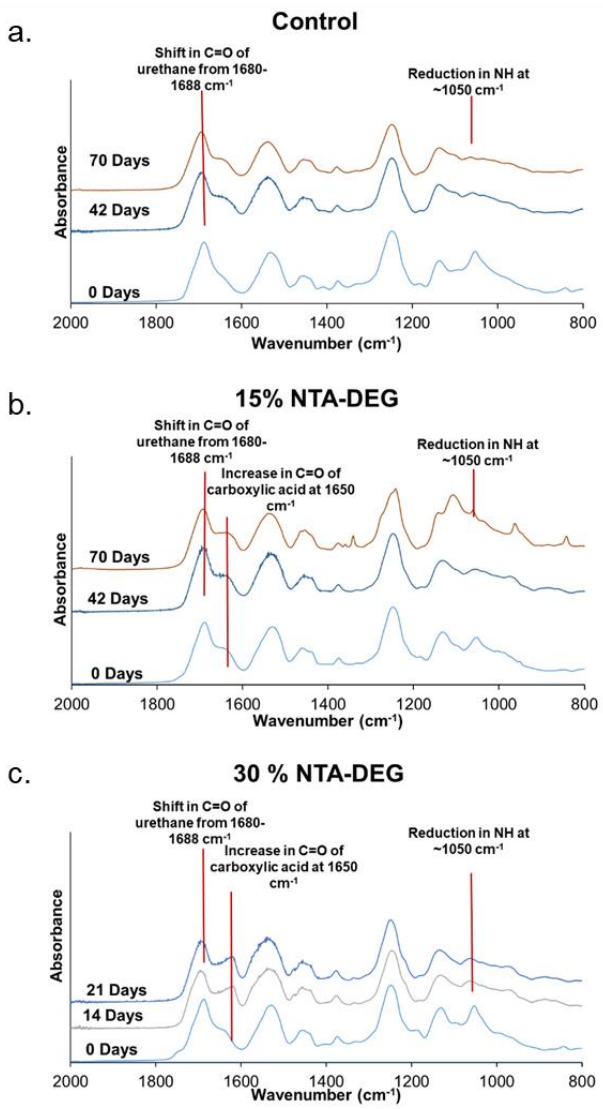
Figure A9. FTIR spectra of (a) Control, (b) 15% NTA-DEG and (c) 30% NTA-DEG, throughout 10 weeks of degradation in 3% H_2O_2. 30% NTA-DEG degraded completely after the 21 day time point.

A4. Discussion:

1. Foam characterization: The addition of NTA-DEG as a monomer aided in opening the pores, as demonstrated by pinholes in pore walls, **Figure A2c**. This increased interconnectivity between pores may be attributed to the hydrophilicity of DEG. Namely, the relatively hydrophilic DEG component increases interactions between the pre-polymer/monomers and the water blowing agent and/or surfactant to aid in pore opening. Previous attempts to increase interconnectivity in SMP foams rely upon mechanical reticulation, plasma treatment, and/or use of physical blowing agents.[31,32] Inclusion of more hydrophilic monomers presents a new method for pore opening in these materials. This interconnectivity could increase nutrient transfer throughout the biomaterial scaffold as well as allow for tissue and blood vessel ingrowth, and it expands potential future applications for SMP foams in tissue engineering and regenerative medicine applications.[33,34]

In general, SMPs contain two main components at the molecular level, known as netpoints and switching segments.[35] Netpoints define the permanent shape of the SMP. In this specific material system, the netpoints are covalent crosslinks that form during synthesis (urethane linkages that form upon reaction with hydroxyls with isocyanates). Switching segments provide the mechanism for shape memory. In this specific system, the switching segments are hydrogen bonds that form between urethane linkages in between the crosslinks. At temperatures above the T_g, hydrogen bonds are broken between the network chains to increase flexibility, making the material elastic. This elasticity allows for deformation (radial crimping in this case) into the secondary shape. Upon cooling below the T_g, new hydrogen bonds form between chains that have been re-arranged during crimping, again limiting SMP flexibility and fixing the temporary shape. Upon exposure to body temperature water after shape fixation, the hydrogen bonds between the urethane linkages are

interrupted by water plasticization that reduces the T_g and triggers shape recovery at a relatively lower temperature in the wet condition.

A reduction in dry T_g of 30% NTA-DEG foams can be attributed to the longer chain length and increased flexibility of NTA-DEG monomers, which theoretically reduces overall crosslink density and network rigidity. Plasticization after exposure to water reduces the T_g in the wet state and enables actuation after exposure to body temperature (37°C water). All foams have wet T_g below 37°C. It was originally hypothesized that NTA-DEG foams may have lower wet T_g due to the hydrophilic DEG chains; however, wet T_g's were statistically similar for the three foam formulations. The retained wet T_g of NTA-DEG foams as compared to controls is attributed to intermolecular bonding between the dipoles of ester linkages.

Previous research on polyurethane foams shows that the materials primarily hydrogen bond with water through the N-H groups rather than through the C=O linkages, based upon Fourier transform infrared (FTIR) spectra.[36] Namely, when hydrogen bonds form at the N-H groups, the N-H infrared band at ~3307 cm^{-1} increases in intensity and shifts to higher wavenumbers. When hydrogen bonding occurs via bridges between two C=O groups, the FTIR spectra shows an increase in the intensity of the C=O peak at ~1687 cm^{-1} with shifts to lower wavenumbers. In the current study, we collected FTIR spectra on foams that had been submerged in water at 50°C for 5 minutes and compared those with dry foam spectra. The N-H peak intensities increased with general shifts to higher wavenumbers in the wet foam spectra, indicating the presence of hydrogen bonds between water and the N-H groups in the urethane linkages. Meanwhile, the C=O peaks at ~1687 cm^{-1} were of similar intensity between the wet and dry samples, with no apparent shift in wavenumber, indicating minimal hydrogen bonding between these groups in these materials. These FTIR spectra support the hypothesis that the dipole-dipole bonds in these foams are less

susceptible to water plasticization via hydrogen bonding, with would correlate with reduced effects on wet T_g in this system.

This hypothesis also correlates with the foam swelling ratios in water. Namely, there is a drop in swelling in the 15% NTA-DEG foams that may be attributed to the dipole-dipole bonds with reduced water access. With an increase in NTA-DEG content to 30%, the hydrophilicity of DEG overcomes these restrictions to increase water interactions with the network. The faster volume recovery observed with NTA-DEG foams is likely due to the open pore structure, which enables faster water penetration and shape recovery from the compressed form. This property could be beneficial for hemostatic dressing use, as it would allow for faster wound filling after implantation.[37]

Based on the theoretically reduced crosslink density and open pore structure in NTA-DEG foams, the dry mechanical property trends (decreased elastic modulus and tensile strength and increased ultimate elongation with NTA-DEG incorporation) were generally expected. Some of these differences could also be attributed to the reduced density of 30% NTA-DEG foams. The smaller differences in modulus and strength between NTA-DEG foams and controls in the wet state are again attributed to secondary intermolecular forces in the samples. The carbonyl linkages of the ester groups interact via secondary dipole interactions that are less affected by water in comparison with the hydrogen bonds between urethane linkages. Thus, plasticization does not affect the NTA-DEG foam flexibility to the same extent as that of control foams. While the wet mechanical properties are more similar between formulations, it may be beneficial to tune the stiffness of NTA-DEG foams in future studies by increasing HPED content or decreasing diisocyanate monomer chain length with butane diisocyanate in place of HDI.

2. Biological Characterization: All of the foams retained high cytocompatibility (>75%) over 72 hours, which meets the ISO 10993 standard for cytocompatibility.[38] Future studies will focus on measuring cytocompatibility of degradation products and *in vivo* host response during degradation to provide a better understanding of the material biocompatibility. The absorbed blood amounts generally correlate with swelling ratios in water, with the control foam having the highest volume of absorbed blood and 15% NTA-DEG having the lowest volume. The decrease in blood absorption in the 30% NTA-DEG foam relative to the control foam could be attributed to the open pore structure, which likely reduced the amount of retained (anticoagulated) blood after removal.

Clotting times were measured relative to gauze. SMP foams all had slower clotting times with increased free RBCs at 0 and 6 minutes. However, by 12 minutes, all samples had fully clotted with no differences between free RBC levels. In general, the 30% NTA-DEG foam appeared to clot the slowest of the tested formulations. This trend was also seen in the platelet attachment numbers, where gauze had the highest number of platelets, followed by the control foam. The NTA-DEG foams had the lowest platelet numbers. The platelet images correlate with these results, based on evidence of more advanced thrombus formation on the gauze sample. All SMP formulations promoted platelet attachment and activation, demonstrated by the protrusions on individual platelets. Control and 15% NTA-DEG foams had areas with platelet aggregates, a precursor to thrombus formation. The 30% NTA-DEG foams had the lowest levels of imaged platelet numbers and aggregates.

Interestingly, in our preliminary *in vivo* experiments in a porcine liver injury[39], treatment with control foams slightly reduced blood loss and significantly increased animal survival in comparison with gauze treatment. Thus, based upon comparisons between gauze and control SMP foams, the *in vivo* clotting process is more complex than we are able to replicate with these initial

in vitro studies and likely requires further investigation in less static conditions. However, it does appear that the modification with degradable NTA-DEG reduces the clotting capabilities of SMP foams. One of the main benefits of the SMP foam system is its synthetic tunability. We have parallel work that involves incorporation of antimicrobial phenolic acids into SMP foams to reduce infection risks.[40] In addition to their antimicrobial properties, phenolic acids demonstrate procoagulant activity.[41,42] Future work will focus on incorporating procoagulant species, such as phenolic acids, into the NTA-DEG foams to increase their clotting capabilities while maintaining the desired degradation profiles, open pore structures, and flexible mechanical properties.

3. Degradation Profiles: Control SMP foams have excellent hydrolytic stability. Despite the incorporation of hydrolytically-labile ester linkages in NTA-DEG foams, they were very stable in accelerated hydrolytic degradation media after an initial drop in mass by ~20% at the first time point. We hypothesize that this stability could be due to (i) relative hydrophobicity around the ester linkages to reduce water penetration into the network and (ii) initial degradation of only ester linkages and loss of NTA from the polymer, after which the remainder of the network was stable in 0.1M NaOH. Based on prior studies showing that control foams degrade via oxidation of tertiary amines in HPED and TEA monomers, we hypothesized that NTA-DEG foams may degrade more quickly in oxidative conditions.[19,23] As the network degrades oxidatively, it becomes more hydrophilic, enabling increased water access to the hydrolytically-degradable ester linkages to promote hydrolysis. Thus, degradation characterization was focused on samples in oxidative media (3% H_2O_2). Control foams had an initially slow degradation rate with an apparent increase in rate at ~42 days. The change in degradation rate of control foams is consistent with previous SMP foam degradation studies and corresponds with the observed erosion profile.[19,23] This result could be attributed to the relative brittleness of control foams (higher elastic modulus) that causes bulk

erosion upon exposure to external forces during the characterization process. Namely, the foams are washed, dried, and weighed every 3-7 days. Increased brittleness can cause samples to break apart over time of repeated external force application. The non-linear mass loss rates and differences in erosion profiles would likely affect tissue regeneration and load transfer *in vivo* as well and makes estimation of *in vivo* degradation rates more complex.[43–45]

The NTA-DEG monomer was designed to provide multiple potential degradation points. NTA contains a tertiary amine similar to HPED and TEA, which has been previously shown to break down into carboxylic acid and ammonia byproducts.[46] The carboxylic acid groups locally decrease pH within the scaffold, which can accelerate hydrolysis of the ester linkages between NTA and DEG. Finally, DEG contains ether linkages, which (i) enhance hydrophilicity adjacent to the ester linkage to increase water access and (ii) may also degrade oxidatively. Ether oxidation produces carboxylic acids, alcohols, and aldehydes, and the carboxylic acids can further catalyze ester hydrolysis.[15] During the ether degradation process, there is a possibility that the carbon radicals can crosslink with each other to form crosslinks. While crosslinking was not visible on the FTIR spectra (would be indicated by branched ether peak at ~1172 cm^{-1}), it is possible that ether crosslinking occurred simultaneously to oxidative and hydrolytic degradation in 15% NTA-DEG foams to provide a more linear degradation profile and to reduce bulk erosion.

The degradation rate of NTA-DEG foams can be easily tuned with variations in NTA-DEG content. We hypothesize that degradation rates could be further controlled with other monomer variables, such as diisocyanate length, monomer hydrophobicity, and polyol functionality. These foams have linear *in vitro* mass loss rates that, if replicated *in vivo*, could be highly beneficial for graded load transfer from scaffolds to tissues during healing, particularly when considering the

highly interconnected pores. While the focus of the current work is on hemorrhage control, these

foams provide a potential platform for tissue engineering scaffolds in future work.

A5. Conclusions

This study reveals that incorporation of ester linkages using the new NTA-DEG monomer can increase the degradation rate of polyurethane SMP foams to clinically relevant time frames of 4 to 8 weeks[24] while maintaining desired thermal properties. Namely, a dry T_g above 40°C ensures that the foams can be stored in their secondary shape, and a wet T_g below body temperature enables expansion to the primary shape after implantation. The new monomer also imparted other potentially valuable foam properties, including interconnects between the pores that may aid in tissue regeneration, very rapid volume recovery within 30 seconds to aid in hemostatic dressing delivery, and increased flexibility to potentially reduce tears or pre-mature breakdown of scaffolds during delivery or healing. Incorporation of NTA-DEG reduced the clotting capabilities of SMP foams; thus, future studies with these foams will include incorporation of procoagulant species into the tunable material system. Beyond hemorrhage control, these foams provide a platform to future development into other regenerative medicine applications where scaffold degradation is desired.

A6. References

(1)   Holcomb, J.; Caruso, J.; McMullin, N.; Wade, C. E.; Pearse, L.; Oetjen-Gerdes, L.;
Champion, H. R.; Lawnick, M.; Farr, W.; Rodriguez, S.; Butler, F. Causes of Death in US
Special Operations Forces in the Global War on Terrorism: 2001-2004. *US. Army Med.
Dep. J.* **2007**, 24–37. https://doi.org/10.1097/01.sla.0000259433.03754.98.

(2)   Eastridge, B. J.; Mabry, R. L.; Seguin, P.; Cantrell, J.; Tops, T.; Uribe, P.; Mallett, O.;
Zubko, T.; Oetjen-Gerdes, L.; Rasmussen, T. E.; Butler, F. K.; Kotwal, R. S.; Holcomb, J.
B.; Wade, C.; Champion, H.; Lawnick, M.; Moores, L.; Blackbourne, L. H. Death on the
Battlefield (2001-2011): Implications for the Future of Combat Casualty Care. *J. Trauma
Acute Care Surg.* **2012**, *73* (6 Suppl 5), S431-7.
https://doi.org/10.1097/TA.0b013e3182755dcc.

(3)   Alam, H. B.; Burris, D.; DaCorta, J. A.; Rhee, P. Hemorrhage Control in the Battlefield:
Role of New Hemostatic Agents. *Mil. Med.* **2005**, *170* (1), 63–69.
https://doi.org/10.7205/milmed.170.1.63.

(4)   Dayan, L.; Zinmann, C.; Stahl, S.; Norman, D. Complications Associated with Prolonged
Tourniquet Application on the Battlefield. *Mil. Med.* **2008**, *173* (1), 63–66.
https://doi.org/10.7205/milmed.173.1.63.

(5)   Navein, J.; Coupland, R.; Dunn, R. The Tourniquet Controversy. *J. Trauma Acute Care
Surg.* **2003**, *54* (5), S219–S220. https://doi.org/10.1097/01.TA.0000047202.16935.E9.

(6)   Sims, K.; Montgomery, H. R.; Dituro, P.; Kheirabadi, B. S.; Butler, F. K. *Management of
External Hemorrhage in Tactical Combat Casualty Care: The Adjunctive Use of XStat^{TM}
Compressed Hemostatic Sponges: TCCC Guidelines Change 15-03*; 2016; Vol. 16.

(7)   Mueller, G. R.; Pineda, T. J.; Xie, H. X.; Teach, J. S.; Barofsky, A. D.; Schmid, J. R.;

Gregory, K. W. A Novel Sponge-Based Wound Stasis Dressing to Treat Lethal Noncompressible Hemorrhage. In *Journal of Trauma and Acute Care Surgery*; 2012; Vol. 73. https://doi.org/10.1097/TA.0b013e3182617c3c.

(8)   Kragh Jr., J. F.; Aden, J. K.; Steinbaugh, J.; Bullard, M.; Dubick, M. A. Gauze vs XSTAT in Wound Packing for Hemorrhage Control. *Am. J. Emerg. Med.* **2015**, *33* (7), 974–976. https://doi.org/10.1016/j.ajem.2015.03.048.

(9)   He, J. M.; Wu, Y. D.; Wang, W.; Cheng, W. L.; Huang, Y. D.; Fu, B. Hemostatic, Antibacterial and Degradable Performance of the Water-Soluble Chitosan-Coated Oxidized Regenerated Cellulose Gauze. *Fibers Polym.* **2014**, *15* (3), 504–509. https://doi.org/10.1007/s12221-014-0504-5.

(10)   Dai, C.; Yuan, Y.; Liu, C.; Wei, J.; Hong, H.; Li, X.; Pan, X. Degradable, Antibacterial Silver Exchanged Mesoporous Silica Spheres for Hemorrhage Control. *Biomaterials* **2009**, *30* (29), 5364–5375. https://doi.org/10.1016/j.biomaterials.2009.06.052.

(11)   Ratner, B. D. A Pore Way to Heal and Regenerate: 21st Century Thinking on Biocompatibility. *Regen. Biomater.* **2016**, *3* (2), 107–110. https://doi.org/10.1093/rb/rbw006.

(12)   Li, J.; Wu, X.; Wu, Y.; Tang, Z.; Sun, X.; Pan, M.; Chen, Y.; Li, J.; Xiao, R.; Wang, Z.; Liu, H. Porous Chitosan Microspheres for Application as Quick in Vitro and in Vivo Hemostat. *Mater. Sci. Eng. C* **2017**, *77*, 411–419. https://doi.org/10.1016/j.msec.2017.03.276.

(13)   Monroe, M. B. B.; Easley, A. D.; Grant, K.; Fletcher, G. K.; Boyer, C.; Maitland, D. J. Multifunctional Shape Memory Polymer Foams with Bio-Inspired Antimicrobials. *ChemPhysChem* **2018**, *19* (16), 1999–2008. https://doi.org/10.1002/cphc.201701015.

(14)   Behl, M.; Lendlein, A. Actively Moving Polymers. *Soft Matter.* 2007, pp 58–67. https://doi.org/10.1039/b610611k.

(15)   Christenson, E. M.; Anderson, J. M.; Hiltner, A. Biodegradation Mechanisms of Polyurethane Elastomers. *Corros. Eng. Sci. Technol.* **2007**, *24* (4), 312–323. https://doi.org/10.1179/174327807X238909.

(16)   Laschke, M. W.; Strohe, A.; Scheuer, C.; Eglin, D.; Verrier, S.; Alini, M.; Pohlemann, T.; Menger, M. D. In Vivo Biocompatibility and Vascularization of Biodegradable Porous Polyurethane Scaffolds for Tissue Engineering. *Acta Biomater.* **2009**, *5* (6), 1991–2001. https://doi.org/10.1016/j.actbio.2009.02.006.

(17)   Pretsch, T.; Jakob, I.; Müller, W. Hydrolytic Degradation and Functional Stability of a Segmented Shape Memory Poly(Ester Urethane). *Polym. Degrad. Stab.* **2009**, *94* (1), 61–73. https://doi.org/10.1016/j.polymdegradstab.2008.10.012.

(18)   Swan, K. G.; Swan, R. C. Principles of Ballistics Applicable to the Treatment of Gunshot Wounds. *Surg. Clin. North Am.* **1991**, *71* (2), 221–239. https://doi.org/10.1016/S0039-6109(16)45376-4.

(19)   Weems, A. C.; Wacker, K. T.; Carrow, J. K.; Boyle, A. J.; Maitland, D. J. Shape Memory Polyurethanes with Oxidation-Induced Degradation: In Vivo and In Vitro Correlations for Endovascular Material Applications. *Acta Biomater.* **2017**, *59*, 33–44. https://doi.org/10.1016/j.actbio.2017.06.030.

(20)   Singhal, P.; Small, W.; Cosgriff-Hernandez, E.; Maitland, D. J.; Wilson, T. S. Low Density Biodegradable Shape Memory Polyurethane Foams for Embolic Biomedical Applications. *Acta Biomater.* **2014**, *10* (1), 67–76. https://doi.org/10.1016/j.actbio.2013.09.027.

(21)   Fan, X.; Chung, J. Y.; Lim, Y. X.; Li, Z.; Loh, X. J. Review of Adaptive Programmable Materials and Their Bioapplications. *ACS Applied Materials and Interfaces*. American Chemical Society December 14, 2016, pp 33351–33370. https://doi.org/10.1021/acsami.6b09110.

(22)   Weems, A. C.; Easley, A.; Roach, S. R.; Maitland, D. J. Highly Cross-Linked Shape Memory Polymers with Tunable Oxidative and Hydrolytic Degradation Rates and Selected Products Based on Succinic Acid. *ACS Appl. bio Mater.* **2019**, *2* (1), 454–463. https://doi.org/10.1021/acsabm.8b00650.

(23)   Jang, L. K.; Fletcher, G. K.; Monroe, M. B. B.; Maitland, D. J. Biodegradable Shape Memory Polymer Foams with Appropriate Thermal Properties for Hemostatic Applications. *J. Biomed. Mater. Res. A* **2019**, *108* (6), 1281–1294.

(24)   Jaganjac, E. T. of gunshot wounds and prevention of complications during the healing process; Kuba, T.; Visna, P.; Beitl, E.; Kalvach, J. Treatment of Gunshot Wounds and Prevention of Complications during the Healing Process. *Rozhl. Chir.* **2007**, *86* (4), 188–193.

(25)   Nishikawa, M.; Hashida, M.; Takakura, Y. Catalase Delivery for Inhibiting ROS-Mediated Tissue Injury and Tumor Metastasis. *Adv. Drug Deliv. Rev.* **2009**, *61* (4), 319–326.

(26)   Bryan, N.; Ahswin, H.; Smart, N.; Bayon, Y.; Wohlert, S.; Hunt, J. A. Reactive Oxygen Species (ROS) - a Family of Fate Deciding Molecules Pivotal in Constructive Inflammation and Wound Healing. *Eur. Cells Mater.* **2012**, *24*, 249–265. https://doi.org/10.22203/eCM.v024a18.

(27)   Bandzierz, K.; Reuvekamp, L.; Dryzek, J.; Dierkes, W.; Blume, A.; Bielinski, D.

Influence of Network Structure on Glass Transition Temperature of Elastomers. *Materials (Basel).* **2016**, *9* (8), 607. https://doi.org/10.3390/MA9070607.

(28) Fox, T. G.; Loshaek, S. Influence of Molecular Weight and Degree of Crosslinking on the Specific Volume and Glass Temperature of Polymers. *J. Polym. Sci.* **1955**, *15* (80), 371–390. https://doi.org/10.1002/pol.1955.120158006.

(29) Laycock.B; Nikolić.M; Colwell.J.M; Gauthier.E; Halley.P; Bottle.S; George.G. Lifetime Prediction of Biodegradable Polymers. *Prog. Polym. Sci. Sci.* **2017**, *71*, 144–189. https://doi.org/10.1016/j.progpolymsci.2017.02.004.

(30) Dunnill, C.; Patton, T.; Brennan, J.; Barrett, J.; Dryden, M.; Cooke, J.; Leaper, D.; Georgopoulos, N. T. Reactive Oxygen Species (ROS) and Wound Healing: The Functional Role of ROS and Emerging ROS-Modulating Technologies for Augmentation of the Healing Process. *Int. Wound J.* **2017**, *14* (1), 89–96. https://doi.org/10.1111/iwj.12557.

(31) Rodriguez, J. N.; Miller, M. W.; Boyle, A.; Horn, J.; Yang, C. K.; Wilson, T. S.; Ortega, J. M.; Small, W.; Nash, L.; Skoog, H.; Maitland, D. J. Reticulation of Low Density Shape Memory Polymer Foam with an in Vivo Demonstration of Vascular Occlusion. *J. Mech. Behav. Biomed. Mater.* **2014**, *40*, 102–114. https://doi.org/10.1016/j.jmbbm.2014.07.037.

(32) Nash, L. D.; Docherty, N. C.; Monroe, M. B. B.; Ezell, K. P.; Carrow, J. K.; Hasan, S. M.; Gaharwar, A. K.; Maitland, D. J. Cold Plasma Reticulation of Shape Memory Embolic Tissue Scaffolds. *Macromol. Rapid Commun.* **2016**, *37* (23), 1945–1951. https://doi.org/10.1002/marc.201600268.

(33) Walthers, C. M.; Nazemi, A. K.; Patel, S. L.; Wu, B. M.; Dunn, J. C. Y. The Effect of Scaffold Macroporosity on Angiogenesis and Cell Survival in Tissue-Engineered Smooth

Muscle. *Biomaterials* **2014**, *35* (19), 5129–5137.

https://doi.org/10.1016/j.biomaterials.2014.03.025.

(34)   Xiao, X.; Wang, W.; Liu, D.; Zhang, H.; Gao, P.; Geng, L.; Yuan, Y.; Lu, J.; Wang, Z.

The Promotion of Angiogenesis Induced by Three-Dimensional Porous Beta-Tricalcium

Phosphate Scaffold with Different Interconnection Sizes via Activation of PI3K/Akt

Pathways. *Sci. Rep.* **2015**, *5* (1), 9409. https://doi.org/10.1038/srep09409.

(35)   Lendlein, A.; Kelch, S. Shape-Memory Polymers. *Angew. Chem., Int. Ed.* **2002**, *41* (12),

2034–2057.

(36)   Yu, Y.-J.; Hearon, K.; Wilson, T. S.; Maitland, D. J. The Effect of Moisture Absorption

on the Physical Properties of Polyurethane Shape Memory Polymer Foams. *Smart Mater.*

Struct. **2011**, *20* (8), 85010. https://doi.org/10.1088/0964-1726/20/8/085010.

(37)   Vyas, K. S.; Saha, S. P. Comparison of Hemostatic Agents Used in Vascular Surgery.

Expert Opin. Biol. Ther. **2013**, *13* (12), 1663–1672.

https://doi.org/10.1517/14712598.2013.848193.

(38)   ISO, P. ISO 10993-5:2009 Biological Evaluation of Medical Devices -- Part 5: Tests for in

Vitro Cytotoxicity. *International Organization for Standardization, Geneva*. 2009, p 34.

(39)   Beaman, H. T.; Shepherd, E.; Satalin, J.; Blair, S.; Ramcharran, H.; Serinelli, S.; Gitto, L.;

Dong, K. S.; Nieman, G.; Schauer, S. G.; Monroe, M. B. B. Hemostatic Shape Memory

Polymer Foams With Improved Survival in a Lethal Traumatic Hemorrhage Model. *SSRN*

Electron. J. **2021**, 1. https://doi.org/10.2139/ssrn.3864497.

(40)   Monroe, M. B. B.; Easley, A. D.; Grant, K.; Fletcher, G. K.; Boyer, C.; Maitland, D. J.

Multifunctional Shape-Memory Polymer Foams with Bio-Inspired Antimicrobials.

ChemPhysChem **2018**, *19* (16), 1999–2008. https://doi.org/10.1002/cphc.201701015.

(41)   Huang, L.; Lin, C.; Li, A.; Wei, B.; Teng, J.; Li, L. Pro-Coagulant Activity of Phenolic Acids Isolated from Blumea Riparia. *Nat. Prod. Commun.* **2010**, *5* (8), 1263—1266.

(42)   Liu, J.; Du, C.; Beaman, H. T.; Monroe, M. B. B. Characterization of Phenolic Acid Antimicrobial and Antioxidant Structure–Property Relationships. *Pharmaceutics* **2020**, *12* (5), 419. https://doi.org/10.3390/pharmaceutics12050419.

(43)   Lloyd, A. W. Interfacial Bioengineering to Enhance Surface Biocompatibility. *Med. Device Technol.* **2002**, *13* (1), 18–21.

(44)   Nair, L. S.; Laurencin, C. T. Biodegradable Polymers as Biomaterials. *Progress in Polymer Science (Oxford)*. Pergamon August 2007, pp 762–798. https://doi.org/10.1016/j.progpolymsci.2007.05.017.

(45)   Song, R.; Murphy, M.; Li, C.; Ting, K.; Soo, C.; Zheng, Z. Current Development of Biodegradable Polymeric Materials for Biomedical Applications. *Drug Des. Devel. Ther.* **2018**, 12–3117. https://doi.org/10.2147/DDDT.S165440.

(46)   Boyle, A. J.; Wierzbicki, M. A.; Herting, S.; Weems, A. C.; Nathan, A.; Hwang, W.; Maitland, D. J. In Vitro Performance of a Shape Memory Polymer Foam-Coated Coil Embolization Device. *Med. Eng. Phys.* **2017**, *49*, 56–62. https://doi.org/https://doi.org/10.1016/j.medengphy.2017.07.009.

Appendix B

Biostable Shape Memory Polymer Foams for Smart Biomaterial Applications*

B1. Introduction:

Shape memory polymers (SMPs) are smart materials with many potential biomedical applications. SMPs can be prepared in a primary/original shape, deformed into a temporary shape upon exposure to an external stimulus, and stored in this temporary shape once the stimulus is removed. The external stimulus can be temperature, light, pH, electrical stimulus, or a magnetic field. Upon re-exposure to the stimulus, the shape memory effect can be triggered to recover the material back to its original shape.

Based on the application, biomaterials require varying degrees of biodegradability, tissue integration, cell and blood interactions, nutrient transfer, space filling ability, and clinical functionality. Polyurethane SMPs have been extensively employed as biomaterial scaffolds in vascular applications,[1] drug delivery,[2] and tissue engineering due to their excellent tunable mechanical properties,[3] high cytocompatibility and biocompatibility,[4], [5] and the ability to tune degradation rates to match application requirements.[6], [7]

Biodegradation affects cell infiltration, vascular in-growth, and neo-tissue formation to allow successful integration of host tissue with biomaterials at the implant location. Biodegradation can occur via three major mechanisms: oxidation, hydrolysis, and enzymatic degradation.[8] Some applications, such as degradable sutures, require a fast degradation rate while others require biostable scaffolds that remain in the body over long time frames. Polyurethane SMPs present an ideal system for controlling degradation rates by selectively incorporating oxidatively, hydrolytically, and/or enzymatically responsive groups. The ability to control architecture changes with shape memory properties while tuning degradation profiles presents several potential benefits for healing, and previous research in this area is rich.[9]–[11]

190

Within the large field of polyurethane SMPs, a crosslinked, amorphous polyurethane SMP foam system has been used for vascular occlusion applications, such as aneurysm filling,[12], [13] peripheral vascular disease,[14] and hemorrhage control.[15] These materials are highly tunable, with prior work focusing on altering shape memory profiles,[16] pore structure,[17] and/or toughness[18] and on incorporation of functional motifs to enable *in vivo* imaging[19], [20] or infection control.[21] *In vitro* degradation characterization of SMP foams showed that they are hydrolytically stable, but that they degrade via oxidation.[7] Degradation was attributed to tertiary amines in the polyol crosslinkers that are used to form the polyurethane network. In a rabbit elastase aneurysm model, Herting et al. found that the materials underwent ~97% mass loss by 90 days using cross sectional histological images.[22]

Based on these findings, several subsequent studies have focused on improving the biostability of this valuable biomaterial system. Hasan et al. replaced the tertiary amine containing monomers in the SMP foams with glycerol and hexanetriol. These foams were highly stable, with <10% mass loss over 45 days in accelerated hydrolytic and oxidation medias (0.1 M NaOH and 50% H_2O_2, respectively).[23] However, their shape recovery profiles were significantly slower than the original SMP foams, with 100% volume recovery achieved after ~40 minutes in 50°C water vs. full recovery in <10 minutes in 37°C water in the control foams. This property would limit their ability to be actuated upon implantation at body temperature in future applications.

Weems et al. focused on improving biostability of shape memory polyurethanes by incorporating isocyanurate-containing alcohols.[24] This approach resulted in an increased biostability and delayed degradation. While tested in an accelerated oxidative degradation media (20% H_2O_2 catalyzed by 0.1 M $CoCl_2$), SMP films had more than 80% mass remaining after 100 days and porous SMP foams had close to 75% mass remaining after 40 days. This is a promising

approach to significantly increasing biostability; however, the eventual degradation byproduct of these polymers may contain small molecules like cyclic isocyanurates, whose cytocompatibility has not been determined. Additionally, materials with intermediate degradation rates may be required.

In a separate approach, Weems et al. achieved a reduced degradation rate by incorporating small molecule antioxidants into the foams to form an SMP composite.[25] The microparticles were physically mixed within the polymer solution; thus, this approach could result in the antioxidant-loaded microparticles leaching out of the polymer system to alter the scaffold biostability over time. In most of the composite formulations, the antioxidant payloads were released during the initial cleaning procedure. The composite that did have a well-retained antioxidant content after washing underwent complete release of the antioxidant during the first 3 days of the degradation study, and thus did not significantly alter the long-term degradation profile.

While these SMP foams have been widely employed in embolic applications, none of the prior studies characterized blood interactions following modifications, which are highly dependent on material chemistry. Additionally, there may be benefits to more moderate increases in biostability or in altering the physical erosion profiles of SMP foams, such as in load-bearing applications where bulk device failure may be detrimental to healing. To that end, we synthesized polyurethane SMP foams that were modified with ether linkages using diethylene glycol (DEG) or triethylene glycol (TEG) to extend their biostability relative to control foams. We characterized the ability to tune the rate of degradation while maintaining other properties, such as pore size and volume recovery rates; the physical erosion profiles; and cell and blood interactions in the resulting ether-containing foams. In the long-term, these foams could provide an option for biomaterial implants

with controlled degradation after implantation to maintain scaffold properties over longer time frames and to eliminate the need for implant removal.

B2. Materials and Methods

1. Materials: Hexamethylene diisocyante (HDI), diethylene glycol (DEG), triethylene glycol (TEG), N,N,N',N'-tetrakis-(2-hydroxypropyl)-ethylene diamine (HPED), triethanol amine (TEA), hydrogen peroxide (H_2O_2, Certified ACS, 30%), sodium hydroxide (NaOH), and ethanol (reagent alcohol) were purchased as used as received from Fisher Scientific (Waltham, MA). Catalysts (T-131 and BL-22) and surfactant (EP-H-190) were used as received from Evonik Corporation (Essen, Germany).

2. Foam Synthesis: Polyurethane foams were synthesized by first preparing an isocyanate (NCO) pre-mix that contained a fraction of the required hydroxyl equivalents and all the required isocyanates. A pre-polymer was formed by crosslinking the NCO pre-mix at 50°C for 48 hours. Surfactant (EP-H-190) was added to the pre-mix after 48 hours. A hydroxyl (OH) mix containing the remaining hydroxyls to balance the NCO groups, deionized (DI) water as a chemical blowing agent, and catalysts (T-131 and BL-22) was then prepared, mixed with the NCO pre-mix via a high-speed mixer (Flacktek, Landrum, SC), and poured into a large mold to form a gas blown foam. Synthesized foam compositions are shown in **Table B1**.

Table B1. Synthesized foam compositions.

Sample ID	HDI (wt%)	HPED (wt%)	TEA (wt%)	DEG (wt%)	TEG (wt%)	EPH 190 (wt%)	T-131 (wt%)	BL-22 (wt%)	Water (wt%)
Control	54.03	27.61	8.05	-	-	6.44	0.46	1.01	2.37
15% DEG	52.36	29.21	-	4.24	-	6.26	0.56	1.2	2.9
15% TEG	51.2	32.28	-	-	5.83	6.28	0.56	1.2	2.73
30% DEG	53.16	27.15	-	8.69	-	6.19	0.60	1.18	2.91
30% TEG	51.34	26.25	-	-	11.52	6.33	0.53	1.2	2.80

3. Foam Pore Analysis: Foam slices (n=3, ~1 cm^2) were cut parallel and perpendicular to the foam rise direction. Each piece was coated with gold using a Denton high vacuum sputter coater. Pore structures were characterized via a JEOL JSM 5600 scanning electron microscope (SEM) at 35X magnification under 10kV high vacuum. The micrographs were analyzed via ImageJ to quantify pore diameters.

4. Density: Cube samples (n=3, ~1 cm^3) were cut via a hot wire cutter. Dimensions and weights were measured to obtain foam densities.

5. Mechanical Testing: Dogbone punches were cut from each foam (n=3) according to the ASTM D638 (scaled down by a factor of 4; length: 6.25 mm, width: ~1.5 mm). The thickness of each piece was measured prior to testing. Samples were tested in both dry and wet conditions. To test the samples in wet conditions, they were placed in DI water at 50°C for 5 minutes and patted dry prior to analysis. Based on thermal and swelling analysis, this time frame/temperature provided equilibrium water absorption to ensure sample wetting. Samples (n=3) were stretched in a tensile tester via a 24 N load cell at a rate of 2 mm/min until failure to measure elastic modulus, elongation at break, and ultimate tensile strength.

6. Thermal analysis: Glass transition temperature (Tg) was measured for each sample (n=3, 3-5 mg) using a Q200 differential scanning calorimeter (DSC, TA instruments, New Castle, DE) in both dry and wet (plasticized) conditions. Samples were placed in t-zero aluminum pans, equilibrated at 40°C, heated to 120°C at 10°C/min, kept isothermally for 2 minutes, cooled to -40°C at 10°C/min, and heated back to 120°C at 10°C/min. Dry Tg was measured was

measured as the half-height transition temperature during the second heating cycle. To measure wet Tg, samples were plasticized by placing in DI water at 50°C for 10 minutes, pressed dry, and placed in t-zero aluminum pans with hermetic lids. A pin hole was pierced on the hermetic lid to allow water to escape during the heating cycle. Samples were equilibrated at -60°C and heated to 80°C at 10°C/min. Wet Tg was measured as the half-height transition temperature during the single heating cycle.

7. Shape Memory Behavior: Volume expansion was used to quantify shape memory behavior. Cylindrical foam samples (1 cm long, 8 mm diameter) were cut, cleaned in DI water and 70% ethanol, and dried under vacuum for 24 hours prior to testing. Each sample was heated to 100°C for 10 minutes to allow softening, and the diameter was recorded using digital calipers prior to manual crimping in a radial compression crimper (Blockwise Engineering, Tempe, AZ). After cooling to room temperature, the final crimped sample diameter and length were recorded, samples were placed in scintillation vial in a desiccator for 24 hours and fixed on a 300 µm Nitinol wire to allow for complete shape setting and relaxation to occur. After 24 hours, the foam initial diameter and length were measured, and samples were placed in a DI water bath set at 37°C and allowed to expand for 5 minutes. Images were captured every 3 seconds to observe changes in diameter over time (t) and generate a volume recovery profile. Images were analyzed using ImageJ and volume recovery was measured as:

$$\% \text{ Volume recovery} = \frac{SampleDiameter(t) \times Samplelength(t)}{\text{Initial Diameter } (d1) \times \text{Initial Length } (l1)} \times 100$$

Change in volume vs time was plotted over the expansion time frame.

8. Spectroscopic Analysis: Surface chemistry was characterized on thin slices of cleaned foam pieces using a Nicolet i70 Attenuate total reflectance (ATR)-Fourier transform infrared (FTIR) Spectrometer (Fisher Scientific, Waltham, MA) at 0.8 cm^{-1} resolution using OMNIC software. Incorporation of ethers into polyurethane foams was confirmed by the presence of peaks corresponding to the C-O of the ether group at ~1090 and ~1050 cm^{-1} and the carbonyl of urethane at ~1688 cm^{-1}.

9. Degradation Analysis: Cylindrical foams (n=8, 8 mm diameter, 1 cm height) were washed and dried, and initial masses were obtained using a gravimetric scale. Samples were placed in 3% H_2O_2 (real-time oxidative degradation media) or in 0.1M NaOH (accelerated hydrolytic degradation media) at 37°C with regular media changes. At selected time points, samples were washed with ethanol and dried under vacuum for 24 hours. After drying, samples were imaged using a camera, and masses were measured (n=5). A thin slice was cut from a sacrificial set of foams (n=3) and used to measure pore morphology (SEM), Tg (DSC), and surface chemistry (FTIR) as described above.

10. Cytocompatibility: Sample cytocompatibility was tested using 3T3 Swiss mouse fibroblasts (ATCC-CCL92). Cells were cultured with Dulbecco's modified Eagle's medium (DMEM, high glucose GlutaMAX), supplemented with 10% heat-inactivated fetal bovine serum (FBS) and 1% penicillin-streptomycin (P/S, Gibco) at 37°C/5% CO_2. Cells from passage 11 were used after 3 days of culture. Cells were seeded onto a 24-well tissue culture polystyrene plate at 10,000 cells/well and incubated for 24 hours at 37°C/5% CO_2 for 24 hours. Samples were cleaned using water, 20% Contrad solution, and isopropyl alcohol, and then soaked in 1X PBS overnight prior to testing to leach out any alcohol. Samples (n=3) were placed in each well

along with positive controls (media-only with cells, n=3), and negative controls (media-only with no cells). Samples were incubated with cells, and viability was assessed after 24 hours using a Live/Dead assay (ThermoFisher Scientific). Briefly, cells were stained with green fluorescent calcein-AM (live cells) and red-fluorescent ethidium homodimer-1 (dead cells) for 15 minutes at room temperature while protecting from light. Cells were imaged using an Inverted microscope (Leica, DMI6000) to determine the number of live (green) and dead (red) cells. Three images were captured for each sample. Cell viability of each sample (x) was measured as:

$$\text{Cell Viability (x)} = \frac{Live\ Cells}{Total\ number\ of\ cells} \times 100\%$$

11. Blood Interactions: Porcine blood (Lampire Biological Laboratories, Pipersville, PA, USA) anticoagulated with Na-Citrate upon collection was stored at 4°C for up to 3 weeks from the bleed date, according to supplier guidelines. Control, 30% DEG, and 30% TEG foams were washed and dried prior to characterization in all studies. QuikClot Combat Gauze was included as a clinical control. Blood absorption was analyzed by weighing dry samples (n = 3; ~50 mg) and incubating them in blood at 37°C. Samples were weighed at 24 hrs, and blood absorption was calculated as:

$$\%\ Absorbed = \frac{W_b - W_d}{W_d} \times 100\%$$

Where Wb is the mass of the sample in blood and Wd is the dry mass.

Platelet attachment was measured via LDH cytotoxicity assay kit (Cayman Chemical, Ann Arbor, MI). Platelet-rich plasma (PRP) was collected by centrifuging whole blood at 3000 rpm for 15 minutes to obtain a standard curve. PRP was diluted with PBS to obtain multiple

concentrations (100, 50, 25, 12.5, and 6%) to generate a standard. Hemocytometer counts were acquired at each PRP concentrations (n=4) to quantify the standard values. SMP foams (n=4) were cut to equal surface area and placed in individual wells in a 24-well plate. Gauze was used as a clinical control. One milliliter of blood was added to each well and the soaked samples were incubated at 37°C for 30 minutes. PBS was used to wash out any unattached platelets. Samples were then added to wells on a separate plate containing 1ml PBS and 100µl of 10% Triton X-100 to lyse unattached platelets. Supernatant (100 µl) from each well was added to wells on a separate 96 well plate along with 100 µl of LDH reaction solution. The mixture was incubated at 37°C for 30 minutes on an orbital shaker. Microplate reader was then used to obtain absorbance values from each sample at 490nm.

Samples that were washed with PBS to remove unattached platelets were then imaged via SEM to observe activity states and platelet activation. Prior to imaging, samples were soaked in 2% glutaraldehyde solution (Electron Microscopy Sciences, Hartfield, PA) to fix them and later dehydrated. To achieve complete dehydration, samples were soaked in a series of ethanol concentrations : (1) 30 min in 50% ethanol, (2) 30 min in 70% ethanol, (3) 30 min in 95% ethanol and finally (4) 30 min in 95% ethanol. Post dehydration samples were dried overnight in a vacuum oven at 50°C and -30 inches Hg. SEM analysis was performed using JEOL NeoScope JSM-5600 operated at 10kV. Images were captured at regions of interest at 1000X and 5000 X magnification. These images were later analyzed via ImageJ assess platelet aggregations and activation (morphology change).

12. Statistical Analysis: Measurements are presented as mean ± standard deviations. Student's T-tests were performed to determine differences between ether foams and controls. Statistical significance was taken as $p < 0.05$.

B3. Results

1. Structural Properties: Low density polyurethane foams were synthesized with a target density below 0.08 g/cm^3, **Figure B1a**. General increases in density were observed with introduction of lower amounts (15%) of ether-containing monomers, while general decreases in density were observed in higher ether content foams (30%). Pore sizes for each foam were targeted to be between 1000 and 1400 µm to ensure comparable properties to the control. 30% DEG foams have the largest pore size of 1323 µm (vs. control foams: 1151 µm), **Figure B1b**. In the SEM images, **Figure B1c**, 15% DEG and TEG foams appear to have thicker walls, which corresponds with their increased density. In addition to the higher pore size in 30% DEG foams, evidence of pore opening (pinholes in pore walls) can be observed in the 30% DEG and TEG foam SEM images, which resulted in lower density relative to the control foam.
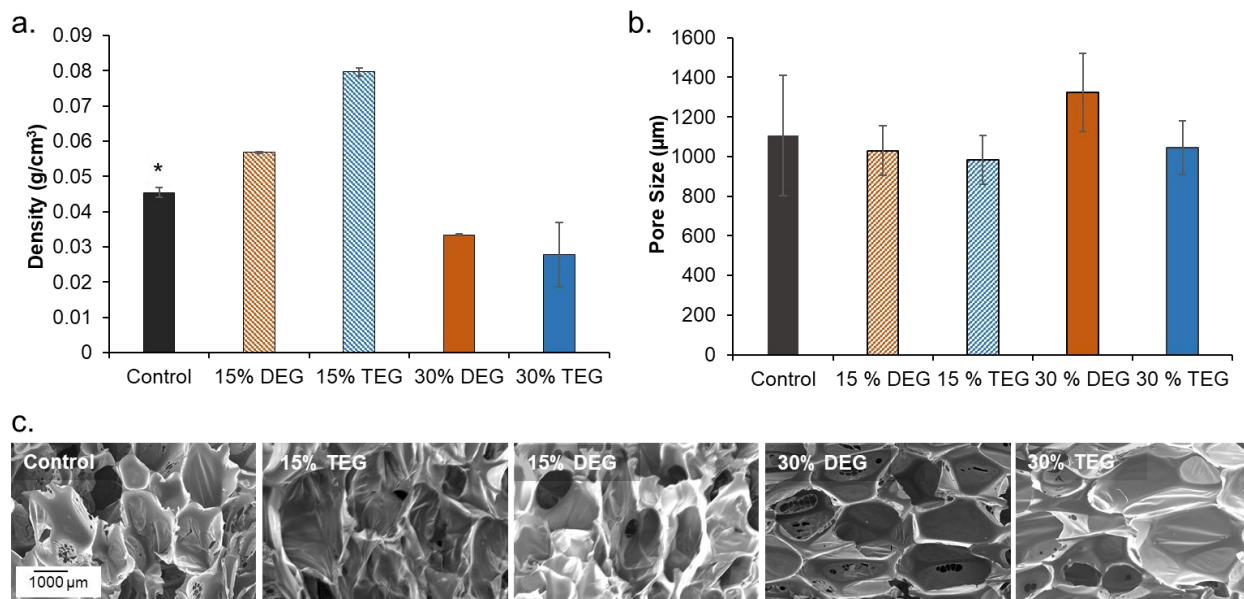

Figure B1. Structural properties of shape memory polymer foams. (a) Density of foams (n=3), (b) average pore size of foams (n=6) measured using SEM images on samples cut parallel and perpendicular to foam rise, and (c) representative micrographs of pore morphology. Scale bar of

1000 µm applies to all images. Mean ± standard deviation displayed in all panels. *p<0.05 relative to all other foams.

2. Thermal Properties: Highly crosslinked amorphous networks were formed using polyol crosslinkers with three (TEA) and four (HPED) hydroxyl groups, along with short chain diol monomers (DEG and TEG), which was indicated by the absence of melting peaks in the DSC traces. As seen in **Figure B2a**, all foams had dry T_g's above 40°C, which enables stable storage of foams at room temperature (~22 °C) without premature shape memory actuation. The target wet glass transition temperature below 37°C was also obtained in all foams, **Figure B2b**, which enables actuation of shape memory behavior upon implantation and exposure to water present in the body via water-induced plasticization of the SMPs.
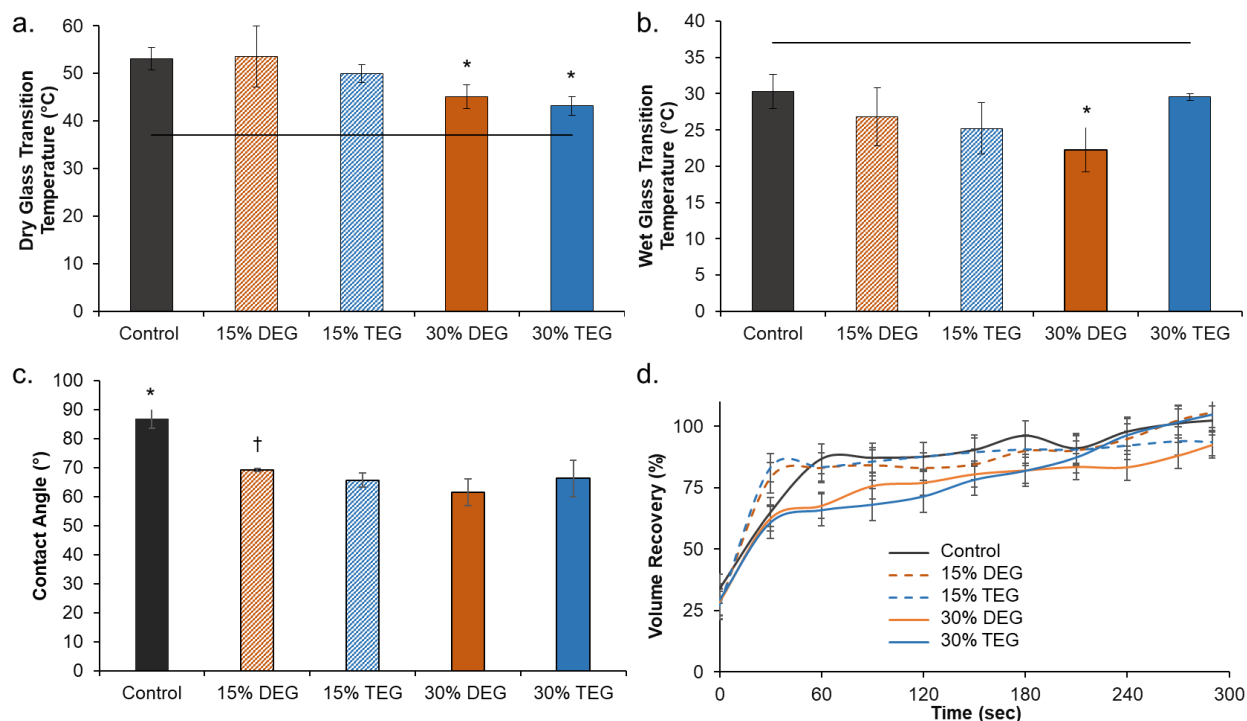

Figure B2. Thermal, shape memory, and hydrophilicity properties of SMP foams. (a) Dry glass transition temperature (n=3, *p<0.05 relative to control), (b) wet glass transition temperature (n=3,

*p<0.05 relative to control), (c) contact angle (n=5, *p<0.05 relative to all other samples, †p<0.05 relative to 15% TEG and 30% DEG samples), and (d) volume recovery of samples (n=3) in deionized water at 37°C. Mean ± standard deviation displayed in all panels.

3. Hydrophilicity and Shape Memory: Contact angle was measured on each formulation in bulk film form to compare the difference in water interactions between the foams. Control films had the highest contact angle (87°) and the inclusion of DEG and TEG increased hydrophilicity, as evidenced by decreased contact angles (down to 63° for TEG and 70° for DEG), as shown in **Figure B2c**. Shape memory profiles of samples were evaluated to indicate their capability to return from their secondary, compressed shape to their original, expanded shape after implantation and exposure to water in the body, **Figure B2d**. All foams expanded back to 100% of their original volume within ~200 seconds. In general, volume expansion profiles were similar, but the 15% DEG and TEG foams had faster expansion in the first 30 seconds, and the 30% DEG and TEG foams had slower expansion in the first 60 seconds relative to the control.

4. Tensile Testing: The addition of ether containing diol monomers resulted in an overall reduction of elastic modulus and increase in maximum elongation in the wet and dry states compared to controls, **Table B2**. The highest reduction in modulus relative to the control (22X) was observed in 30% TEG foams, which corresponds with the highest increase (8X) in elongation at break. All foams had a reduction in modulus and corresponding increase in elongation after undergoing water-induced plasticization in DI water at 50°C for 5 minutes. The wet foam mechanical properties were overall more similar between formulations.

Table B2. Tensile properties of shape memory polymer foams in dry and wet conditions. n = 3, mean ± standard deviation displayed.

Sample ID	Elastic Modulus (kPa)		Maximum Elongation ε (mm/mm)	
	dry	wet	dry	wet
Control	3200 ± 1700	150 ± 20	0.17 ± 0.04	0.4 ± 0.2
15% DEG	840 ± 140	41 ± 5	0.25 ± 0.01	0.9 ± 0.5
30% DEG	140 ± 40	32 ± 6	0.46 ± 0.17	3.0 ± 1.2
15% TEG	790 ± 270	45 ± 13	0.28 ± 0.14	1.2 ± 0.2
30% TEG	170 ± 110	12 ± 3	1.25 ± 0.45	1.0 ± 0.1

5. Degradation Analysis:

   5.1. Mass loss and physical erosion: All foams remained stable in accelerated hydrolytic media (0.1M NaOH), with less than 10% mass loss over 98 days, **Figure B3a**. In the oxidative media (3% H_2O_2) foams had comparable, approximately linear mass loss rates over the first 40 days, **Figure B3b.** After that, control foams began to degrade more quickly, and they underwent bulk erosion and started breaking into smaller pieces by ~56 days, **Figure B4**. Amongst the ether containing foams, 30% DEG foams had the slowest degradation rate and had 5% mass remaining after 105 days followed by 30% TEG foams, which fully degraded in 98 days. The ether containing foams appeared to undergo surface erosion, maintaining their bulk geometries over >80 days, **Figures B4 and B5**.
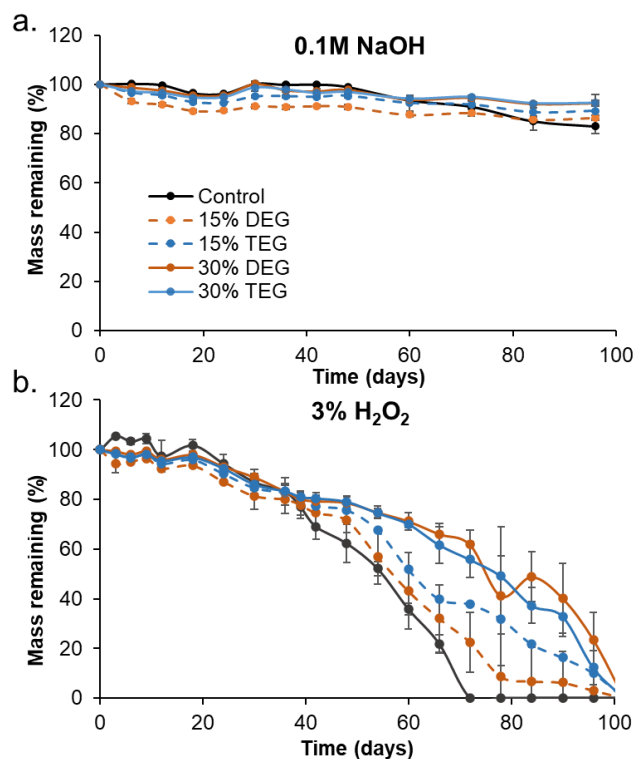
Figure B3. Mass loss profiles of samples as a function of time in (a) accelerated hydrolytic degradation media, 0.1M NaOH, and (b) oxidative degradation media, 3% H_2O_2. n=5, mean ± standard deviation displayed.

5.2. Thermal Analysis: As degradation proceeded, thermal analysis was performed to measure T_g as an indication of network crosslink density over time, **Figure B4**. This data can be used as an indication of whether the foams underwent surface or bulk degradation, where surface degradation would indicate that the polymer network and crosslink density remain intact during material breakdown. Interestingly, despite their observed physical bulk erosion, control foams retained their T_g (~50-60°C) throughout the entire degradation process. All ether-containing foams retained their T_g's until ~56 days, after which there was an observed decrease in T_g. Thus, surface degradation likely occurred throughout

most of the degradation process, as is expected for oxidative degradation, due to the high reactivity of reactive oxygen species.
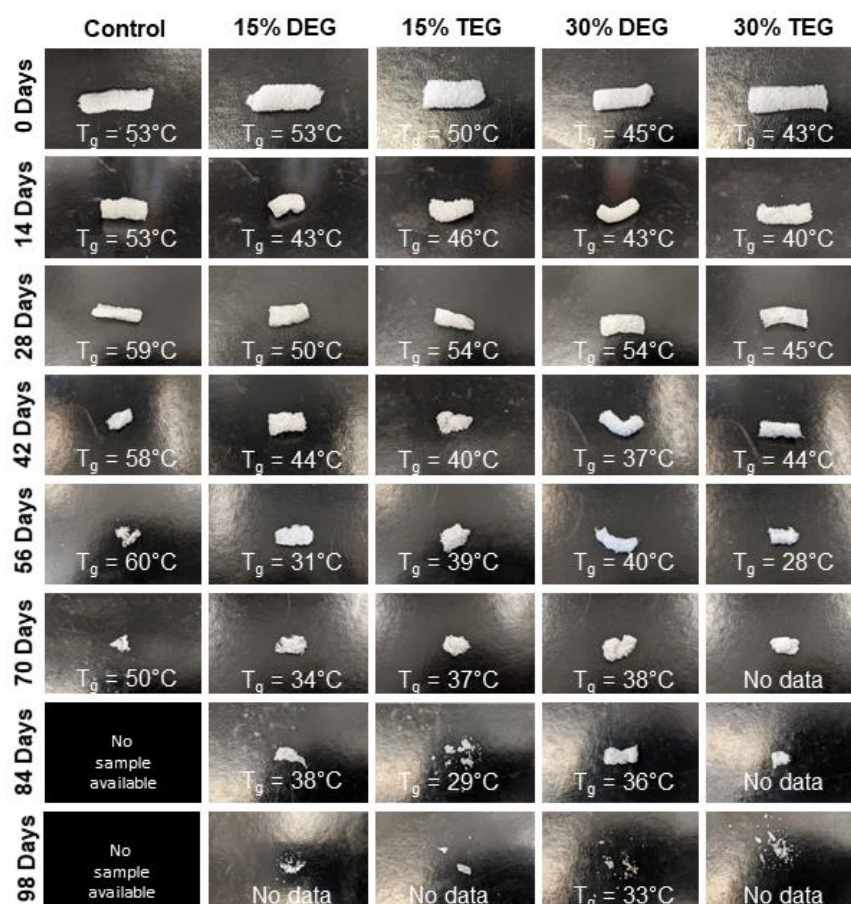
Figure B4. Physical erosion profile of samples degrading in oxidative degradation media, 3% H_2O_2 along with respective T_g's measured at each time point.

5.3 Pore Morphology: SEM was used to analyze pore morphology every two weeks, as shown in **Figure B5**. Control foams began losing their porous structure by 14 days and underwent significant strut breaking by 28 days. Total pore collapse was observed in control foams by 42 days. Among the ether containing foams, 30% DEG and 30% TEG generally maintained their pore morphology while shrinking over time, with some strut breakage at

~70 days and collapse at ~98 days. Material shrinkage can also be seen in 15 DEG and

TEG foams, with maintained visible pores over ~70 days.
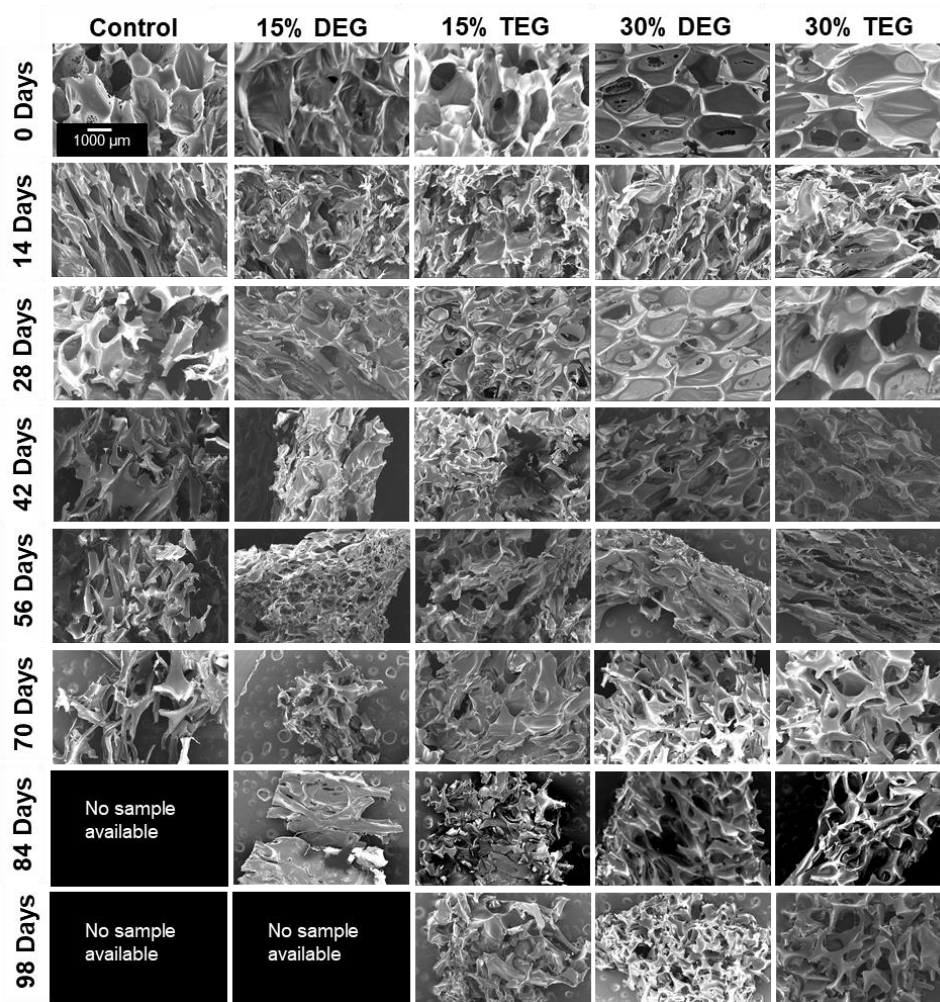
Figure B5. SEM micrographs depicting the overall pore morphology observed during degradation

in oxidative media, 3% H_2O_2, over 98 days. Scale bar of 1000 µm applies to all images.

5.4 Spectroscopic Analysis: FTIR spectra during degradation in 3% H_2O_2 revealed a shift in

the urethane peak from 1680 cm^{-1} to 1688 cm^{-1} and a reduction in tertiary amine peaks of

HPED and TEA at 1050 cm^{-1}, which has been previously observed, **Figure B6**.[26] As the

tertiary amine peak in the ether-containing foams is reduced, the ether peak at ~1090 cm^{-1}

become more apparent, indicating that the ether groups remain stable during degradation.

There is no visible evidence of ether crosslinking (branched ether peak at ~1174 cm^{-1}) during degradation in the FTIR spectra.[27]

Figure B6. FTIR spectroscopic analysis of samples during degradation in oxidative media, 3% H$_2$O$_2$.

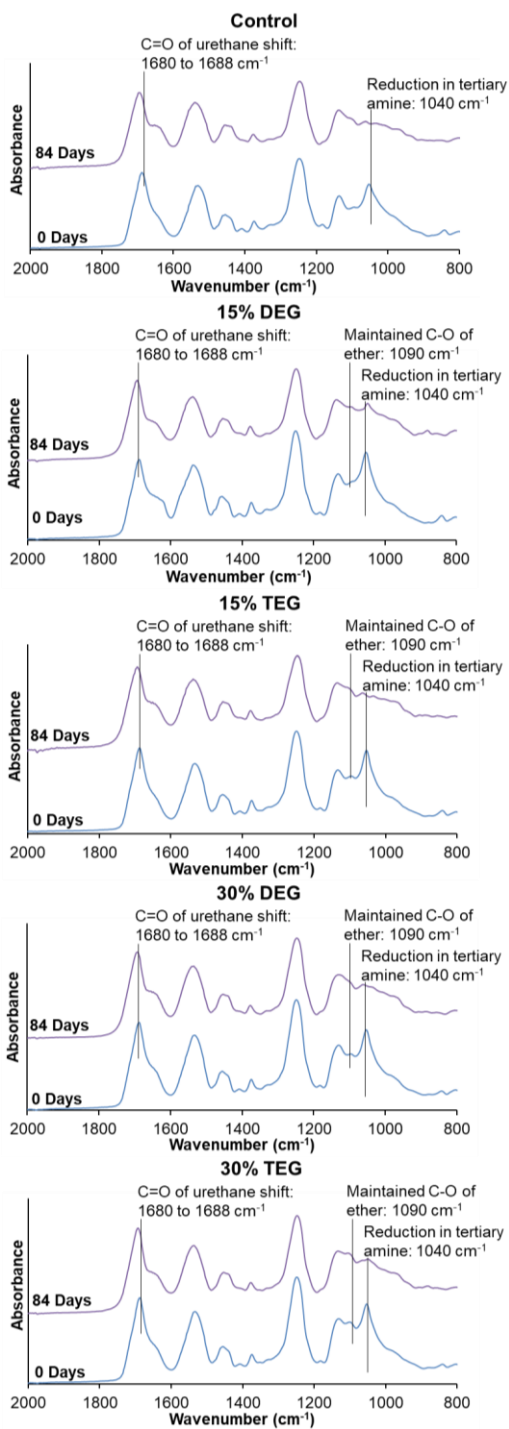6   Cell and blood interactions: Since 15% DEG and 15% TEG had a faster degradation rate compared to 30% DEG and 30% TEG samples, cell and blood interactions were studied exclusively for the foams containing 30% ether linkages along with control foams and a clinical control (QuickClot gauze). Cell viability was confirmed to be ~100% for all samples after 24 hours of incubation, **Figure B7a**. As seen in **Figure B7b**, control foams absorbed the highest amount of blood among the tested samples, and all materials absorbed between 100 and 200% of their dry weight in blood. Platelet attachment was quantified after incubation of samples in platelet rich plasma. As shown in the **Figure B7c**, maximum platelet attachment was observed on 30% DEG, followed by gauze and 30% TEG with comparable platelet numbers that were approximately half that of 30% DEG. Control foams had the lowest number attached platelets. These results correlate the platelet aggregation and activation visualized using SEM micrographs, **Figure B7d**. The gauze clinical control had aggregated platelets with evident of thrombus formation. All three SMP foams showed evidence of platelet activation (small protrusions on platelet surfaces) and aggregation, and imaged platelet densities correspond with the numbers quantified using the LDH assay.
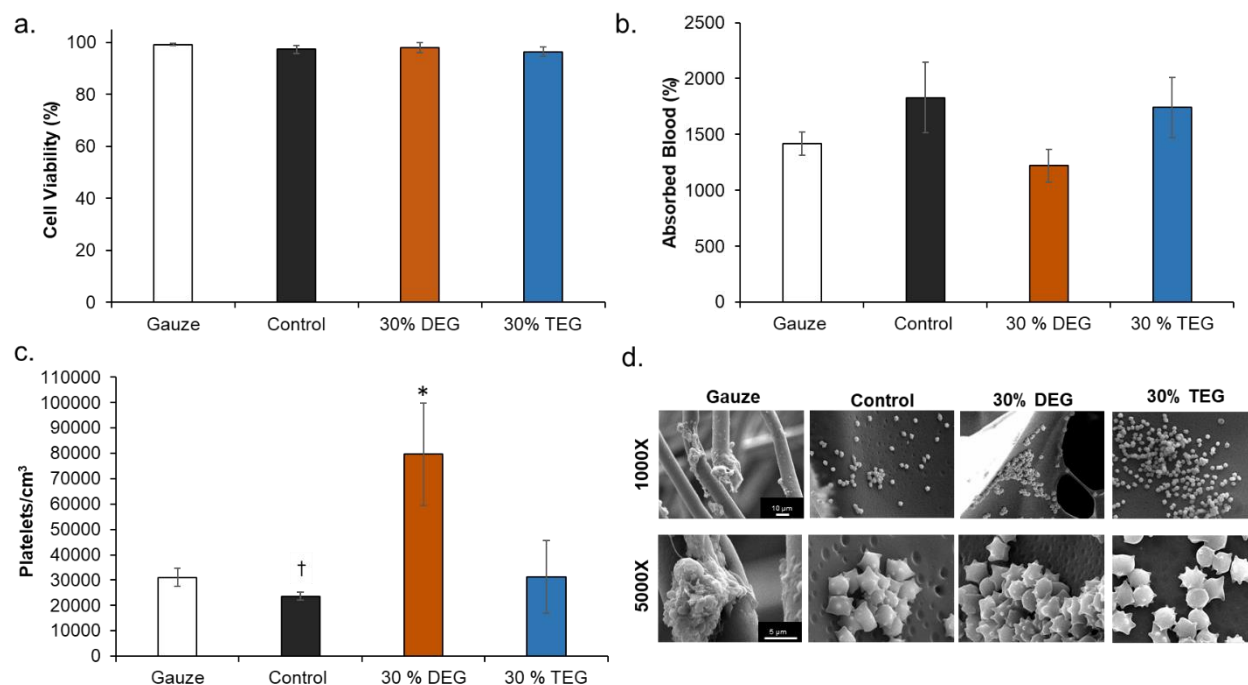
Figure B7. Cell and blood interactions with SMP foams. (a) 3T3 mouse fibroblast viability over 24 hours (n=3). (b) Whole porcine blood absorption after 24 hours of incubation (n=3). (c) Platelet attachment to sample surfaces (n=3, *p<0.05 relative to all samples, †p<0.05 relative to gauze). Mean ± standard deviation displayed in all panels. (d) SEM micrographs of attached platelets. Scale bars shown in Gauze column apply to all other images in a given row.

B4. Discussion

Foam Physical Characterization: Overall, it was observed that adding ether-containing monomers, DEG and TEG, resulted in an increased pore interconnectivity and reduction in T_g compared to control foams. We hypothesize that the increased hydrophilicity of DEG and TEG enabled increased interactions between the monomers in the pre-polymer and the chemical blowing agent (water) and/or the surfactant, which resulted in pore opening in the 30% DEG and TEG foams. This phenomenon could be advantageous in applications that require increased interconnectivity without relying on physical or mechanical modifications like mechanical reticulation,[17] plasma treatment,[28] and/or the addition of physical blowing agents.

TEG-containing foams had slightly lower T_g's compared to corollary DEG-containing foams, and increasing TEG and DEG content induced further decreases in T_g. Reduction in foam T_g of is attributed to increased hydrophilicity and flexibility of DEG and TEG, which corresponds with the contact angle measurements. Additionally, replacing the tri-functional TEA with difunctional DEG or TEG theoretically reduces foam crosslink density, which would result in lower T_g. However, all foams had dry T_g well above room temperature, which would enable their stable storage in the secondary shape. Exposure to water at 37 °C results in a reduction in T_g due plasticization by water molecules penetrating the inner structure of the foams. This reduced T_g aids in rapid volume recovery once implanted in the body and exposed to water in body temperature blood.

The increased elongation at break and decreased stiffness of the ether containing foams were expected due to the overall decreases in crosslink density and increased chain flexibility of ether linkages. The penetration of water molecules into the polymer network and interruption of hydrogen bonds allows the polymer chains to move more freely, as indicated by the overall

decreased modulus and increased elongation at break of all samples in the wet conditions compared to foams tested in dry conditions. The dry measurements are important for considering material handling prior to implantation, and all materials are mechanically robust and easy to handle in the dry state. The wet measurements provide information about the material properties after implantation, which is important for matching native tissue properties. Again, all materials are mechanically within the range of soft tissues, and the differences between the ether foams and controls are reduced in the wet state.[29] In future work, the ether foams could be modified with stiffer diisocyanate species to increase the modulus if needed.[16]

Foam Degradation Profiles: When incubated in accelerated hydrolytic degradation medium containing 0.1M NaOH, all samples remained stable, with no significant mass loss due to the lack of hydrolytically labile linkages. This result agrees with previous work on this material system that consistently shows high hydrolytic stability.[7], [30] In oxidative degradation medium containing 3% H_2O_2, control foams physically broke apart after ~42 days, while the other formulations maintained their geometry for longer times throughout the degradation time frame. These physical changes were accompanied by an increase in the mass loss rate in control foams. The breaking apart of control foams may be attributed to their relatively high brittleness, evidenced by the lowest elongation at break (0.17 ± 0.04 mm/mm), compared to the other formulations. During the degradation study, foams are repeatedly subjected to minor mechanical forces during the weekly washing and drying steps. Since the control foams are more brittle, they may break apart more easily and be more susceptible to bulk erosion, despite maintaining T_g values throughout degradation. The ether-containing foams were more flexible and less susceptible to these stresses, as demonstrated by their increased overall physical integrity throughout degradation, which translates to slower and more consistent degradation rates. The ether linkages appear to remain

211

intact during the degradation process as evidenced in FTIR spectra. This stability of the ether linkages could potentially contribute to their increased stability and more consistent degradation profiles.

While the overall changes in degradation rates were not hugely different, the introduction of ether linkages increased the oxidatively stability by ~40% (increase from 72 days for control to 100+ days for ether foams). Additionally, the observed surface erosion and maintenance of pore structure over longer time frames may be beneficial for graded load transfer during new tissue formation as the SMP foams degrade. Finally, the ability to tune degradation independently of thermal and shape memory properties enables easy transition to ether containing foams to increase degradation rates without altering storage or implantation considerations.

Foam Biological Characterization: While future studies will require more in-depth analysis of biocompatibility after implantation and cytocompatibility of degradation byproducts, the addition of TEG and DEG does not affect cytocompatibility of SMP foams. In terms of blood absorption, the increased absorption by TEG foams compared to DEG foams is attributed to increased hydrophilicity, which increases fluid uptake. The increased absorption by control foams may be attributed to their closed pore structure, which increases blood retention compared to open pore ether foams.

Various surface characteristics, like surface charge, relative hydrophilicity, and surface roughness, can impact protein absorption and subsequent blood and/or cell interactions with biomaterials. Thus, blood interactions must be considered when making chemical changes in any biomaterial system, particularly for embolic applications. It was observed that the 30% DEG foams had the highest platelet attachment, both in the quantified LDH assay and the qualitative SEM

imaging. The 30% TEG foams had similar platelet attachment values to clinical gauze control, and control foams showed the lowest number of attached platelets. When visualized using SEM, gauze promoted thrombus formation within the testing time frame, while all SMP foams had aggregated and activated platelets with similar trends observed in relative platelet numbers on each surface. This result shows that incorporating ether linkages into the SMP foams enhanced platelet attachment and activation, which may translate to increased efficacy of these materials in embolic applications and provides a new tool for increasing clotting in SMP foams.

B5. Conclusions

A reduction in SMP foam degradation rate was achieved by incorporating ether linkages. The resulting foams maintaining desired thermal properties, which allows stable storage in the secondary shape at room temperature prior to use and rapid volume recovery upon implantation. The modified foams have rapid volume recovery and increased flexibility that allows easy implantation without premature breaks or tears. Addition of ether linkages to the foams enabled uniform surface erosion that improves retainment of scaffold integrity, which can be vital in slowly-degrading biomaterials applications. Increased clotting capabilities were seen in the 30% DEG foams that also have the slowest degradation rates. Overall, these materials could be employed in hemostatic applications and then left in place to slowly degrade during healing, eliminating risks associated with implant removal after its intended application.

B6. References

[1] M. W. Laschke *et al.*, "In vivo biocompatibility and vascularization of biodegradable porous polyurethane scaffolds for tissue engineering," *Acta Biomater.*, vol. 5, no. 6, pp. 1991–2001, 2009.

[2] H. M. Wache, D. J. Tartakowska, A. Hentrich, and M. H. Wagner, "Development of a polymer stent with shape memory effect as a drug delivery system," *J. Mater. Sci. Mater. Med.*, vol. 14, no. 2, pp. 109–112, 2003.

[3] J.-L. Sormana and J. Carson Meredith, "High-Throughput Discovery of Structure−Mechanical Property Relationships for Segmented Poly(urethane−urea)s," *Macromolecules*, vol. 37, no. 6, pp. 2186–2195, Feb. 2004.

[4] J. Guan and W. R. Wagner, "Synthesis, characterization and cytocompatibility of polyurethaneurea elastomers with designed elastase sensitivity," *Biomacromolecules*, vol. 6, no. 5, pp. 2833–2842, 2005.

[5] P. Singhal, W. Small, E. Cosgriff-Hernandez, D. J. Maitland, and T. S. Wilson, "Low density biodegradable shape memory polyurethane foams for embolic biomedical applications," *Acta Biomater.*, vol. 10, no. 1, pp. 67–76, Jan. 2014.

[6] L. K. Jang, G. K. Fletcher, M. B. B. Monroe, and D. J. Maitland, "Biodegradable shape memory polymer foams with appropriate thermal properties for hemostatic applications," *J. Biomed. Mater. Res. A*, vol. 108, no. 6, pp. 1281–1294, 2019.

[7] A. C. Weems, K. T. Wacker, J. K. Carrow, A. J. Boyle, and D. J. Maitland, "Shape memory polyurethanes with oxidation-induced degradation: In vivo and in vitro correlations for endovascular material applications," *Acta Biomater.*, vol. 59, pp. 33–44, Sep. 2017.

[8] S. P. Lyu and D. Untereker, "Degradability of polymers for implantable biomedical

devices," *Int. J. Mol. Sci.*, vol. 10, no. 9, pp. 4033–4065, 2009.

[9]   W. M. Huang, B. Yang, Y. Zhao, and Z. Ding, "Thermo-moisture responsive

polyurethane shape-memory polymer and composites: A review," *J. Mater. Chem.*, vol.

20, no. 17, pp. 3367–3381, 2010.

[10]   J. Lee and S.-K. Kang, "Principles for Controlling the Shape Recovery and Degradation

Behavior of Biodegradable Shape-Memory Polymers in Biomedical Applications,"

Micromachines 2021, Vol. 12, Page 757, vol. 12, no. 7, p. 757, Jun. 2021.

[11]   M. Zare, P. Davoodi, and S. Ramakrishna, "Electrospun Shape Memory Polymer Micro-

/Nanofibers and Tailoring Their Roles for Biomedical Applications," *Nanomater. 2021,*

Vol. 11, Page 933, vol. 11, no. 4, p. 933, Apr. 2021.

[12]   A. J. Boyle *et al.*, "In vitro and in vivo evaluation of a shape memory polymer foam-over-

wire embolization device delivered in saccular aneurysm models," *Journal of Biomedical*

Materials Research - Part B Applied Biomaterials, vol. 104, no. 7. pp. 1407–1415, 2016.

[13]   A. J. Boyle *et al.*, "In vitro performance of a shape memory polymer foam-coated coil

embolization device," *Med. Eng. Phys.*, vol. 49, pp. 56–62, 2017.

[14]   T. L. Landsman *et al.*, "Design and verification of a shape memory polymer peripheral

occlusion device," *J. Mech. Behav. Biomed. Mater.*, vol. 63, pp. 195–206, Oct. 2016.

[15]   H. T. Beaman *et al.*, "Hemostatic Shape Memory Polymer Foams With Improved Survival

in a Lethal Traumatic Hemorrhage Model," *SSRN Electron. J.*, p. 1, 2021.

[16]   P. Singhal *et al.*, "Controlling the Actuation Rate of Low-Density Shape-Memory

Polymer Foams in Water," *Macromol. Chem. Phys.*, vol. 214, no. 11, pp. 1204–1214, Jun.

2013.

[17]   J. N. Rodriguez *et al.*, "Reticulation of low density shape memory polymer foam with an

in vivo demonstration of vascular occlusion," *J. Mech. Behav. Biomed. Mater.*, vol. 40, pp. 102–114, Dec. 2014.

[18] A. D. Easley, M. B. B. Monroe, S. M. Hasan, A. C. Weems, J. Frederick, and D. J. Maitland, "Shape memory polyurethane-urea foams with improved toughness," *J. Appl. Polym. Sci.*, vol. 136, no. 14, p. 47268, Dec. 2018.

[19] A. C. Weems *et al.*, "Shape Memory Polymers with Visible and Near-Infrared Imaging Modalities: Synthesis, Characterization and In Vitro Analysis," *RSC Adv.*, vol. 7, no. 32, pp. 19742–19753, 2017.

[20] S. M. Hasan *et al.*, "Tungsten-loaded SMP foam nanocomposites with inherent radiopacity and tunable thermo-mechanical properties," *Polym. Adv. Technol.*, vol. 27, no. 2, pp. 195–203, Feb. 2016.

[21] M. B. B. Monroe, A. D. Easley, K. Grant, G. K. Fletcher, C. Boyer, and D. J. Maitland, "Multifunctional Shape-Memory Polymer Foams with Bio-inspired Antimicrobials," *ChemPhysChem*, vol. 19, no. 16, pp. 1999–2008, Aug. 2018.

[22] S. M. Herting *et al.*, "In vivo comparison of shape memory polymer foam-coated and bare metal coils for aneurysm occlusion in the rabbit elastase model," *J. Biomed. Mater. Res. Part B Appl. Biomater.*, vol. 107, no. 8, pp. 2466–2475, Nov. 2019.

[23] S. M. Hasan, G. K. Fletcher, M. B. B. Monroe, M. A. Wierzbicki, L. D. Nash, and D. J. Maitland, "Shape Memory Polymer Foams Synthesized Using Glycerol and Hexanetriol for Enhanced Degradation Resistance," *Polymers (Basel).*, vol. 12, no. 10, p. 2290, Oct. 2020.

[24] A. C. Weems, J. K. Carrow, A. K. Gaharwar, and D. J. Maitland, "Improving the Oxidative Stability of Shape Memory Polyurethanes Containing Tertiary Amines by the

Presence of Isocyanurate Triols," *Macromolecules*, vol. 51, no. 22, pp. 9078–9087, 2018.

[25]   A. C. Weems, W. Li, D. J. Maitland, and L. M. Calle, "Polyurethane Microparticles for Stimuli Response and Reduced Oxidative Degradation in Highly Porous Shape Memory Polymers," *ACS Appl. Mater. Interfaces*, vol. 10, no. 39, pp. 32998–33009, Oct. 2018.

[26]   A. C. Weems, K. T. Wacker, J. K. Carrow, A. J. Boyle, and D. J. Maitland, "Shape Memory Polyurethanes with Oxidation-Induced Degradation: In Vivo and In Vitro Correlations for Endovascular Material Applications," *Acta Biomater.*, vol. 59, pp. 33–44, 2017.

[27]   E. M. Christenson, J. M. Anderson, and A. Hiltner, "Oxidative mechanisms of poly(carbonate urethane) and poly(ether urethane) biodegradation: In vivo and in vitro correlations," *J. Biomed. Mater. Res. - Part A*, vol. 70, no. 2, pp. 245–255, 2004.

[28]   L. D. Nash *et al.*, "Cold Plasma Reticulation of Shape Memory Embolic Tissue Scaffolds," *Macromol. Rapid Commun.*, vol. 37, no. 23, pp. 1945–1951, Dec. 2016.

[29]   A. B., S. Rao, and H. J. Pandya, "Engineering approaches for characterizing soft tissue mechanical properties: A review," *Clin. Biomech.*, vol. 69, pp. 127–140, 2019.

[30]   A. U. Vakil *et al.*, "Shape Memory Polymer Foams with Tunable Degradation Profiles," *ACS Appl. Bio Mater.*, vol. 4, no. 9, pp. 6769–6779, Sep. 2021.

Name of Author: Anand Utpal Vakil

Place of Birth: Ahmedabad, Gujarat, India

Date of Birth: June 24, 1994

Education:

B.Tech. Chemical Engineering, Manipal Institute of Technology, 2016

MS. Chemical Engineering, Syracuse University, 2018

Ph.D. Chemical Engineering, Syracuse University, 2018- Present

Awards and Honors

2022   Society for Biomaterials (SFB) BioInterfaces Rena Bizios Poster Award, 1st Place

2022   SFB Biomaterials Education Challenge, 1st Place

2020   Stevenson Biomaterials Research Poster Session Best Commercialization Potential

2019-2022 Syracuse University SFB Student Chapter Secretary

2019   University of Rochester's Frontiers in Material Science for the 21st century Symposium, 1st place

Publications, *mentored undergraduate

A.U. Vakil, N.M. Petryk, ***** E. Shepherd, H.T. Beaman, "Biostable Shape Memory Polymer Foams for Smart Biomaterial Applications," Polymers. 2021, 13, 4084. https://doi.org/10.3390/polym13234084

N. M. Petryk, * G. Haas, **A. U. Vakil**, and M. B. B. Monroe, "Shape memory polymer foams with tunable interconnectivity using off-the-shelf foaming components," J. Biomed. Mater. Res. Part A, 2022. https://doi.org/10.1002/jbm.a.37383

A.U. Vakil, N.M. Petryk, * E. Shepherd, H.T. Beaman, P.S. Ganesh, K.S. Dong, M.B.B. Monroe, "Shape Memory Polymer Foams with Tunable Degradation Profiles," ACS Applied BioMaterials, In Press (2021). DOI: 10.1021/acsabm.1c00516.

N. Christmas,* **A.U. Vakil**, C.J. Hatch, S. Dong, D. Fikhman, H.T. Beaman, M.B.B. Monroe, "Characterization of Shape Memory Polymer Foam Hemostats in In Vitro

Hemorrhagic Wound Models." Journal of Biomedical Materials Research Part B: Applied Biomaterials, 109 (5), 681-692 (2021). https://doi.org/10.1002/jbm.b.34732.

Manuscripts in Preparation and Submission, *mentored undergraduate

A.U. Vakil, N.M. Petryk*, C. Du, B. Howes*, D.Stinfort*, S. Serinelli, L. Gitto, M. Ramezani, H.T. Beaman and M.B.B. Monroe. "Comparison of in vitro and in vivo degradation of polyurethane foams with tunable degradation rates" In preparation

A.U. Vakil, M. Ramezani, and M.B.B. Monroe. "Antimicrobial shape memory polymer hydrogels for chronic wound dressings" Under review at *ACS Applied Bio Materials*

A.U. Vakil, M. Ramezani, and M.B.B. Monroe. "Magnetically Actuated Shape Memory Polymers for On-Demand Drug Delivery" Under review at *Materials*

National Conference Presentations, <u>presenting author</u>, *mentored undergraduate

<u>A.U. Vakil</u>, Y. Espiritusanto, E. Jain, M.B.B. Monroe, "Temporally-Controlled Shape Memory Polymers for Drug Delivery," *2022 Annual Meeting of the Society for Biomaterials,* Baltimore, MA, April 27-30, 2022. *Poster Presentation.* **1st place: Dr. Rena Bizios Poster Awards**

<u>N.M. Petryk</u>,* G. Haas, **A.U. Vakil**, M.B.B. Monroe,. "Shape Memory Polymer Foams with Tunable Interconnectivity Using Off-the-Shelf Foaming Components," *2022 Annual Meeting of the Society for Biomaterials,* Baltimore, MA, April 27-30, 2022. *Poster Presentation.* **SFB Student Award for Outstanding Research, 2nd place: Dr. Rena Bizios Poster Awards**

<u>G.N. Haas</u>, N.M. Petryk, **A.U. Vakil**, M.B.B. Monroe, "Effects of Commercially-Available Catalysts on Shape Memory Polymer Foam Properties," *2022 Annual Meeting of the Society for Biomaterials,* Baltimore, MA, April 27-30, 2022. *Poster Presentation.*

<u>A.U. Vakil</u>, M.B.B. Monroe, "Magnetically Induced Shape Memory Polymers for On-Demand Drug Delivery," *31st Annual BioInterface Workshop & Symposium*, September 1 – October 1, 2021, *Oral Pitch*

<u>N.M. Petryk</u>,* G.N. Haas, **A.U. Vakil**, M.B.B. Monroe, "Tuning Porosity and Interconnectivity of Polyurethane Shape Memory Polymer Foams Using Off-the-Shelf Foaming Components," *31st Annual BioInterface Workshop & Symposium*, September 1 – October 1, 2021, *Oral Pitch*. **1st Place in Student Pitch Competition.**

<u>A.U. Vakil</u>, M.B.B. Monroe, "Temporally Controlled Shape Memory Polymers for On-Demand drug delivery" *2021 Annual Meeting of the Society for Biomaterials*, Online Meeting, April 20-23, 2021, *Rapid Fire Presentation.*

N.M. Petryk,* **A.U. Vakil**, M.B.B. Monroe, "Polyurethane Shape Memory Polymer Foams with Off-the-Shelf Physical Blowing Agents," *2021 Annual Meeting of the Society for Biomaterials*, Online Meeting, April 20-23, 2021, *Oral Presentation.*

A.U. Vakil, N.M. Petryk,* M.B.B. Monroe, "Biodegradable Shape Memory Polymer Hemostats," *ACS Fall 2020 Meeting and Exposition*, Online Meeting, August 17-20, 2020, *Oral Presentation.*

A.U. Vakil, N.M. Petryk,* M.B.B. Monroe, "Biodegradable Shape Memory Polymer Foams for Hemostatic Applications," *ACS Spring 2020 Meeting and Exposition*, Online Meeting, March 22-26, 2020. *Oral Presentation.*